PETROLEUM RESEARCH JOURNAL

TECHNICAL PAPERS

ENGINEERING

Improvement of the accuracy of statistical well log interpretation using the material balance equation .... *G. Szigeti* 1

Description of naturally fractured reservoirs for simulation studies ..... *J.C. Sabathier* 6

Corrosion control in DEFA waterflood system .... *M.A. Elarabi* 16

EXPLORATION

Post-stack deconvolution and multiples attenuation .... *M.M. Elazezi* 22

Amplitude features of fast compressional waves in porous media on zero-offset synthetic seismograms .... *A.A.A. Othman* 37

Depositional environment of the Bahi Formation deduced by textural analysis, NW Sirt Basin, Libya .... *A.M.A. Sghair* 46

Microprobe analysis of the glauconite pellets of the Lidam Formation NW Sirt Basin, Libya .... *M. El-Bakai* 56

CHEMISTRY

Kinetics of formation of epichlorohydrin from allyl chloride by hydrogen peroxide using sodium molybdate as catalyst ..... *I. Ahmad and A.R. Labib* 62

Synthesis and study of different thioamides as corrosion inhibitors .... *M.A. Khawaja, S.R. Abu Oun, M.A. Shariff* 67

SHORT NOTES

The effects of hydrogen on the fracture toughness of stainless steel ..... *A.T. Hassan* 76

VOLUME 5-1993

Petroleum Research Centre
P.O. Box 6431 Tripoli
Great Socialist People's Libyan Arab Jamahiriya

PRJ, Vol. 5 (January 1993); P. 1–5, 3 TABLES.

IMPROVEMENT OF THE ACCURACY OF STATISTICAL WELL LOG INTERPRETATION USING THE MATERIAL BALANCE EQUATION

G. Szigeti*

دقة الإستقراء الإحصائي لسرود الآبار باستخدام معادلة توازن المواد

ج. زيقيتي

عند تحديد مسامية كتلة الصخور داخل البئر النفطي تتم مقارنة القيم المقاسة بتلك التي تم حسابها من النموذج الإفتراضي للصخور. وتنتج عن هذه المقارنة معادلات اتفاقية. وعلى افتراض أن السجل المقاس متغير عشوائي بقيم متوقعة معطاة من النموذج النظري وبتباين معلوم، فانه بالإمكان تحديد التقدير الإحصائي والحجم الجزئي للمسام وللمكونات المعدنية وتباين تلك الكميات.

وباستخدام معادلة توازن المواد في مجموعة المعادلات الإتفاقية، كمعادلة اتفاقية تؤول إلى إنحراف معياري صفري، يقل التباين بالنسبة للمسامية والعناصر المعدنية الأخرى. كما أن استخدام معادلة توازن المواد يستوجب التعامل مع المحددة الدورية بدلاً عن المحددة المعتادة.

ABSTRACT

In the determination of the porosity of the rock bulk drilled through the oil well, we compare the measured physical quantities and the calculated quantities given by the idealized, theoretical rock model. The comparison gives stochastical equations. Supposing that the measured log is a random variable with expected value given by the theoretical model and with known variance, we can determine the statistical estimation of the volume fraction of the porosity and other mineral components and the variance of those quantities. If we involve the exact, theoretical material balance equation into the system of stochastical equations, as a stochastical equation tending to zero standard deviation, then the variance of the porosity and other mineral components will be decreased. The consideration of the material balance equation requires the use of the cyclical determinant instead of the regular determinant.

INTRODUCTION

An important task of the log survey is to determine the porosity of the rock bulk drilled through the oil well. For this reason the minerals of the given rock matrix are grouped on the basis of their physical properties which affect the given logs, and the task is to determine the volume fractions of each group. During this process all available logs which help to solve the problem are put in use.

The method of finding the volume fractions is to compare the measured physical quantities with the calculated quantities given by the theoretical description of idealized rock model containing the parameters.

Because of various reasons (see [1]) the measured quantity is a stochastical one; accordingly we have to consider it as a random variable. If only the first moments are known (i.e. the expected values) of these random variables, then as it is proved in [2], we can not get information on the rock volumes. Nevertheless knowing the second moments as well (by which the standard deviations of these variables also will be known) and assuming that, first, the measured quantities vary around the values of the theoretical model and second, rather large (infinitely large) number of observations, there is a possibility to restore the volume fraction parameters of the theoretical model. Enforcing the first assumption and taking into consideration that in a given depth point only a few stochastical observations are available, it is clear that the parameters to be determined are also stochastical quantities i.e. we can

* Petroleum Research Centre, P.O. Box 6431, Tripoli, G.S.P.L.AJ.

determine only the probability of the event, that the parameter belongs to a given section around the expected value.

During the process we consider the theoretical rock model which is defined by us, however not arbitrarily, as a certain model and not as a stochastic model. As a consequence, there is a basic difference between the stochastic vector equations of measured and theoretical values, and between the exact, purely theoretical material balance equation.

In the limited number of publications dealing with the complex process of interpretation of well log measurements (see e.g. [4], [5]) we could not find information about the fact, or about the manner of the above mentioned difference. According to our knowledge, part of log analysts proceed the following way: first they determine the volume fractions without using the material balance equation, and after that, they interpret the difference of the sum of components from the unit as a quantitative description of the quality of the interpretation process. We consider this procedure from a logical point of view, as a correct one, but not as the possible complete one, because it's inaccurate to ignore the only certain, exact equation in the determination of the volume fractions of mineral components.

FORMULATION OF THE PROBLEM AND SUMMARY OF THE STATISTICAL RESULTS

Let us suppose that we have m different log data at given depth point of the bore hole, and we divided the unit volume of the surrounding rock for $k+1$ mineral components as $x_0, x_1, \ldots, x_k$ so that

$$x_0 + x_1 + \cdots + x_k = 1 \tag{1}$$

(We begin to enumerate the x_i components from zero, because we suppose that the rock has k solid components and x_0 is the fluid component, which is in our case the main parameter, namely the porosity).

Let us suppose that each log can be described as a linear function of unknowns $x_0, x_1, \ldots, x_k$, and all the measured logs are random variables according to the one dimensional normal distribution, with known standard deviations $\sigma_1, \sigma_2, \ldots \sigma_m$ and with expected values which are the results of that linear function in a certain, unknown point $\hat{x}_0, \hat{x}_1, \ldots, \hat{x}_k$. Normalizing the coefficients of the first linear function and the first measured value by σ_1, the seconds by σ_2 and so on, we can write

$$\begin{aligned} a_{10} \cdot \hat{x}_0 + a_{11} \cdot \hat{x}_1 + \cdots + a_{1k} \cdot \hat{x}_k &= b_1 \\ a_{20} \cdot \hat{x}_0 + a_{21} \cdot \hat{x}_1 + \cdots + a_{2k} \cdot \hat{x}_k &= b_2 \\ &\vdots \\ a_{m0} \cdot \hat{x}_0 + a_{m1} \cdot \hat{x}_1 + \cdots + a_{mk} \cdot \hat{x}_k &= b_m \end{aligned} \tag{2}$$

where a_{ij} is the normalized jth coefficient of the ith linear tool response function, b_i is the normalized ith log, which is not necessarily the originally measured log, but a modified form of that, after different transformations like filtering, depth matching, etc.

According to the assumptions the right hand side of (2) is a random variable with normal distribution. The expected value of each b_i is the expression standing on the left hand side of the ith equation and the variance of each b_i is 1. In addition we shall suppose, that for any $i \neq j$ the b_i and b_j stochastic variables are independent of each other.

Denoting the set of matrices containing n rows and m columns by $\mathcal{M}_{n,m}$ and the set of vectors, containing k elements as one row by $\mathcal{V}_k$, the set of equations (2) can be rewritten in matrix form

$$A\underline{\hat{x}} = \underline{b} \tag{3}$$

where $A \in \mathcal{M}_{m,k+1}$, $\underline{b} \in \mathcal{V}_m$, $\underline{x} \in \mathcal{V}_{k+1}$ and $\underline{\hat{x}} = (\hat{x}_0, \hat{x}_1, \ldots, \hat{x}_k)$.

We consider that the statistical results, which can be summarized as follows, are well known to the reader (see e.g. [3], page 260). Keeping in force all the assumptions related to $\underline{b}$, among all the linear statistical estimations $\underline{\alpha}$ for the solution of the overdetermined linear system of equations (3), the smallest variance given by that $\underline{\alpha}$, which satisfies the Gauss normal equation

$$(A^T \cdot A)\underline{\alpha} = A^T \cdot \underline{b} \tag{4}$$

(A^T is the transpose of matrix A).

In this case $\underline{\alpha}$ is unbiased estimation of $\underline{\hat{x}}$, i.e. the expected value of $\underline{\alpha}$ is $\underline{\hat{x}}$.

In this way according to Cramer's rule, the ith component of $\underline{\alpha}$ can be calculated from

$$\alpha_i = \frac{\det[(A^T \cdot A)^i]}{\det[(A^T \cdot A)]} \tag{5}$$

where $A^T \cdot A \in \mathcal{M}_{k+1,k+1}$; $(A^T \cdot A)^i \in \mathcal{M}_{k+1,k+1}$ is the matrix in which the ith column of the matrix is changed to the right hand side vector of (4). The variance of α_i, denoted $D^2(\alpha_i)$ can be calculated from

$$D^2(\alpha_i) = \frac{\det[(A^T \cdot A)_{ii}]}{\det[(A^T \cdot A)]} \tag{6}$$

where $A^T \cdot A$ is the same as above, and $(A^T \cdot A)_{ii} \in \mathcal{M}_{k,k}$ is the matrix obtained from the matrix $A^T \cdot A$ by omitting it's ith column and it's ith row.

INVOLVEMENT OF THE MATERIAL BALANCE EQUATION INTO THE STOCHASTICAL SYSTEM

During the investigation of the system of equations (2) all the equations had a statistical character. However, equation (1), is not stochastical but a certain one. The simplest way to eliminate the difference between equation (1) and equation (2), is to handle the right hand side of (1) as a stochastical variable with unit expectancy and with a variance, which tends to zero.

Accordingly let ξ_e be a stochastical variable with Gaussian normal distribution, with the expectation value 1, and with the variance σ^2,

$$M(\xi_e)=1; \quad D^2(\xi_e)=\sigma^2 \tag{7}$$

Denoting $1/\sigma$ by s and so $s=1/\sigma$ tends to infinity, then the stochastical variable $s\cdot\xi_e$ shows the behavior

$$M(s\cdot\xi_e)=s; \quad D^2(s\cdot\xi_e)=1 \tag{8}$$

Handling equation (1) in this way, now the system of equations (1) and (2) for $x_0, x_1, \ldots, x_k$ looks like

$$\begin{aligned} &s\cdot x_0+s\cdot x_1+\cdots+s\cdot x_k=b_0\\ &a_{10}\cdot x_0+a_{11}\cdot x_1+\cdots+a_{1k}\cdot x_k=b_1\\ &\quad\vdots\\ &a_{m0}\cdot x_0+a_{m1}\cdot x_1+\cdots+a_{mk}\cdot x_k=b_m \end{aligned} \tag{9}$$

where

$$b_0=s\cdot\xi_e \tag{10}$$

We shall apply the same statistical results for the system of equations (9), which have been applied for the system (3). Accordingly, taking the special structure of (9) in consideration, in analogy with (4), the unbiased statistical estimation $\underline{\beta}$ of $x_0, x_1 \ldots x_k$ of (9) fulfills the equation

$$(A^T\cdot A+s^2\cdot E)\cdot\underline{\beta}=A^T\cdot\underline{b}+s^2\cdot\underline{e} \tag{11}$$

where $A\in\mathcal{M}_{m,k+1}$ is the matrix of equation (2), $\underline{b}\in\mathcal{V}_m$ is the vector on the right hand side of the same equation. $E\in\mathcal{M}_{k+1,k+1}$ is the matrix each element of which is unit, while s is given by (10). In the case when s tends to infinity, the estimation $\underline{\beta}$ of (9) and (10) gives the statistical estimation of the system consisted of (1) and (2).

So, in full analogy with (5) and (6) we get

$$\beta_i=\lim_{s\to\infty}\frac{\det[(A^T\cdot A+s^2\cdot E)^i]}{\det[(A^T\cdot A+s^2\cdot E)]} \tag{12}$$

and

$$D^2(\beta_i)=\lim_{s\to\infty}\frac{\det[(A^T\cdot A+s^2\cdot E)_{ii}]}{\det[(A^T\cdot A+s^2\cdot E)]} \tag{13}$$

(Note that according to (11) at the calculation of the numerator of (12) the $(A^T\cdot A+s^2\cdot E)^i$ matrix preserves its structure, having the s^2 second term after replacing the ith column by the right hand side of (11), because the right hand side has the same second term).

The limit process in (12) and (13) can be derived in a simple form. On the basis of algebraic type results given in the Appendix, the derivation gives us the following final form for the statistical estimation $\underline{\beta}$:

$$\beta_i=\frac{\text{cycl det}[(A^T\cdot A)^i]}{\text{cycl det}[(A^T\cdot A)]} \tag{14}$$

and

$$D^2(\beta_i)=\frac{\text{cycl det}[(A^T\cdot A)_{ii}]}{\text{cycl det}[(A^T\cdot A)]} \tag{15}$$

where all the matrices in square brackets are exactly the same as in formulas (5) and (6), but instead of the regular determinant, β_i and $D^2(\beta_i)$ can be expressed by the "cycl det" operator, which is defined as follows:

For an arbitrary $C\in\mathcal{M}_{n,n}$ matrix cycl det is the sum of n determinants:

$$\text{cycl det } C=\sum_{i=1}^{n}\det[C_i] \tag{16}$$

where $C_i\in\mathcal{M}_{n,n}$ is developed from C by replacing its ith column by $\underline{e}\in\mathcal{V}_n, \underline{e}^T=(1, 1\ldots, 1)$.

Comparing (14), (15) with (5), (6) we can say, that the effects of consideration of the material balance equation in statistical estimation of volume fraction parameters, is that instead of the regular determinant calculation, we have to calculate the cyclical determinant of the same matrixes.

EXAMPLES

First we illustrate how the two different approaches work on a simplified "artificial" case. The rock matrix consists of the quartz component only. Our task is to determine the porosity filled up by interstitial water, using the acoustic, density and hydrogen index logs, and to determine the standard deviation (the square root of the variance) of this quantity, which displays a Gauss normal distribution

as a result of the assumption that the measured logs show Gauss normal distribution as well.

Table 1a shows the slowly changing, or the so called zone parameters of each rock component for each log and the standard deviations of the measurements.

The calculated results for the standard deviation of the porosity are given in Table 1b using the three different possible combinations from the three different logs, without the use of (formula (6)) and with the use of (formula 15)) of the material balance equation. It can be noticed that the standard deviation is decreasing in all cases as a result of the presence of the material balance equation. The largest decrease is shown by the (HI, Δt) pair, while the most accurate way of solving the porosity determination, using two out of the three logs above, is offered by the (HI, ρ_b) combination.

The second example is a more complex one from the practice of geophysical interpretationl. Here the bore hole intersects fractured granite rocks while the fractures are partly filled with zeolite as a result of hydrothermal processes. We have neutron density (ρ_b), neutron porosity (HI), acoustic (Δt), photoelectric index (P_e) and two different spectral gamma ray (Th and K) logs. According to these conditions quartz (Qz), feldspar (FP), mica and heavy minerals (M & Hm), zeolit (Zeo) and total porosity (ϕ_t) filled up by interstitial water are the main mineral groups in the volumetric rock model. The upper part of Table 2 contains the zone parameters and the standard deviations of the log measurements. The lower part of Table 2 shows the standard deviations of the volume fractions for each mineral group without and with the material balance equation taken into account. Comparison of the two last rows of Table 2 shows again that the uncertainty of the interpretation, belonging to a given level of probability (in our case, i.e. in the case of Gaussian distribution and standard deviation this probability level is 0.6827) decreases by involving the material balance equation into the estimation. This decrease is less in the case of Table 2, than it was in the case of Table 1, which is related to the fact that the dimension of the equation system, in the second case, is higher.

Table 1a. Slowly Changing Parameters of the Two Mineral Components Model

Tool	Mineral group		Standard deviation of the measurement
	Water	Quartz	
acoustic, Δt [μsec/foot]	185.0	52.0	5.0
density, ρ_b [g/cm^3]	1.08	2.65	0.05
hydrogen index, HI [dimensionless]	0.93	−0.02	0.01

Table 1b. Standard Deviation of Porosity Determination in Percentage Without and With the Material Balance Equation Being Taken into Consideration

Used logs	Standard deviation (%)	
	without	with
(Δt, ρ_b)	2.47	2.43
(HI, ρ_b)	1.92	1.00
(HI, Δt)	9.62	1.14

Table 2. Slowly Changing Zone Parameters of the Five Mineral Components Model and the Standard Deviation of the Volume Fraction in Percentage Without and With the Material Balance Equation Being Taken into Consideration

Tool		Mineral Group					Standard deviation of the measurement
		t	Q_z	FP	M & Hm	Zeo	
ρ_b [g/cm^3]		1.08	2.65	2.55	3.01	2.11	0.05
HI [dim. less]		0.93	−0.02	−0.03	0.05	0.01	0.01
Δt μsec/foot]		185.0	52.0	55.0	41.0	60.0	5.0
Pe [barn/electron]		1.13	1.85	2.86	4.2	1.78	0.5
Th [ppm]		2.6	1.8	17.0	40.0	50.0	1.0
K [dim. less %]		0.68	0.68	7.0	4.0	7.0	1.0
Standard deviation %	without	1.03	6.09	8.32	5.68	6.98	
	with	1.00	5.51	8.29	3.79	4.86	

SUMMARY

In calculating the volume fractions of mineral components by means of complex well log interpretation, the accuracy of the determination of these fractions can be increased by involving the material balance equation into the interpretation system. The calculation of the standard deviations of the volume percentages becomes only slightly more difficult, as a result of taking the material balance equation into consideration. Whereby the regular determinant is replaced by the cyclical determinant operation. Practical examples show, that in some cases the increase in accuracy is significant.

ACKNOWLEDGEMENT

I would like to thank Mr. Mustafa Idris, the General Manager of the Petroleum Research Centre for Providing the opportunity to continue this research.

The continuous stimulating consultation with Prof. Zoltan Barlai which helped considerably in the process of this study is highly acknowledged.

REFERENCES

[1] Theys P., 1988, Log Quality Control and Error Analysis: A Prerequisite to Accurate Formation Evaluation, Eleventh European Formation Evaluation Symposium.

[2] Halfin L.A., 1958, Informacionnaja teorija interpretacii geofzicsszkih iszledovanij [The Information Theory of the Interpretation of Geophysical Investigation], (in russian): D.A.N. CCCP T 122 No. 6 [Reports of the Academy of Sciences of USSR, Volume 122, No. 6].

[3] Vincze I., 1968, Matematikai statisztika ipari alkalmazasokkal [Mathematical Statistic with Industrial Applications], (in hungarian), Muszaki Konyvkiado, Budapest: Technical Publishing Company).

[4] Rodriquez E., A. Mezzatesta, D. Tetzlaff, 1989, Determination of Statistical Confidence Intervals for Petrophysical Formation Properties: SPWLA Laser Symposium, London.

[5] Mayer C., A. Sibbit, 1980, Global, a New Approach to Computer processed Log Interpretation, 55th Annual Conference of Society of Petroleum Engineers, Dallas.

APPENDIX

Here we dicuss the limit process used in the derivation of formulas (14) and (15).

Let $C \in \mathcal{M}_{n,n}$ be an arbitrary matrix and $E \in \mathcal{M}_{n,n}$ the matrix, each element of which is the unit. Then for any number p

$$\mathrm{dt}(C+pE)=p\cdot\mathrm{cycl\ det}\ C+\det C \tag{a1}$$

here we use the notations used in the paper. The definition of the $\mathcal{M}_{n,n}$ can be found before expression (3) and the definition of the operator "cycl det" is given by formula (16).

For providing eq. (a1) let us denote the column vectors of C by $\underline{c}_1, \underline{c}_2, \ldots \underline{c}_n$ and the columns of E by $\underline{e}$. Then we have

$$\det(C+pE)=\det(\underline{c}_1+p\cdot\underline{e}_1\underline{c}_2+p\cdot\underline{e}\ldots,\underline{c}_n+p\cdot\underline{e}) \tag{a2}$$

where on the right hand side there is just another notation for the matrix under discussion.

For two arbitrary vectors $\underline{a}, \underline{b} \in \mathcal{V}_n$ and for any index i

$$\begin{aligned}&\det(\underline{c}_1,\underline{c}_2,\ldots,\underline{c}_{i-1},\underline{a}+\underline{b},\underline{c}_{i+1}\ldots,\underline{c}_n)\\&\quad=\det(\underline{c}_1,\underline{c}_2,\ldots,\underline{a},\ldots,\underline{c}_n)\\&\qquad+\det(\underline{c}_1,\underline{c}_2\ldots\underline{b},\ldots\underline{c}_n)\end{aligned} \tag{a3}$$

and for any indexes $i, j,; i \neq j$

$$\begin{aligned}&\det(\underline{c}_1,\underline{c}_2,\ldots,\underline{c}_{i-1},p\underline{e},\underline{c}_{i+1},\ldots,\\&\quad\underline{c}_{j-1},p\underline{e},\underline{c}_{j+1},\ldots,\underline{c}_n)=0\end{aligned} \tag{a4}$$

The two last identities express obvious behavior of the determinant operation, they can be proved easily starting from any definition of the determinant.

Repeatedly applying (a3) to the right hand side of (a2) we get the sum of 2^n number of determinants, but on the basis of (a4) only $n+1$ out of them differ from zero:

$$\begin{aligned}&\det(C+pE)=p\cdot\{\det(\underline{e},\underline{c}_2,\ldots,\underline{c}_n)\\&\quad+\det(\underline{c}_1,\underline{e},\underline{c}_3,\ldots,\underline{c}_n)+\cdots+\det(\underline{c}_1,\underline{c}_2,\ldots,\underline{e})\}\\&\quad+\det(\underline{c}_1,\underline{c}_2,\ldots,\underline{c}_n)\end{aligned} \tag{a5}$$

This shows the validity of (a1).

Now let $C \in \mathcal{M}_{n,n}, B \in \mathcal{M}_{k,k}$ and $E_n \in \mathcal{M}_{n,n}, E_k \in \mathcal{M}_{k,k}$ be the matrices each element of which is unit and suppose cycl det $B \neq 0$.

Then on the basis of (a1) the equation

$$\lim_{p\to\infty}\frac{\det(C+p\cdot E_K)}{\det(B+p\cdot E_n)}=\frac{\mathrm{cycl\ det}\ C}{\mathrm{cycl\ det}\ B} \tag{a6}$$

is a simple limit process for the ratio of linear, related to p, functions.

PRJ, Vol. 5 (January 1993); P. 6–15, 16 FIGS.

DESCRIPTION OF NATURALLY FRACTURED RESERVOIRS FOR SIMULATION STUDIES

J.C. Sabathier*

وصف المكامن المتشققة طبيعياً لأجل المحاكاة

جين كلود ساباتير

تتناول هذه الورقة المكامن المتصلة تشققاتها في وضع شبكي (على الأقل في بعض أجزاء الحقل) عندما تكون المواد الهيدروكربونية في مكامن داخل الوطاء.

الهدف من وصف المكامن المتشققة طبيعياً لأجل المحاكاة هو تعريف المعايير التي يلزم ادخالها في المحاكي. وتقدم هذه الورقة أولاً أنماط المخططات المكمنية والمحاكيات المتوفرة حالياً ثم تناقش كيف يتم اختيار الأنسب بناءاً على خصائص المكمن. كما أخذ في الإعتبار خصائص التشققات والوطاء (المسامية، النفادية، النفادية النسبية، الضغوط الشعرية). ويتم تحليل تعريف أبعاد كتل الوطاء وذلك بمراجعة مختصرة للوسائل المتاحة. وقد تم التركيز على أهمية الإستمرارية العمودية الجزئية المتناسقة. كما تم القاء بعض الضوء على استعمال محاكيات المكامن مع الوصف المكمني.

ABSTRACT

In this paper we only consider fractured reservoirs where fractures are inter-connected in a continuous network (at least in some part of the field) and where mobile hydrocarbons are initially in place in the matrix.

The description of naturally fractured reservoirs for simulation studies aims to define the parameters which have to be input in the simulator. Thus this paper first presents the different types of reservoir schematisations and the types of simulators which are presently available and discusses how to choose the most appropriate one according to the reservoir characteristics. Characterization of the fracture and matrix media (porosity, permeability, relative permeabilities, capillary pressures) are furtherly considered. The definition of the geometry of the matrix blocks is analyzed with a brief review of the presently available tools. The importance of an even partial vertical continuity is emphasized. Possible influence of the gas-oil interfacial tension, diffusion, and thermal convection is also presented. Some considerations are also given on the use of reservoir simulators in connection with reservoir description.

*FRANLAB, France.

RESERVOIR SCHEMATISATION

The presence of fractures has been observed in many hydrocarbon reservoirs of different lithologies. Fractures crossing the wellbore improve the well productivity which may be out of range with the potential corresponding to a matrix reservoir. However fractures may also result in a specific reservoir behaviour needing a specific modelling. We shall consider only this case which happens when fractures are interconnected, creating a continuous network, or when they are parallel and extended, *and* if the matrix contains mobile hydrocarbons. In such cases, most of the initially in place hydrocarbon volume is in the matrix rock while fractures provide the main path for fluid flows in the reservoir. The first objective in characterizing a reservoir where fractures have been identified is to know (from geology and well tests) if it has to be considered as a fractured reservoir as defined above.

Natural fractures happen in brittle rocks under the action of stresses connected to:

- the tectonic history of the formation (folding, faulting...),
- erosion resulting on unloading and expansion of the upper sediments,

– compaction of shales (loss of water, mineral changes...).

Tectonic fractures are generally organized in systems, i.e. in sets of parallel fractures whose intersections delimit parallelepiped matrix blocks. Examples of conjugated patterns have been reported by Stearns and Friedman [1]. However, due to other sources of fracturing, reservoir heterogeneities and further diagenetic phenomena, the actual network of open fracturs in a reservoir may be very irregular without defining a recognizable block structure (Fig. 1).

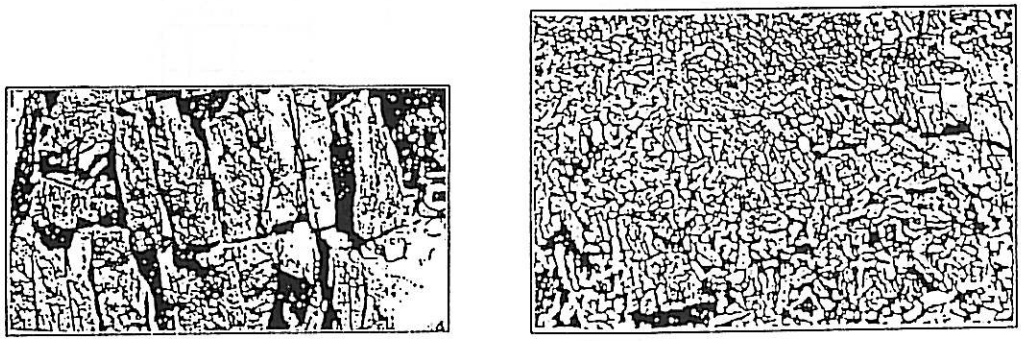


FIG. 1. Fractured formations (outcrops).

In the numerical models a very smplified assumption has to be made. Fractures are assumed to be distributed among rectangular systems respectively parallel to the coordinates planes (X–Y, Y–Z, Z–X). Thus the matrix (Fig. 2) may be distributed in:

– rectangular parallelepipeds (sugar cube model),
– horizontal layers (plate model),
– vertical columns (pillar model).

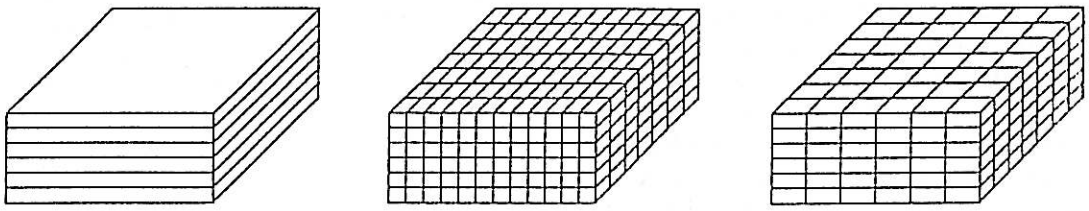


FIG. 2. Fractured reservoir schematization.

TYPE OF SIMULATOR

There are basically two types of simulators to model fractured reservoirs. They correspond to different types of reservoirs and consequently it is necessary to identify first the reservoir type to be able to select the most suitable simulator (or to know the limitations of the only available one). The two types of simulators are:

– the "column type" models,
– the "dual porosity" models.

The column type models (ref. 2, p. 704–749) favor the vertical description of the reservoir and assume that fluid flows are mainly in the vertical direction. The field is represented by a few sectors (which may communicate). In each sector the fractures define a series of identical piles of blocks. There is a complete vertical fluid segregation in the fractures and no horizontal flow in the fractures of a given sector. The model computes for one (or a few) column(s) of each sector the fluid flows within each matrix block and between each block and the surrounding fractures (Fig. 3–4). Each block is fully characterized and subgridded while fractures, in the model, are used to impose boundary conditions for matrix flow computations. Reimbibition of the oil flowing out of a block in the next lower block may be included in the computations.

Dual porosity models (Fig. 5) view the reservoir as made of two continuous media. Space is discretized in cells, for numerical purposes, which are reservoir space elements. All the fractures of the cell are represented by a "fracture node" and all the matrix medium is represented by a "matrix node". The two nodes are generally both located at the center of the cell. Fluids are flowing between fracture nodes according to the characteristics of the fracture system. Fluid flows are also computed between the fracture and matrix nodes of the same cell (dual permeability models also allow fluid flows between matrix nodes). Such models are well suited to describe 3-D flows in the fracture system but have to simplify the matrix-fracture flow computations. The matrix node represents several matrix blocks (supposed to be

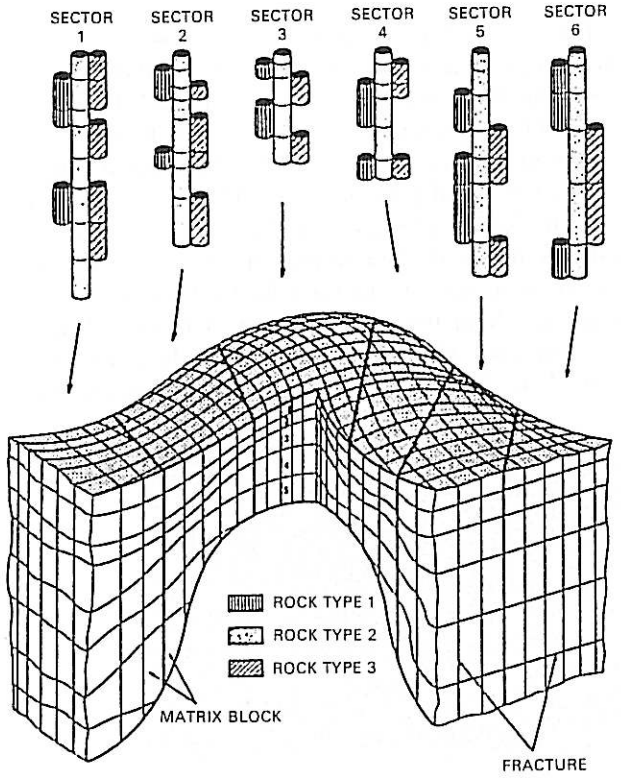


FIG. 3. Representation of a reservoir with a column type model.

identical) areally and vertically distributed within the cell and the model can only compute the behaviour of an "average" block. These computations are indeed critical and valuable results may be expected only if the model is able to directly account for the different driving forces (viscous, capillary and gravity forces), gravity and capillary being mandatory [3]. Generally the block is not subgridded (this is theoretically possible when the cell height is equal to the block height) thus pseudo-steady state conditions are assumed to prevail for matrix-fracture flow computations. Reimbibition between blocks in a cell, which is a very important phenomenon, cannot be directly computed and is even not at all accounted for in several models which consequently must be carefully used.

The column type models are consequently preferable when large sectors of the field behave uniformly, which is generally the case when the fractures are sufficient to provide a high overall permeability. In such reservoirs this type of model is specially recommendable when the pseudo-steady state hypothesis for matrix-fracture flow is no more acceptable because of the block size and many result in significant errors.

The dual porosity models are preferable when gradients develop over the field so that the hypothesis of homogeneous sectors with horizontal gas-oil and

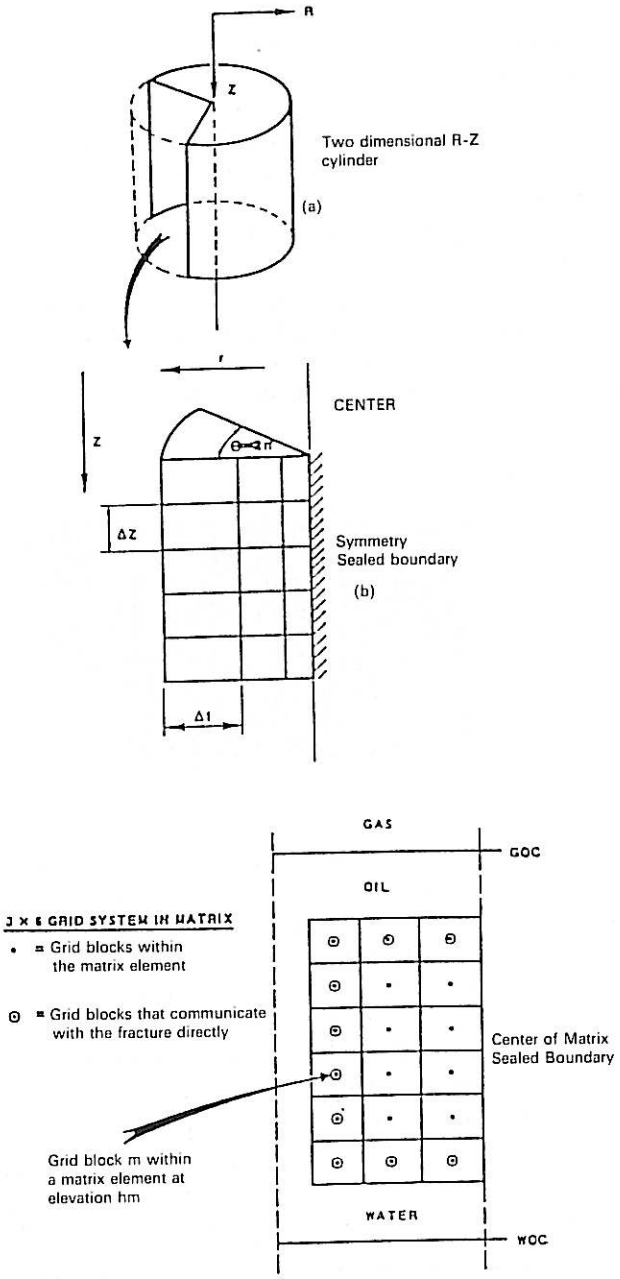


FIG. 4. Matrix element in a column type model.

oil-water interfaces is no more valid. This is generally the case when fractures are small and/or irregularly distributed.

It must also be observed that if the matrix block has a sufficient permeability it is rapidly (within a time step) in equilibrium with the surrounding fractures so that the reservoir may be viewed as one composite system which can be simulated with a conventional single porosity model. Indeed petrophysical properties input in this model will have to account for the fractured character of the reservoir (pseudos) which means that the reservoir description must be the same as when using a dual porosity model.

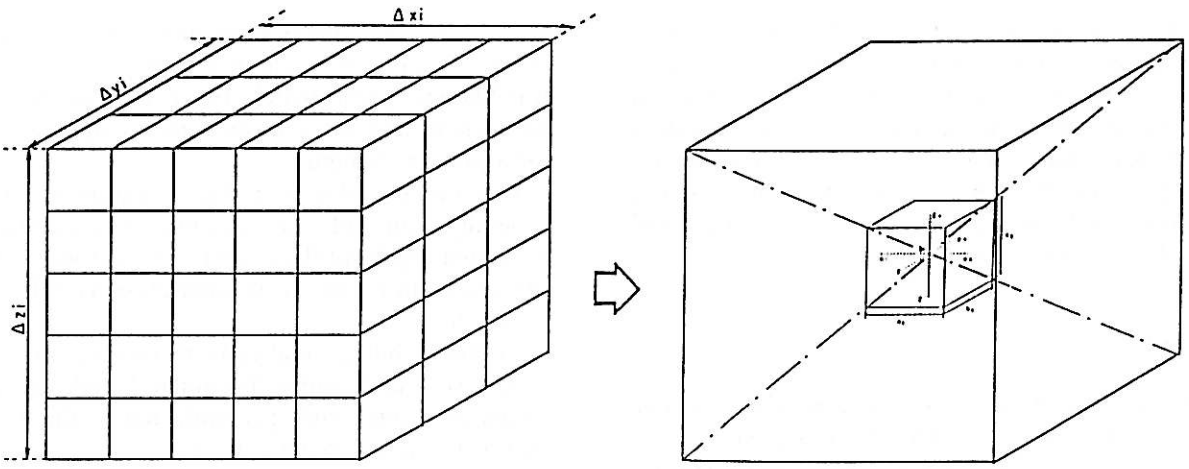


FIG. 5. Dual porosity model.

CHARACTERIZATION OF THE FRACTURE SYSTEM

In a dual porosity model the fracture system is characterized by the same parameters as the porous medium in a single porosity model. In the column type model only the porosity versus depth is needed.

The degree of fracturation may widely vary all over the field with even possibly unfractured areas. When the well pattern is large, which is common in fractured fields, these variations of fracturation may be difficult to map. Programmes have been written to help determine the intensity of fracturing resulting from the tectonic history of the reservoir. The successive shapes of the reservoir are determined and the resulting stresses are computed by the model from the mechanical properties of the rock [4]. The model maps a "relative chance of fracturation" index corresponding to the maximum stresses computed in simplified hypothesis (Fig. 6).

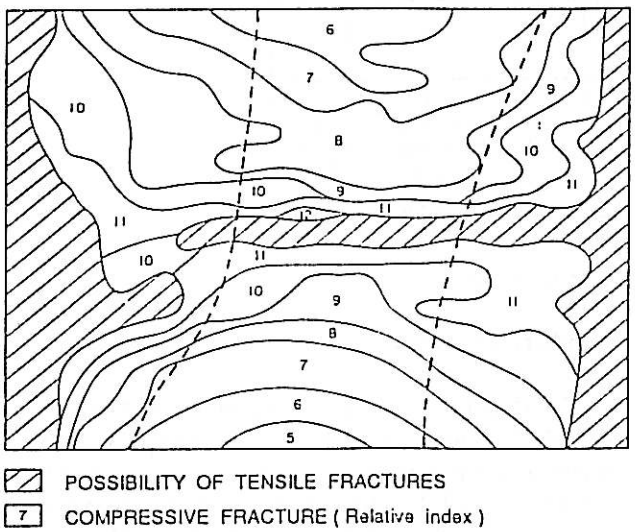


FIG. 6. Chance of fracturing index.

Permeability

This parameter is normally computed from the well productivity and the production test analysis. When interpreting production tests, attention has to be paid to the flow pattern in the reservoir (radial or vertical) mainly if there is a gas-cap (Fig. 7). If the fractures are organized in systems of parallel fractures of possibly different permeability (different fracture thickness and/or density) as evidenced by well interferences, the grid will be accordingly oriented to be able to model the fracture network anisotropy.

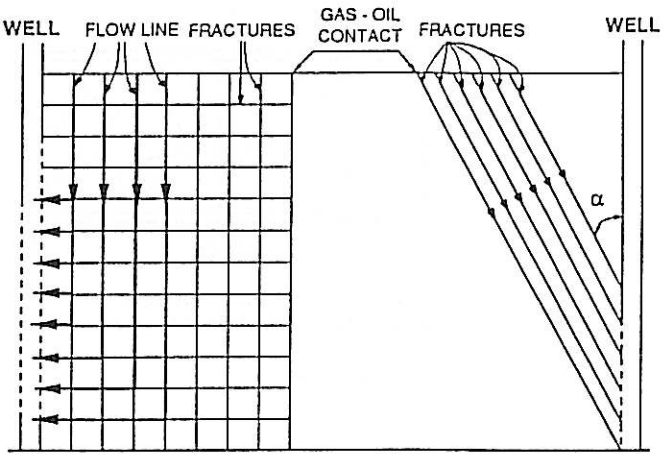


FIG. 7. Fluid flow through fractures around a well.

Another possibly important problem is the variation of the fracture permeability with the reservoir pressure. In 1975 Jones published results of laboratory experiments [5] showing a strong permeability decrease with pressure. However in actual fields this decline is generally much lower, if any. Only a periodic survey of the well productivity indices may allow to estimate the reduction of permeability with pressure in the fracture system.

Vertical permeability may be difficult to evaluate when vertical fractures have a limited extension. In carbonate reservoirs, stylolites may sometimes interrupt fracture interconnections and consequently limit the vertical connections. In some cases they are also related to some type of fracturing. Thus in carbonate reservoirs stylolites are an important feature and should be carefully described.

Porosity

The fracture porosity is low, generally less than 0.3%, and cannot be directly measured by any present logging tool. Applying Poiseuille's law for laminar monophasic flows between plates gives a relationship between the fracture thickness and its permeability. Thus knowing the fracture density and supposing they are identical, it is theoretically possible to compute the porosity of the fracture system from its equivalent permeability (porosity is proportional to the cubic root of the permeabiliy). Practically, even in the most favorable cases (large and extended fractures), very erroneous figures may be derived from this computation due to the fact that all the fractures do not contribute to the flow towards the producing well (and thus the geometry of the fracture network must be known) and that a large part of the pressure drop may be due to fracture joints, restrictions, fracture tortuosity....

Interpretation of well production tests with a dual porosity flow model may provide, in the best cases, the value of the ω parameter which is practically the ratio of the fracture to matrix expansibilities. As the porosity and compressibility of the marix may be independently estimated, the expansibility of the fracture medium may be computed. Thus the fracture porosity could be computed if the compressibility was known. Unfortunately this parameter may vary between 10 and 100 fold the values commonly used for a porous medium.

Fracture porosity is in fact a parameter which, generally, can only be adjusted by matching the measured depths of the gas-oil and water-oil levels in the observation wells i.e. in connection with the other parameters.

Compressibility, as already mentioned, may vary over a very large range. Formulae based on experiments with constraints perpendicular to the fracture planes give a maximum value [5].

Relative Permeabilities

Within one single fracture the relative permeability concept is not valid as one fluid is flowing either discontinuously (droplets, bubbles) or under film flow conditions. In a fracture network, experiments have shown that each fluid flows separately through a definite set of fractures. Relative permeabilities can be defined only at the scale of the network and are generally considered as equal to the phase saturations. However the performances of a fractured medium worsen when fractures have different thicknesses (Fig. 8).

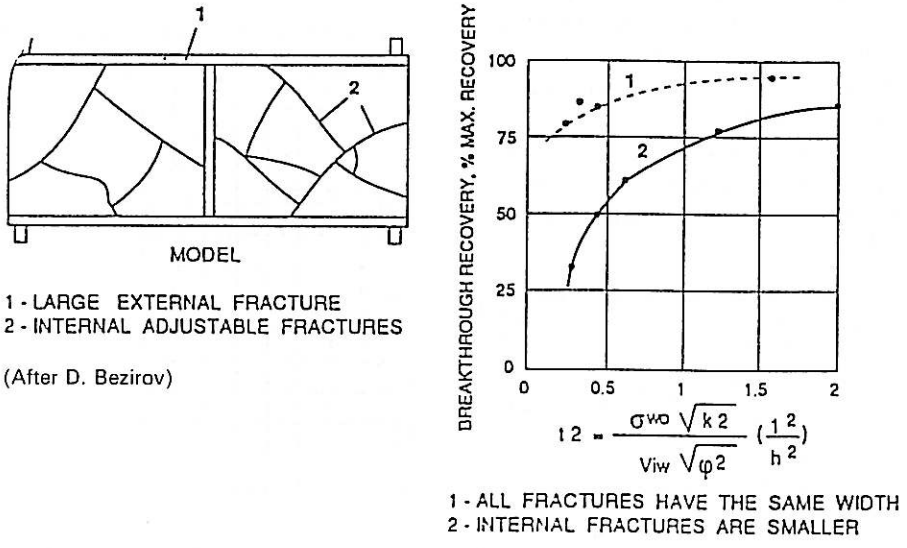


FIG. 8. Effect of fracture heterogeneity.

Capillary Pressures

The thickness of the wetting phase film which is adsorbed along the walls of the fracture is only a fraction of micron, thus, in most cases, the residual saturations and the capillary pressures may be ignored.

Some models are however using both gas-oil and oil-water capillary curves in the fracture medium

for numerical reasons. Pseudo curves may also be input for capillary pressures and relative permeabilities.

CHARACTERIZATION OF THE MATRIX MEDIUM

Rock Properties

The usual rock characteristics (porosity, permeability, capillary and relative permeability curves ...) have to be input in the model and are measured with the same techniques as in porous single porosity reservoirs. However as well production tests cannot be used to compute the matrix permeability, this parameter has to be measured on cores and/or estimated by using log transforms.

If an initial gas-cap exists or if a secondary gas-cap is anticipated, it is mandatory to accurately measure the gas-oil capillary pressure curve. This parameter is generally neglected in single porosity reservoirs but, in fractured reservoirs producing by gas-cap expansion (with or without gas injection) and having relatively small blocks, the final recovery is directly dependent on its value (Fig. 9).

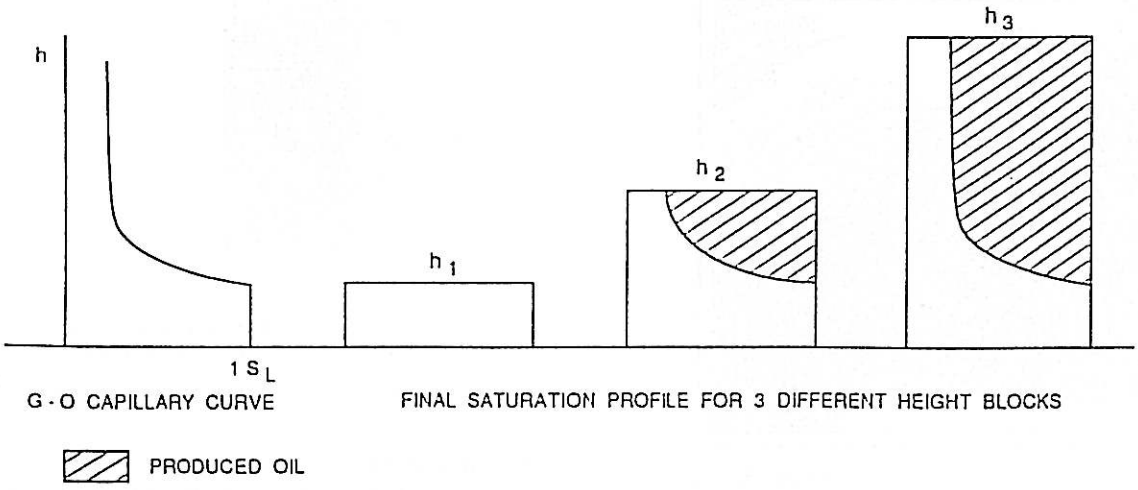


FIG. 9. Gravity drainage. Block height influence.

Relative permeabilities and capillary pressure curves have to be measured in drainage and imbibition conditions if the movements of the gas-oil and water-oil contacts in the fractures may reverse in some parts of the field. Wettability is an important problem each time fractures are invaded by water.

Matrix Block Size

Defining the geometry of the marix blocks is a key problem to solve when building a fractured reservoir model. A geological picture must be first obtained and furtherly simplified to meet the simulator input requirements.

Block description is obtained either from the observation of outcrops of the same formation (Fig. 1) or/and from the determination of the location, orientation and dip of the fractures crossing the wells.

The fracture network observed on outcrops is indeed not necessarily identical to the one prevailing in the reservoir even in the same geological formation and mainly if there is evidence of an irregular fracturing. However outcrop observations may help to relate the fracture characteristics to the lithology and the structural location.

Aerial photography allows to define regional fracture trends (Fig. 10) which may be considered as no depth dependent in tectonically undisturbed areas.

Core description, when recovery is good, provides the fracture density, their length, dip, strike (oriented cores), filling materials.... Fracture induced by drilling may be recognized and discarded. Thickness of the fractures in reservoir conditions cannot be obtained from cores.

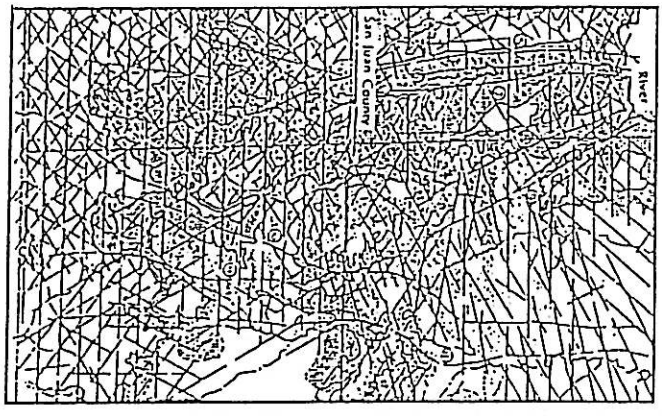


FIG. 10. Regional joint trend.

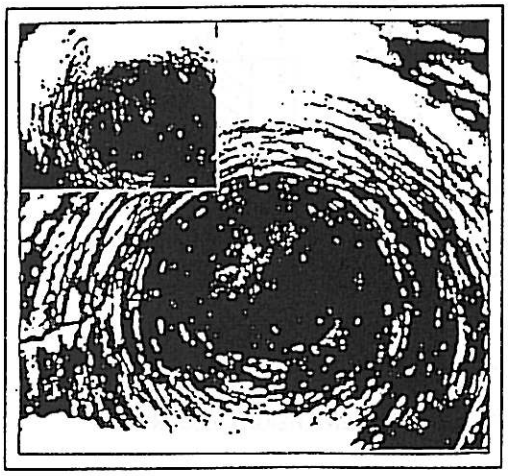
Mud losses are also an indication of large fracturing, recorded on surface. However it does not allow to determine the number and location of the fractures.

Seismic profiles may also sometimes indicate fractured zones. In such cases it may help to determine the extension of the fractured areas but cannot indeed give information on the block size.

Several types of measurements in the well may be used (generally in conjunction) to locate the fractures more or less precisely:

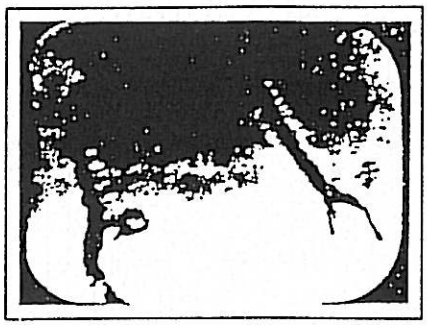
- In some specific cases camera pictures may give very valuable information (Figs. 11–12) but the constraints of photography make it rarely possible.
- Production logging (flowmeters, temperature logs) may indicate the location of open fractures if the hole conditions are good.
- Many efforts have been done to use electric logs (mainly the sonic log) for detecting fractures. Most of them are reported in [2], [6], [7]. In some specific conditions good results are obtained by interpreting log "anomalies" as fractures. However there is no general validated method and such interpretations have to be checked and calibrated on a regional basis. Schlumberger uses a programme (DETFRA) which computes a probability index of fracturing from individual indices defined with the available logs.
- Two tools give "false pictures" of the wellbore with visualisation of the fractures:
  - the Borehole Televiewer (BHTV) which is an ultrasonic scanner providing a sonar type picture (Fig. 13),
  - the "Formation Micro Scanner"™ (Schlumberger) which combines the reading of dense arrays of electrical sensors set on the pads of a four arm caliper (Fig. 14).

  Pictures given by these two tools are generally very clear and allow to make the same measurements as on cores. However they must be closely analysed to detect "false fractures" corresponding to pictures generated by other heterogeneities.



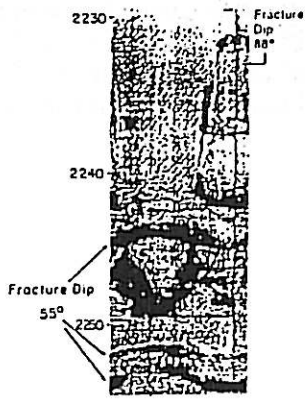
(After Fons)

FIG. 11. Photograph of fracture obtained with a borehole camera.



(After ref. 6, p. 25)

FIG. 12. TV pictures in Emeraude field wells.



(After Kai Hsu et al) JPT, June 1987

FIG. 13. BHTV log.

- Production test analysis are sometimes used to define an "average" block height. In favorable cases the dual porosity flow model allows to compute the value of the parameter $\lambda = \alpha \cdot (km\hat{}2) \cdot (rw\hat{}2)/kf$ where α is a geometric factor equal to $12/(hm\hat{}2)$ in the plate model (hm = thickness of the matrix bed). α (dimension $1/L\hat{}2$) is dependent upon the block shape. On the other hand as only monophasic flows are analysed by this method it should be at best possible to approach an "equivalent" length (volume/surface ratio) of the block, which is not enough to characterize the matrix medium.

When all the information about well fracturing are obtained, they are processed in order to get a space description of the fracture system and a definition of the matrix blocks as consistent as possible

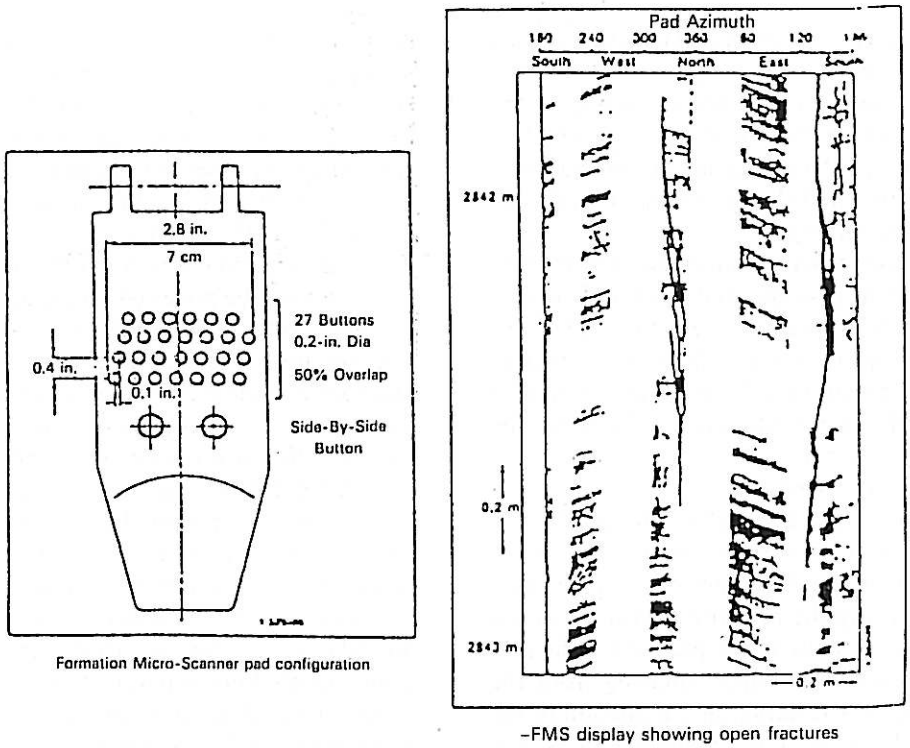
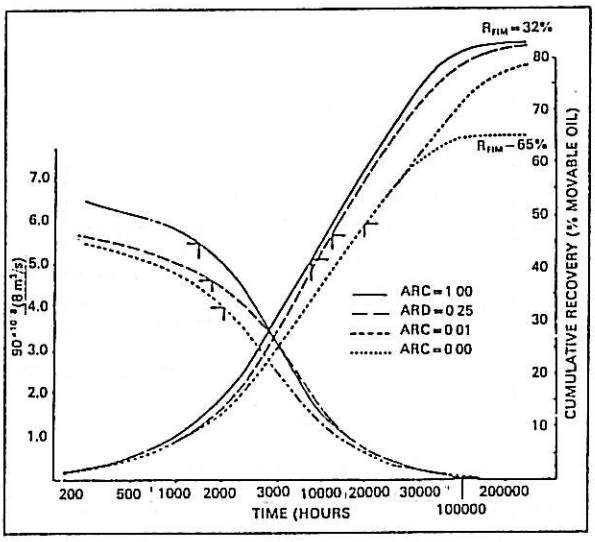


FIG. 14. FMS log.

with *all* the available data. When a complete information is availabe a statistical processing may be necessary to define the characteristics according to depth, lithology.... It must also be reminded that very few subvertical and practically no vertical fractures have a chance to be observed in a well.

The next step is to simplify the geological description according to the model input requirements. When fractures are large and extended they often clearly define a pattern which may be easily schematized by one of the accepted model pictures (plates, columns or sugar lumps). When fractures are small and short they are also irregular and the typical form of the blocks is no more obvious. A very important parameter to evaluate is the partial continuity which often exists in such reservoirs. This continuity, mainly in the vertical direction, is critical for the recovery by gravity drainage as even a limited unfractured section between two blocks may give (Fig. 15) practically the same performances as a full vertical connection [8]. It is the author's opinion that very often such reservoirs are simulated with a sugar cube scheme using too small blocks and that a column type model should be more appropriate. It must be kept in mind that each time fractures are invaded by gas, gravity drainage is the main recovery factor and the final recovery depends on the block height compared to the extension of the capillary transition zone.



ARC = Area of contact (fraction) between the two blocks (After ref. 8)

FIG. 15. Partial block continuity.

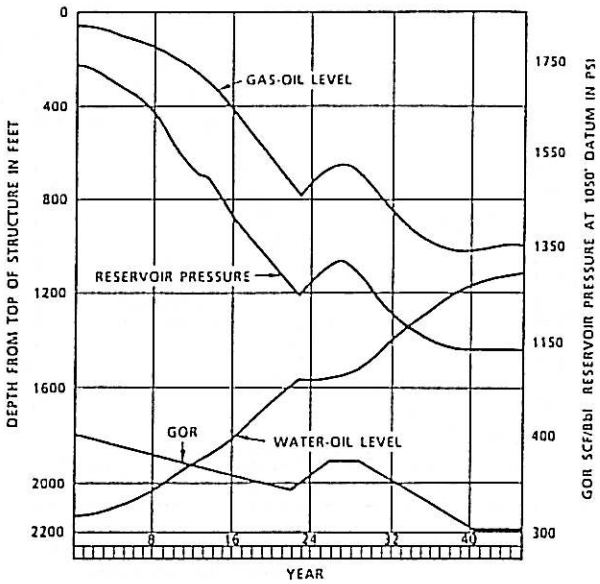
OTHER PARAMETERS

Among the other parameters which have to be defined in any simulation but which have a specific importance for fractured reservoirs, we have mentioned the gas-oil capillary curve. This one is not only dependent on the matrix rock but also on the *gas-oil interfacial tension*. This one is pressure and gas composition

dependent. The increase of the interfacial tension when pressure decreases may be very significant and may largely modify the final oil recovery. In such cases the model must account for this variation. Similarly if an external gas is injected the interfacial tension may vary with gas composition and the model has to make the corresponding computations.

Diffusion is a slow process and, consequently, may often be neglected in conventional reservoirs as it is efficient in only a small volume close to the fluid fronts. In fractured reservoirs the distance from matrix rock to the next fractures remains small and diffusion may be an efficient displacement mechanism between the fracture and marix media.

In highy fractured reservoirs, *thermal convection* is acting in the fracture system, resulting in initially uniform oil properties all through the column. If convection is fast enough, it maintains uniform oil properties in the fractures during the reservoir depletion with a bubble-point pressure close to the pressure at the gas-oil contact. Gas is consequently diffusing from the matrix to the fractures resulting in a reduction of the matrix oil bubble-point. This phenomenon is evidenced by a production at declining GOR from the bottom part of the oil column down to pressures much lower than the initial bubble point (Fig. 16). Before



(After ref. 2, p. 771)

FIG. 16. Example of convection-diffusion effects.

production, convection may be evidenced by a constant temperature all through the reservoir.

RESERVOIR SIMULATION AND RESERVOIR DESCRIPTION

Due to the large number of parameters involved in a fractured reservoir model, it is unrealistic to expect that matching the field past performances will allow to fix the reservoir properties at their correct values. The history match is only a way to check the consistency of the reservoir characterization previously performed by the reservoir engineer and to adjust some parameters within a range of acceptable values and according to the general reservoir picture. If such a "limited" adjustment is not sufficient, the general description must be reviewed before any new simulation.

On the other hand, engineers sometimes hesitate to embark in a fractured reservoir simulation because data are not sufficient to describe the fracture system. It is clear that large efforts have to be done to improve this description and modern tools may be very helpful. However, even in cases where the fracture system is poorly known (lack of data, very complicated system), a numerical simulation may give significant results if properly used.

A first use of the simulation is to test on a limited model (cross section, sector) the relative importance of some poorly known parameters (within their realistic range of variation) in order to decide a cost effective programme of data acquisition. The second use of the model is as an engineer's tool in a reservoir engineering study. When requested by his management, the reservoir engineer must provide production profiles, development/completion programmes.... Answers must be given even if very few or/and very poor data are available. The model is a way to forecast the field behaviour according to the best reservoir picture based on the presently available data and engineer's experience. The model has to be chosen to represent the actual physical phenomena even if their magitude remains uncertain. In other words very simplified data should never give accurate detailed results but may provide a satisfactory estimate of the whole reservoir behaviour if the relative influence of the different drive mechanisms is correctly evaluated *and* if these mechanisms are correctly simulated. If a field is considered as a fractured field (as above defined) the different forces (viscosity, capillarity, gravity) do not act as in a single porosity reservoir and a specific model is better suited to simulate it even with poor data. The model is also able to give an estimate of the uncertainties by modifying the relative importance of these forces (specific coefficients have been introduced in our model, FRAGOR, to easily and independently modify each force and thus to be able to run rapidly several sensitivity cases).

CONCLUSIONS

The description of a fractured reservoir is indeed a challenge. Important improvements of the logging tools help to a better analysis and improvements of the simulators and allow a better computation of the

different fluid flows in such reservoirs. The main point to clarify before starting to use a numerical model is to know if the fractures which have been recognized to exist are developed in a system such that the reservoir may be viewed as a series of separated matrix elements. If so, the engineer's judgement remains the key factor to correctly choose the suitable conceptual description (cubes, columns, layers). This choice is basic as it may strongly modify the way the different forces competitively act in the reservoir.

REFERENCES

[1] Stearns, D.W. and Friedman, M.: "Reservoirs in Fractured Rock," 1972, A.A.P.G., Reprint Series N°21.

[2] Saïdi, A.M.: "Reservoir Engineering of Fractured Reservoirs," 1987, Total Edition Press.

[3] Quandalle, P. and Sabathier, J.C.: "Typical Features of a New Multipurpose Reservoir Simulator," paper SPE 16007 presented at the Ninth Symposium on Reservoir Simulation held in San Antonio, TX, Feb. 1–4, 1987.

[4] Quiblier, J.A.: "Contribution à la prévision de la fissuration en zone faiblement tectonisée," Thesis presented at Univ. of Paris (France), 1971.

[5] Jones F.O. Jr.: "A Laboratory Study of the Effects of Confining Pressure on Fracture Flow and Storage Capacity in Carbonate Rocks,," *J. Pet. Tech.* (Jan. 1975) 21–27.

[6] Reiss, L.H.: "Reservoir Engineering en Milieu Fissuré," 1980, Editions Technip, Paris.

[7] Van Gof-Racht T.D.: "Fundamentals of Fractured Reservoir Engineering," 1982, Elsevier Seientific Publishing Co.

[8] Festoy, S. and Van Gollf-Racht, T.D.: "Gas Gravity Drainage in Fractured Reservoirs Through New Dual-Continuum Approach," SPERE (Aug. 1989) 271–78.

PRJ, Vol. 5 (January 1993); P16–21, 5 FIGS, 2 TABLES.

CORROSION CONTROL IN DEFA WATERFLOOD SYSTEM

M.A. Elarabi*

التحكم في التآكل بمنظومة حقن المياه بحقل الدفا

ميلود عبد السلام العربي

تقدم الدراسة أمثلة عملية لإختيار أنسب المثبطات الكيميائية لمعالجة التآكل في منظومة حقن المياة بحقل الدفا باستخدام أجهزة قياس ربطت على وصلة جانبية قريبة من رأس أحد الآبار المنتجة للمياه لكي تطابق متغيرات ظروف التشغيل المختلفة.

ABSTRACT

Practical methods are presented to select different biocides and corrosion inhibitors for the DEFA waterflood system. It involves the use of side stream bacteria detection on mounted probes and potentiodyne technique on the well head of a source water well. These methods are well suited for application in systems where high frequency fluctuations in process variables are encountered. Field examples of corrosion problems and solutions are cited.

INTRODUCTION

The efficient and continuous operation of waterflood system requires complete control of corrosion mechanism which could lead to failure in its components from source water wells to injection wells. The corrosion in DEFA waterflood system is severe because hydrogen sulfide, carbon dioxide, sulfate reducing bacteris (SRB) and changing velocity are involved.

Before adopting a solution to corrosion problems, a complete understanding of each corrosion mechanism and the possibilities of combined mechanisms are necessary.

Field study is conducted to investigate the corrosivity of Zelten formation water utilized in pressure maintenance plan in DEFA oil field. These tests include evaluation of different biocides to mitigate the growth of SRB within the waterflood system and corrosion inhibitors to reduce the corrosion rate. SRB growth can cause a highly localized pitting corrosion in the distribution network and the corrosion product (iron sulfide) contributes to formation plugging, injectivity decrease, corrosion cell formation (different aeration) and survival of anaerobic SRB. Therefore bacterial growth should not be tolerated in the water injection system.

* El Fateh University, Chemical Engineering Department, G.S.P.L.A.J.

SYSTEM DESCRIPTION

The DEFA waterflood system (Fig. 1) was originally designed in the early 1970's with a capacity of 250,000 barrels of water per day. In the late 1970's, the system was expanded to an ultimate capacity of 500,000 bbls/day. In 1982, the booster station was expanded to provide the additional pressure required for water injection. However, with every attempt to increase the system pressure, numerous leaks occured on the trunk lines and distribution lines, particularly at the extremities where the velocity is less than 1 ft/sec (0.3048 m/sec). Most failures occur in the lower quadrant of the pipe with severe pitting corrosion under heavy iron sulfide scale build up. Waterflood production is divided on severe source wells (WSW) alternatively in operation. Water from source wells flows to pump station and via 24″ mainline and 16″ lateral to the injection wells. Filters are located at the wellhead and facilities for pigging the line are available. Because of present low production levels, only five water source wells are in operation producing a total of 225,000 bbls/day.

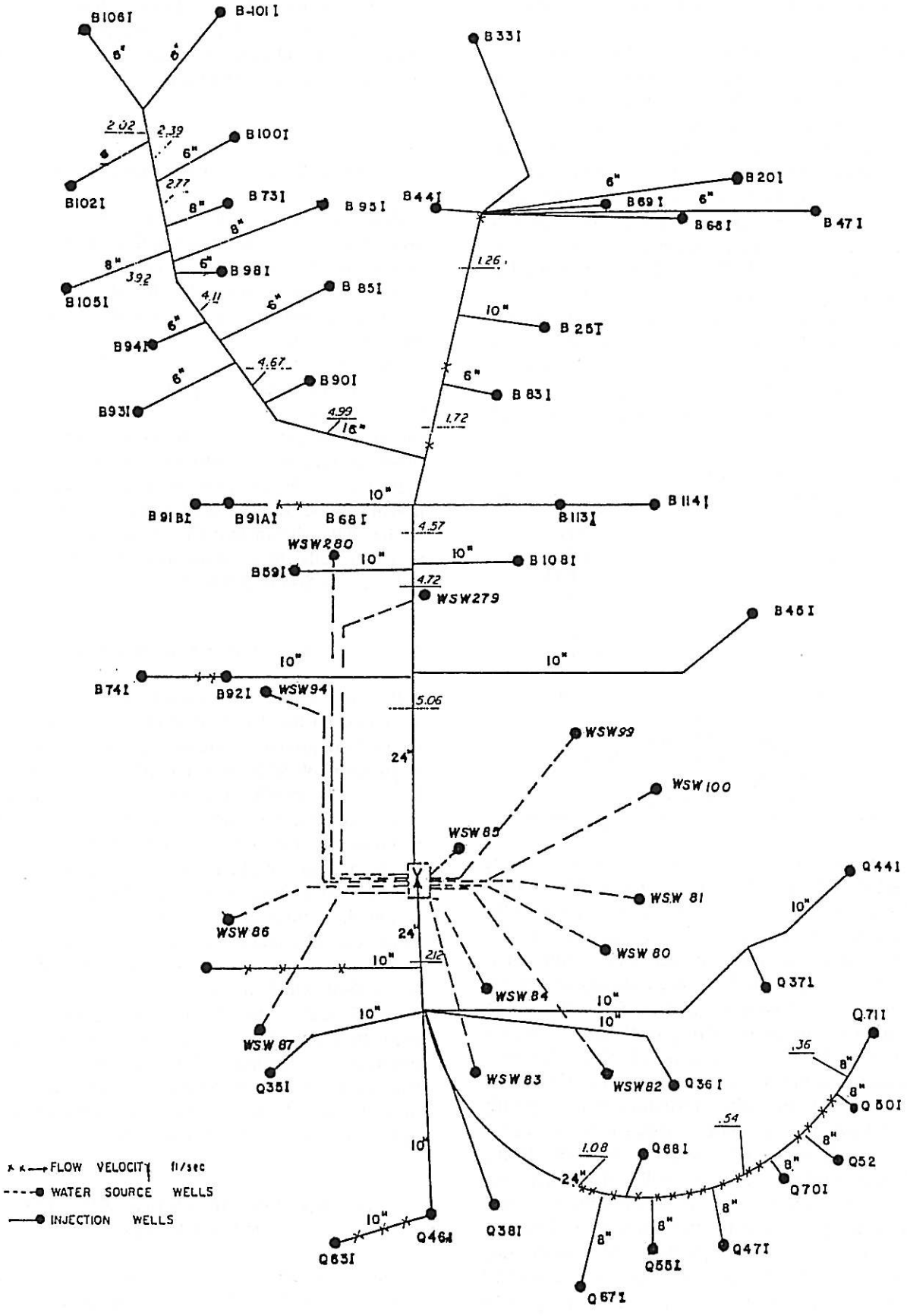


FIG. 1. DEFA water flood system.

WATERFLOOD CORROSION HISTORY

Injection water produced from Zelten formation is highly corrosive due to high temperature, H_2S and CO_2 content, Table 1 shows a typical water analysis for this water. Corrosion failures on the trunk lines started after few years of operation. Section of the pipeline inspected at the failure sites indicated that severe pitting under a heavy layer of iron sulfide scale is taking place. The iron sulfide layer is covered with a heavy layer of organic material, assumed to be inhibitor and crude oil. The crude oil is produced as slug with the produced water. A survey based on serial dilution method, conducted later, confirmed the existence of SRB throughout the system. Also, visual inspection of probes and coupons, used to monitor corrosion, showed black scale (iron sulfide) and highly localized pitting which support the idea that SRB

Table 1. Typical Injection Water Analysis (WSW 85)

Na^+	(mg/l)	4901.0
Ca^{++}	(mg/l)	571.0
Mg^{++}	(mg/l)	170.1
Ba^{++}	(mg/l)	0.13
Cl^-	(mg/l)	2389.0
HCO_3	(mg/l)	427.0
CO_3	(mg/l)	0.0
SO_4	(mg/l)	1379.0
PH	(units)	5.9
Talk	(mg/l)	700.0
H_2S	1–2 ppm (at well head)	
CO_2	4–5 ppm (at end of dist. lines)	
O_2	10–40 ppb	
Iron	300–400 ppm (as $CaCo_3$)	

is the main cause of corrosion. It was therefore decided that the possible approach would be to treat both the source water wells and trunk lines with the effective biocide available. This procedure was followed routinely at approximately one month intervals. The source wells have been closely monitored for recurrence of bacteria growth. Only WSW 279 was showing positive SRB growth and complete sterilization has not been achieved. Since this phenomenon doesnot exist in other wells, there is a possibility that the Zelten formation was originally free of SRB. Contamination appears to be caused from an external source near the wellbore during drilling or workover of some wells. Most likely, the WSW 279 is infected in the rathole area (the area between the pump and the bottom hole perforation). As a result of monthly pigging and biocide slug treatment for the 16″ and 24″ trunklines, a marked decline in corrosion rate planktonic (floating) SRB and H_2S levels was noted at the extremities of the system. As a result of continued trunklines leaks, the Company decided to replace the whole injection flowline network with cement mortar lined steel. This, however, will not eliminate further corrosion in source water and injection wells, or formation plugging reduction in water injectivity wells (due to SRB growth).

PLANKTONIC AND SESSILE SRB

Bacterial corrosion is actually caused by sessile anaerobic bacteria living under thick biofilm matrix, debris and sediments in the system, or accumulated corrosion product attached to the metal surface. The visible predominance of iron sulfide in the biofilm, adjacent to the heavily colonized corroded metal surface, is evidence of anaerobics. These anaerobic organisms are believed to play a predominant role in biological corrosion. Planktonic corrosion organisms simply represent a small proportion of the active sessile population of corrosion causing bacteria that happened to detach from the biofilm and enter the flowing phase at a particular point in time. Recent studies have shown that the sessile bacteria population (on cells/cm^2) outnumber the planktonic (as cell/cm^2) by 500 to 50,000 times.

EFFECTS OF BIOCIDES

Present methods of diagnosing bacterial corrosion are based on the detection of planktonic SRB whose intermitted presence indicates a much larger sessile population of SRB that actually live in the lower layers of the biofilm and cause corrosion. Thus the success of certain biocides currently used in the field is illusory in that contaminated systems are detected by the presence of planktonic SRB in injection water used for serial dilution test, and biocides are shown to kill these floating organisms, as indicated by the same test. The quick recurrence of planktonic SRB and continued corrosion, however, indicated that the sessile SRB, which actually caused corrosion, had not been affected by the biocides at the concentration used. Perceiving that a truly successful biocide must penetrate the biofilm and kill the innermost sessile bacteria is entirely misleading and biocide field use must be based on realistic assessment of efficacy against sessile bacterial population.

MECHANISM OF ANAEROBIC STEEL POPULATION

Sulfate reducers, typified by desulfovibrio desulfuricants, use the sulfate ion water as an oxidizing agent for the assimilation of organic matter. They also use high level of iron in their cell structure and are, therefore, prevalent in iron rich environments.

Sulfur reduced from sulfate reacts with available hydrogen and iron to form H_2S and FeS. Apart from the fact that H_2S is highly corrosive, the tying up of iron results in extra dissolution of the metal and thereby increases the corrosion rate.

BIOCIDE EFFICACY AGAINST SRB

Planktonic SRB

Since the early 1980's the API bottle test is used widely in field biocide study. The test procedure is designed with two controlled parameters, concentration and contact time. (Concentration tested are 0, 25, 50, 100, 150 and 200 ppm each at contact timt of 1, 3, 6, 12 and 24 hours). At each concentration and each contact time, serial dilutions of 1:10, 1:100, 1:1000 and 1:10,000 are used.

The problem with this method is the difficulty to find a uniformaly contaminated water sample within the waterflood. This is obvious since the method is based on planktonic bacteria which represent a small fraction of sessile bacteria.

More than five biocides are tested using the API method. Most of them show a complete kill at high concentration. Gluteraldehyde blends give consistently good kill and growth reduction results, while organic diamine acetate appears to be the alternative treating agent. For preliminary chemical screening purposes, this approach is probably adequate. Final biocide selection should include tests against surface associated populations and their effectiveness in penetrating biofilm layers on the metal surface.

Sessile SRB

A number of methods are developed in recent years to sample sessile SRB including; test spools or nipple on the by-pass loop (side stream), corrosion monitoring coupons, flush mounted coupons or probes, and a laboratory test loop. The last two methods are utilized to test the effectiveness of different biocides on sessile bacteria.

In the test loop procedure, a sample of water is used for developing SRB by incubation at 55°C for two days and adding a specific nutrient. Special bottles designed with a plastic probe are filled with the water. After 16 days of incubation time a biofilm is developed on the probes. Different biocides are added at various dosage and bottles are kept under agitation for 4 hours. The biofilm is scrapped from the probes into a sterile plastic bag containing 40 ml of sterile water. Finally 1 ml of water is inoculated for the SRB count. A summary of the result is shown in Table 2.

Table 2. Kill Test Against Planktonic and Sessile SRB

Biocide	Concentration (ppm)	Planktonic*	Sessile
A	100	−	+
	200	−	+
B	100	−	−
	200	−	−
C	100	+	+
	200	+	+
D	100	+	+
	200	+	+
E	100	+	+
	200	+	+
F	100	−	−
	200	−	−
BLANK 1		+	+
BLANK 2		+	+

* + Bottle turned black
− bottle not turned black

The side-stream loop consists of mounted coupons or probes which are exposed to water flowing through the system. A complex microbial biofilm develops and sessile bacteria population can be quantitatively recovered and analysed for total number of surviving bacteria on the metal surface at frequent intervals. This is part of continuing program and no complete data is available.

As shown in Table 2 both biocides B and F show a complete kill for planktonic and sessile bacteria. Biocide B is an aldehyde/ammonium salt derivative and biocide F is diamine active ingredient based derivative. This supports the original finding for biocide evaluation against planktonic SRB.

CORROSION INHIBITOR EVALUATION

To reduce the corrosion rate throughout the waterflood system and reduce the time required in routine chemical trials, the Potentiodyne analyser with conventional process (mild steel) is used.

The electrodes are equilibrated in the injection water under prevailing well head conditions as shown in Fig. 2. The scanning rate is kept at 4V/hr for all the runs on WSW 85. The procedure is typical of utilizing side-stream for inhibitor injection at different concentrations until practical predetermined level of corrosion rate is achieved. Each inhibitor is evaluated at three different concentrations 2, 4 and 6 ppm, and the corrosion rate at each concentration is measured at 0, 1, 3, 6 and 24 hours. However, due to iron sulfide deposition, the data at 24 hrs is not included in the evaluation. To prove it is the iron sulfide and not the filming ability of corrosion inhibitor, the corrosion rate without

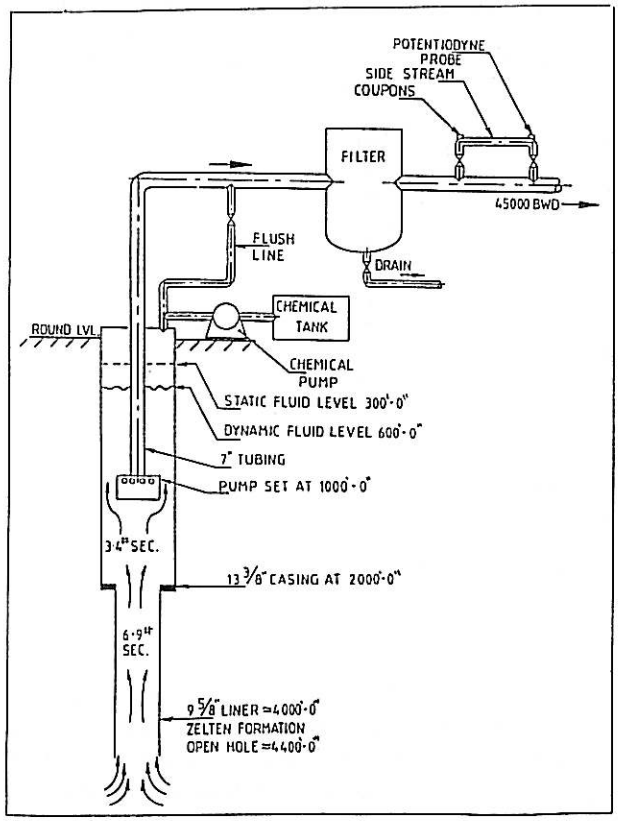


FIG. 2. Typical water source well.

inhibitor is reduced from 18 mpy to 13.6 mpy under the same conditions.

In comparison with the presumed practical and economical corrosion rate of 1 mpy, the result shows that corrosion inhibitors A, B, C and D are all effective at 6 ppm as shown in Fig. 3. However, this concentration is measured at the well head, and as we move farther from the injection point, this concentration diminishes due to filming properties of these inhibitors. Therefore, inhibitor B is not recommended for use at concentration below 4 ppm level as shown in Fig. 4. All chemicals are ineffective at 2 ppm as shown in Fig. 5.

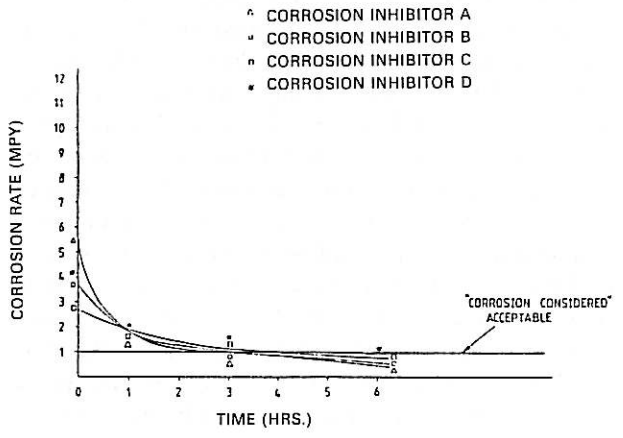


FIG. 3. Corrosion rate at 6 PPM.

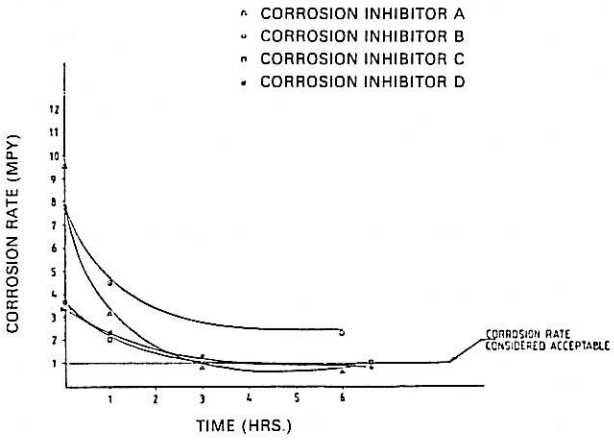


FIG. 4. Corrosion rate at 4 PPM.

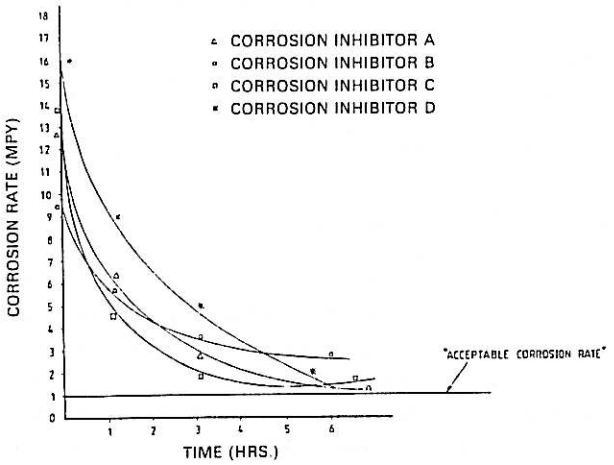


FIG. 5. Corrosion rate at 2 PPM.

ECONOMICAL PERFORMANCE EVALUATION

Both corrosion inhibitors A and C are superior to B. These two chemicals could be used at lower levels to achieve the same corrosion inhibition. Make-up injection point is necessary for chemical B to maintain a residual concentration of more than 4 ppm throughout the waterflood system. Except for corrosion inhibitor D (the highest price), the prices of the other three chemicals vary by only 5%.

CONCLUSIONS

- SRB are still present despite the regular biocide injection. Some source water wells are still giving positive growth and complete sterilization has not been achieved.
- Bacterial growth should not be tolerated in the water injection system as it may cause corrosion or formation damage.
- Bacterial corrosion is actually caused by sessile anaerobic bacteria living under a thick biofilm

matrix attached to the metal surface. Sessile bacteria population outnumber the planktonic 500–50,000 times.

- Biocide efficacy testing that only samples planktonic bacteria is entirely misleading, and biocides field use must be used on their efficacy against sessile bacteria.
- The investigation has shown that the potentiodynamic technique enables the influence of chemicals to be evaluated under field conditions in a short time, whereas, conventional methods would have required extended periods of testing.

ACKNOWLEDGEMENT

I thank Waha Oil Company, Corrosion Section and Technical Laboratory personnel for their assistance and support to complete this work.

REFERENCES

[1] D.P. Moore and Byars H.B., 1990, Field Measurements Involve Various Techniques, Oil and Gas Journal, 90.

[2] D.P. Moore and Byars G.B., 1990, Measurement Records Vital for Effective Program, Oil and Gas Journal, 97.

[3] E.L. Liening, 1979, Practical Applications of Electrochemical Techniques to Localized Corrosion Problems, Corrosion/79, Atlanta, Georgia, 78.

[4] E.Y. Chen and Chen R.B. Chen, 1984, Monitoring Microbial Corrosion in Oil Field Water Systems, JPT, 1171.

[5] I. Ruseska et al, 1982, Biocide Testing against Corrosion Causing Oilfield Bacteria Helps Control Plugging, Oil and Gas Journal, March 8, 253.

[6] J.G. Stoecker, 1984, Guide for the Investigation of Microbiologically Induced Corrosion, Materials Performance, 48.

[7] S.M. Gerchakov, Little B.J. and Wagner P., 1986, Probing Microbiologically Induced Corrosion, Corrosion, Vol. 42, No. 11, 689.

[8] W.P. Iverson, 1984, Mechanism of Anaerobic Corrosion of Steel by SRB, Materials Performance, 28.

PRJ, Vol. 5 (January 1993); P. 22–36, 12 FIGS.

POST-STACK DECONVOLUTION AND MULTIPLES ATTENUATION

M.M. Elazezi*

التخلص من الإنعكاسات السيزمية المتكررة باستخدام طريقة اللف العكسي (ديكونفولوشن)

محمد مسعود العزيزي

تعمل الإنعكاسات المتكررة الموجودة بالمعلومات السيزمية على حجب أسطح الإنعكاس الأساسية والمهمة ، لذلك فقد تم إجراء عملية تصفية لما بعد التكدس بتطبيق طريقة التصفية التوقعية (الإستقرائية) للمعلومات السيزمية النهائية للتخلص من هذه الإنعكاسات.

لقد تم حساب القياسات أو المعايير المطلوبة باجراء عملية المقارنة الذاتية ثمّ بعدها إختبار هذه القياسات على أجزاء من المقاطع السيزمية. تضمن الإختبار كيفية إختيار أحسن المقاسات المطلوبة مثل مسافة التنبؤ وطول المشغل الخاصة باجراء عملية التصفية (DECONVOLUTION) ، كما تم مقارنة المقاطع السيزمية قبل وبعد تطبيق المعايير المختارة.

أعطت المقارنة نتائج مشجعة جداً وذلك من خلال إبراز أسطح الإنعكاس المتميزة وطمس الإنعكاسات المتكررة.

إن التخلص التام من مثل هذه الإنعكاسات هو النتيجة المستهدفة ، ولكن يبدو أن الإنعكاسات المتكررة ذات نطاق كبير من الخواص ، ولذلك فانه يتم فقط التخلص من الإنعكاسات التي تتوافق مع المعايير والقياسات التي تم تطبيقها.

ABSTRACT

The presence of multiples on seismic data have obscured the recognition of primary reflection events of interest. Post-stack deconvolution was carried out using final-stacked seismic data. The predictive deconvolution technique is used for multiple suppression. The parameters were computed from autocorrelation functions and tested on different panels of the seismic sections. The Test include mainly the prediction distance and operator length to select the best parameters required to attenuate the existing multiples. The obtained sections were compared with the final sections before post-stack deconvolution was applied. The tested parameters gave very encouraging results by bringing out a distinctive reflector and suppressing multiples. Complete suppression of multiples is the desired result from the application of the selected deconvolution filter; however, multiples seem to exhibit a range of properties and so only those multiples which conform to the predicted assumptions were removed.

*Petroleum Research Centre, P.O. Box 6431, Tripoli, G.S.P.L.A.J.

INTRODUCTION

The seismic trace is assumed to be the convolution of seismic wavelet with the earth reflectivity function. The wavelet is composed of source signature, recording filter, surface reflections, and geophone response (Yilmaz, 1987). In order to remove the effect of the wavelet from the seismic trace, thus retrieving the earth's reflectivity function, a filter is required. Such a filter is called an inverse filter and the process is called deconvolution (Arya, 1979).

It has been mentioned by Yilmaz (1987) that post-stack deconvolution often has to be applied firstly, because deconvolution never can completely compress the basic wavelet, contained in the pre-stack, into spike, and secondly, since a CMP stack is an approximation to the zero-offset section, predictive deconvolution aimed at removing multiples may be a viable process after stack.

Hardy *et al.* (1989, 1990) and Hardy and Hobbs (1991) have mentioned that there is no optimum method for multiple suppression and have proposed the implementaton of stacking methods, moveout filters, predictive and adaptive deconvolution, and

wave equation. They suggested that multiple suppression should only be applied where necessary to improve interpretation; otherwise multiple identification schemes should be used. Post-stack deconvolution was carried out using final-stacked seismic data which still show high amplitude multiple interference which obscured the recognition of the primary reflection events. The predictive deconvolution technique (Peacock, 1969; Robinson, 1967, 1979) is used for multiple suppression. The parameters were computed from autocorrelation functions generated at several parts of the seismic sections and tested on different panels of these sections. The obtained sections were compared with the final sections before post-stack deconvolution applied. The comparison is to evaluate the effect of the designed deconvolution parameters on multiple attenuation and any improvement in data quality.

DECONVOLUTION TYPES

Different deconvolution types are being currently used for deconvolution of seismic data (Arya, 1979). These deconvolution types are designed to be applied before and after stacking depending on the type of multiples to be removed and the resolution required for data improvement. Deconvolution before stack is applied for wavelet shaping and attenuating multiple reflections. It has the advantage of operating upon traces before the normal move out correction has been applied. Deconvolution after stack is applied for further wavelet shaping and attenuation of multiples that remain after stack, taking into consideration the effect of the intermediate processing on the nature of the wavelet and its reverberant train of events.

The common types of deconvolution techniques include the following:

a. Wavelet deconvolution

This is a type of deconvolution which can be used to correct poor source signature and instrument phase distortion (Berkhout, 1977; Treitel, 1977). It involves changing the shape of the wavelet to some more desirable shape. The zero phase wavelet technique is used to produce a symmetrical wavelet with the energy concentrated in the centre lobe.

b. Adaptive deconvolution

This is a time-varying deconvolution method based upon adaptive linear filtering techniques (Griffiths *et al.*, 1977). The procedure consists of changing the prediction gap at every sample down the trace to find the best gap. Thus a different operator is used at each data point in the trace as the processor moves along the reflection seismogram. The technique can be very successful in suppressing multiples with a short time-varying period, but can become unstable in the presence of noise.

c. Spiking and predictive deconvolutions

Spiking deconvolution is a special case of predictive deconvolution in which the operator is to predict and remove energy starting at the first zero crossing after the zero lag value of the autocorrelation. The deconvolution technique has been discussed by Peacock (1966), Robinson (1967, 1979), and Yilmaz (1987). Predictive deconvolution is one of the most common seismic processing techniques. It is a very useful tool for multiple attentuation because multiples are highly predictable whereas the reflection series with which they are convolved is normally highly unpredictable. It is also used to increase the resolution of seismic data.

Predictive deconvolution is used in this study for investigating the possible improvement in data quality, as explained in the following section.

PREDICTIVE DECONVOLUTION

Design Principles

The filter assumes that a seismic trace is made up of two types of components, namely predictable and unpredictable. It is designed to predict, and then to remove, the predictable components from a trace. The predictable components consist of multiple and the effective source wavelet. The filter parameters are designed from the autocorrelation of a trace which shows the amplitude of the primary and multiples, and also the time extent of the existing multiples. When a primary is encountered on the trace the occurrence of the next primary cannot be predicted from it. This is because the reflection coefficient sequence is random and therefore has no time-invariant characteristics which enable such a prediction to be made. Predictive deconvolution has its power in wavelet resolution and multiple attentuation; however, it has its weaknesses as well. There are two main weaknesses. At early times and long offsets the multiple period is not constant and predicted times are inaccurate. Predictive deconvolution predicts the first multiple from the presence of the primary, the second multiple from the first multiple, and so on. If one number of the sequence is absent, weak, or distorted, the prediction will be in error accordingly.

Design and Operation

The Starting point of designing the operator is the autocorrelation function of the seismic trace. Autocorrelation of functions or time series occurs when the function or series is correlated with itself. The

autocorrelation of the seismic trace is always symmetrical about the zero shift and the zero shift value is always the maximum value (Dobrin and Savit, 1988). The desired effect of deconvolution is assessed by inspecting the autocorrelation function before and after the filter parameters are applied. The filter has three sections: the first is a single point of unit amplitude at time zero, the second is a sequence of zero amplitude samples forming the prediction distance, also known as the gap length and measured in milliseconds; the third part of the filter is the prediction operator length which is usually a few hundred milliseconds (Dobrin and Savit, 1988). The "Ethos" software is used to obtain the autocorrelation function. Different panels of seismic data were produced after the selected deconvolution parameters were applied to study their effect on multiple suppression.

Computational Procedures

a. Design gate (window)

The gate should cover the full seismic trace to obtain the greatest statistics, but it is limited to avoid high noise zones, and also may be different reverberation on early and later part of trace. Several design gates were tested to select the proper position of the time gate which covers the primary reflection events of interest and leads to the removal of multiples effecting these events. The trials involved changing the upper and lower time limits of the design gates. The choice of the proper design gate was started by the selection of three different gates (Figs 4, 5, and 6). The gates covered time intervals between 500–2500, 1000–2000 and 1000–3000 ms. The selection of three gates is to investigate the effect of the existing type of multiples at each gate, their time duration and also the effect of the applied deconvolution parameters in removing such effects and increasing resolution. The autocorrelation functions generated from the three selected design windows (Figs 1, 2, and 3) show slight differences regarding the extent of multiple duration which might be as a result of the types of multiples existing at each gate. They also show the effect of the applied deconvolution parameters on multiple attenuation. Figs. 4, 5, and 6 show a significant reduction in multiple energy in comparison with the same parts of the sections before filter parameters are applied. These sections also show the improvement regarding continuity and resolution of the primary events at each time interval. For example, an improvement is shown in Fig. 5 where onlap (white arrow) of the reflection event at 1650 ms is much clearer. The section with the 1000–3000 ms window (Fig. 6) is slightly crisper than the other two sections as shown at the time interval between 1600 and 1800 ms. The deconvolution parameters seem to have a similar effect in the three windows regarding multiple attenuation around and below the basement reflector at 1800 ms.

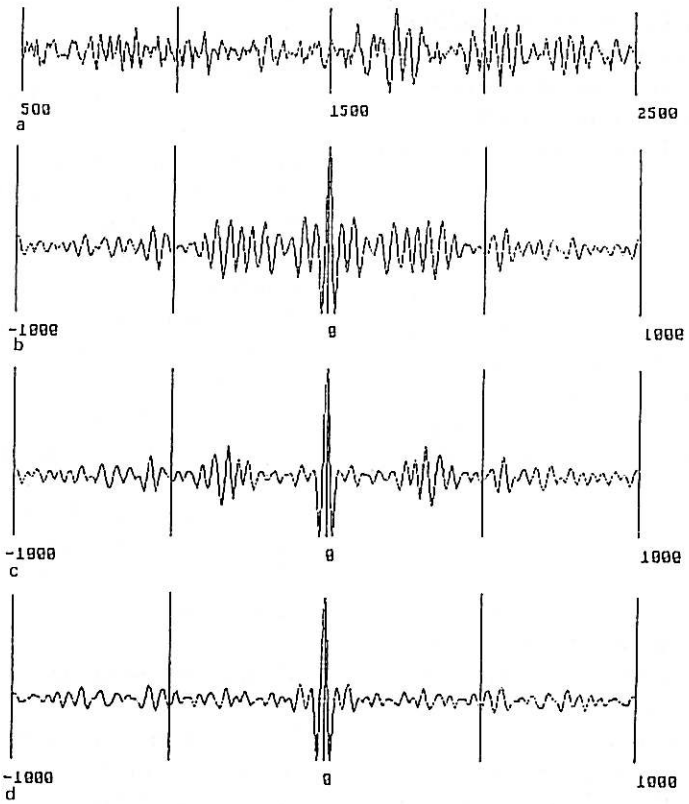


FIG. 1. Autocorrelation functions generated from a seismic section V100, CMPs 1790–1810, design gate 500–2500. (a) Input data trace widow. (b) Function of input traces before deconvolution. (c) After deconvolution of 32 ms gap length and 300 ms operator length applied. (d) After 600 ms operator length applied. Refer to FIG. 7 for deconvolution effect in multiples attentuation.

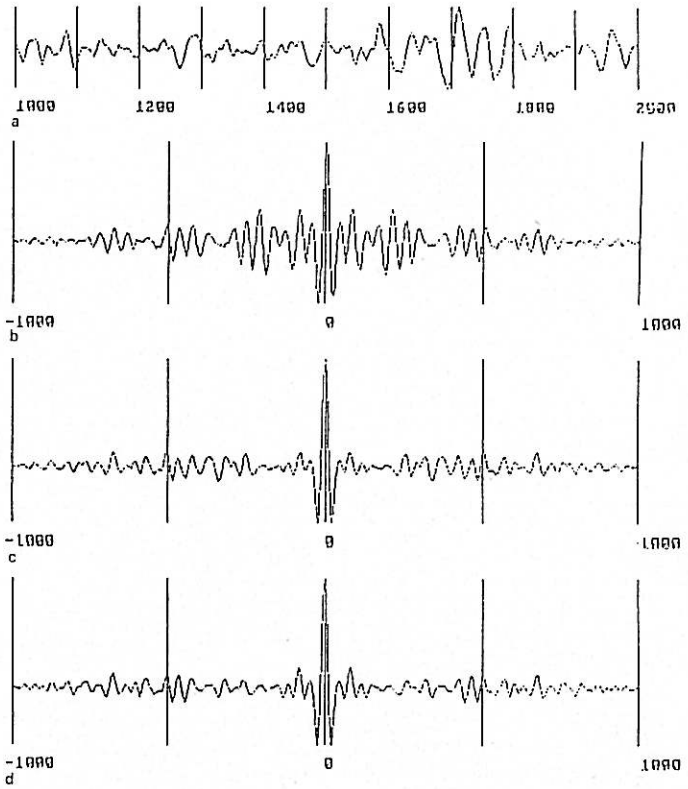


FIG. 2. Autocorrelation functions generated from a seismic section V100, CMPs 1790–1810, design gate 1000–2000. (a) Input data trace window. (b) Function of input traces before deconvolution (c) After deconvolution of 32 ms gap length and 300 ms operator length applied. (d) After 600 ms operator length applied. Refer to FIG. 8 for deconvolution effect in multiples attenuation.

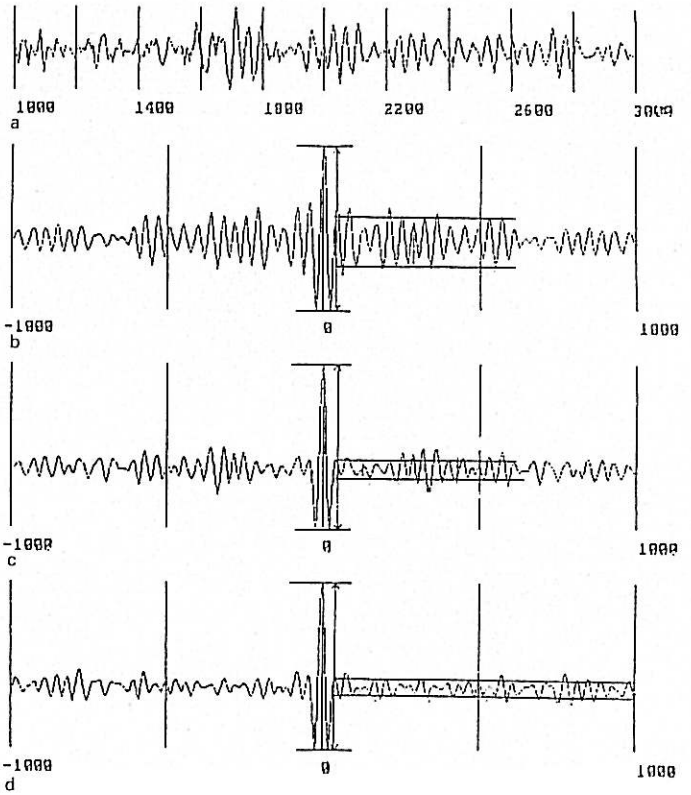


FIG. 3. Autocorrelation functions generated from a seismic section V100, CMPs 1790–1800, design gate 1000–3000. (a) Input data trace window. (b) Function of input traces before deconvolution. (c) After deconvolution of 32 ms gap length and 300 ms operator length applied. (d) After 600 ms operator length applied. Refer to FIG. 9 for deconvolution effect in multiples attenuation.

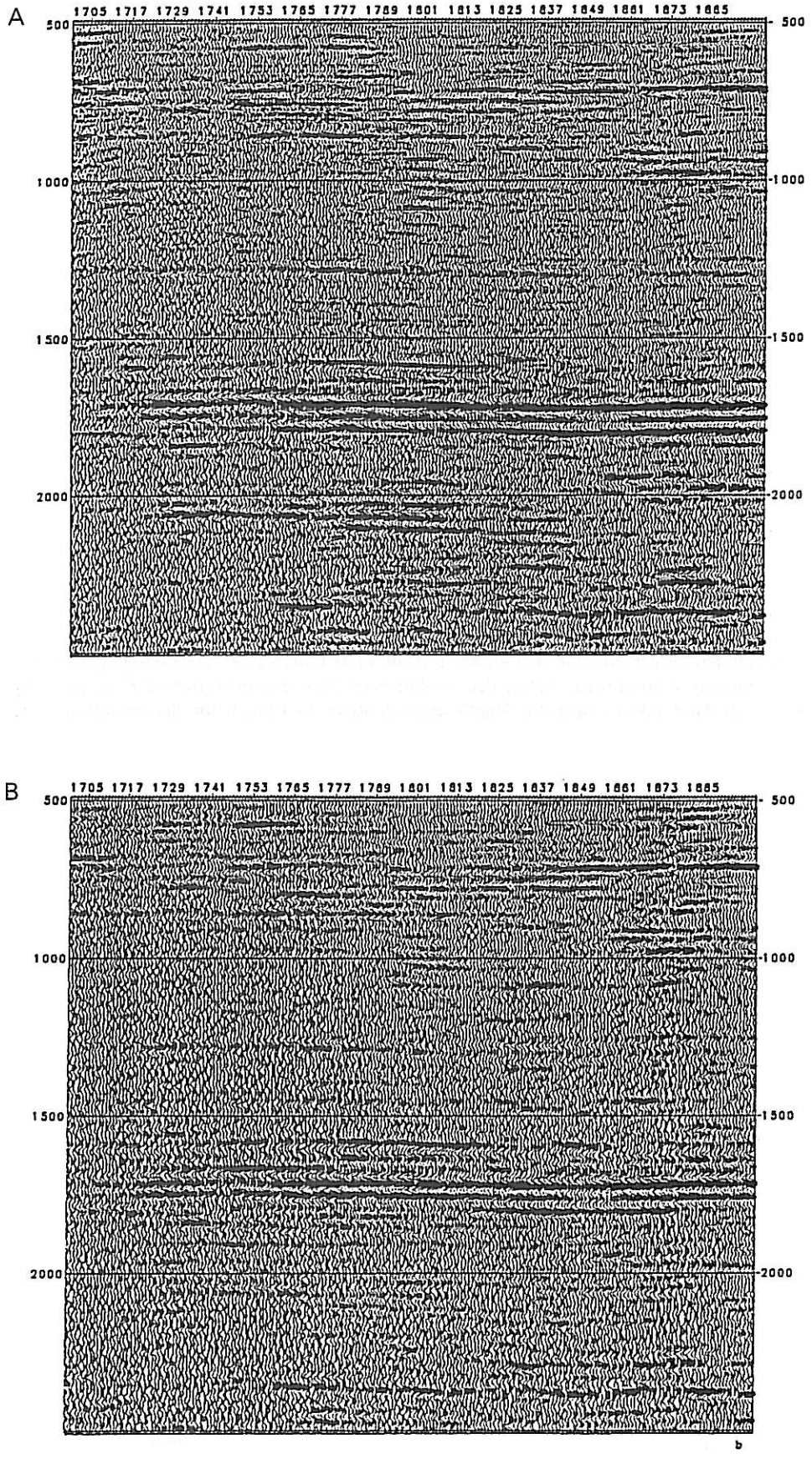


FIG. 4. Design gate of 2000 ms (500–2500). Seismic section V100, CMPs 1700–1900. (a) Before. (b) After post-stack deconvolution of 32 ms gap length and 600 ms operator length applied.

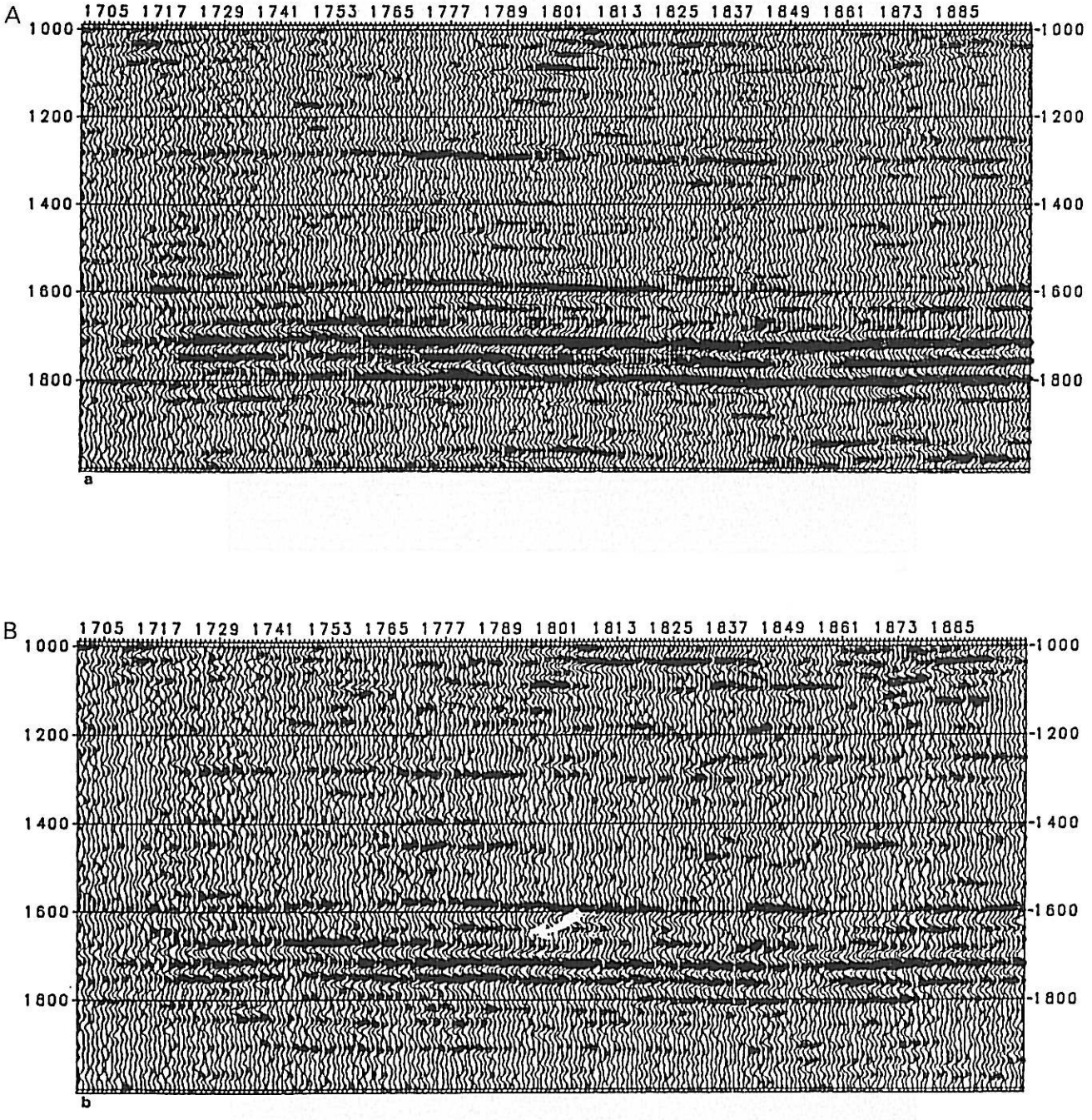


FIG. 5. Design gate of 1000 ms (1000–2000). Seismic section V100, CMPs 1700–1900. (a) Before. (b) After post-stack deconvolution of 32 ms gap length and 600 ms operator length applied.

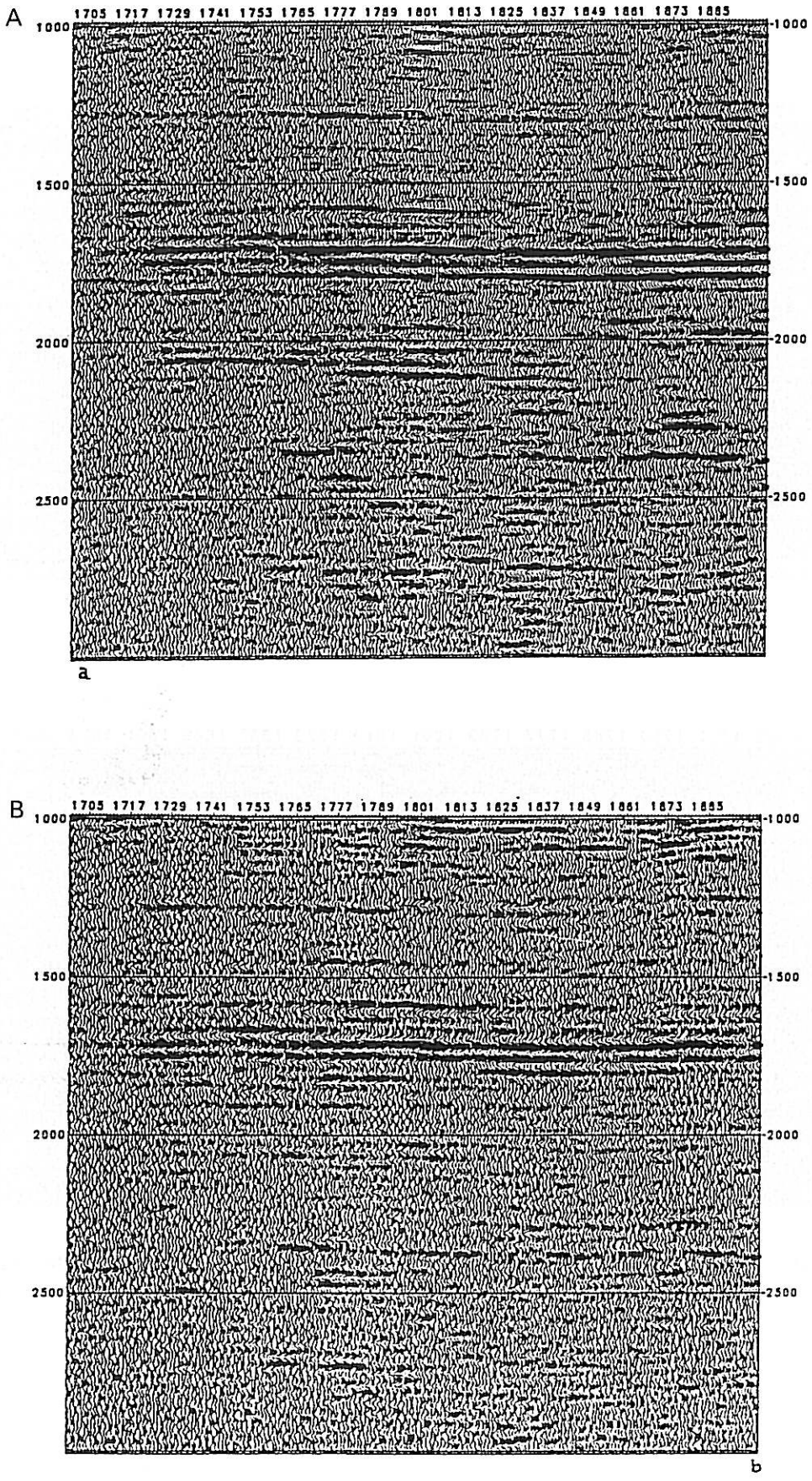


FIG. 6. Design gate of 2000 ms (1000–3000). Seismic section V100, CMPs 1700–1900. (a) Before. (b) After post-stack deconvolution of 32 ms gap length and 600 ms operator length applied.

b. Autocorrelation traces

The functions are generated from an average of 20 traces and are used for determining the filter's parameters. Fig. 3 is an example of an autocorrelation function produced from a design gate between 1000–3000 ms before and after deconvolution with 300 and 600 ms operator length. The multiple following the primary event at zero time crossing is showing very clearly and extends to 600 ms.

Fig. 3b shows the function before deconvolution where the ratio of amplitude of primary event to multiples is 42:13 and with time extent of 600 ms. Fig. 3c shows the function after 300 ms operator length is applied. The amplitude ratio of the primar events to multiples is 42:4 and with time extent of 300 ms. The operator has slightly reduced the ampitude of the multiples at time extent later than 300 ms with ratio of 42:8. Fig. 3d shows the function after 600 ms operator is applied. The ratio of amplitude of primary events to multiples is 42:4 and time extent of more than 600 ms which cover the time period of the main multiple reflections.

Figs. 1 and 2 show similar autocorrelation functions before and after deconvolution operators of 300 and 600 ms are applied. The extent of multiple duration is between 400 and 600 ms. Therefore, an operator of at least 600 ms is required in order to significantly remove a major part of the existing multiples. Both the sections and functions show considerable improvement regarding multiple attenuations after the operator is applied which indicates that the designed parameters are effective against multiples The testing of three windows is to avoid the selection of an improper gate which might result in computing and then applying parameters not suitable for the type of multiples that exist.

Figs. 7, and 8 show the same computed deconvolution parameters applied at different panels of traces in other parts of the seismic section. The panels were used to produce autocorrelation functions and to compare the functions with those used for deconvolution parameters computation and also for multiple duration estimation. The comparison is to investigate whether these parameters have the same or different effects on multiple attentuation. The functions produced after the deconvolution parameters were applied show similar effect to that shown on the functions used for producing and testing the parameters. This indicates that the designed parameters are effective and could be applied at different parts of the sections.

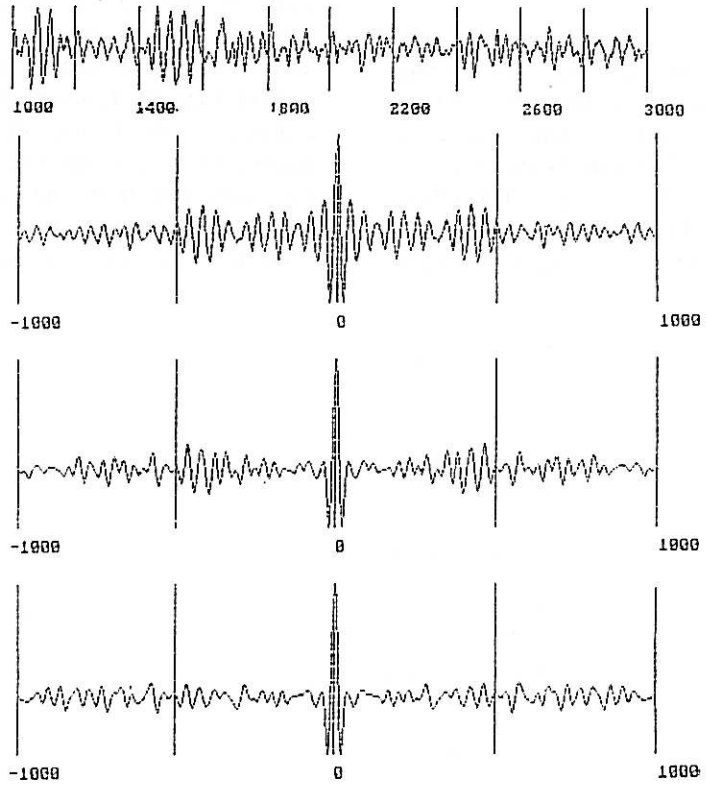


FIG. 7. Autocorrelation function generated from seismic section V100, CMPs 2220–2240, and time interval 1000–3000 ms. Similar effect is shown regarding multiple attenuation to those used for deconvolution parameters computation in other parts of the sections.

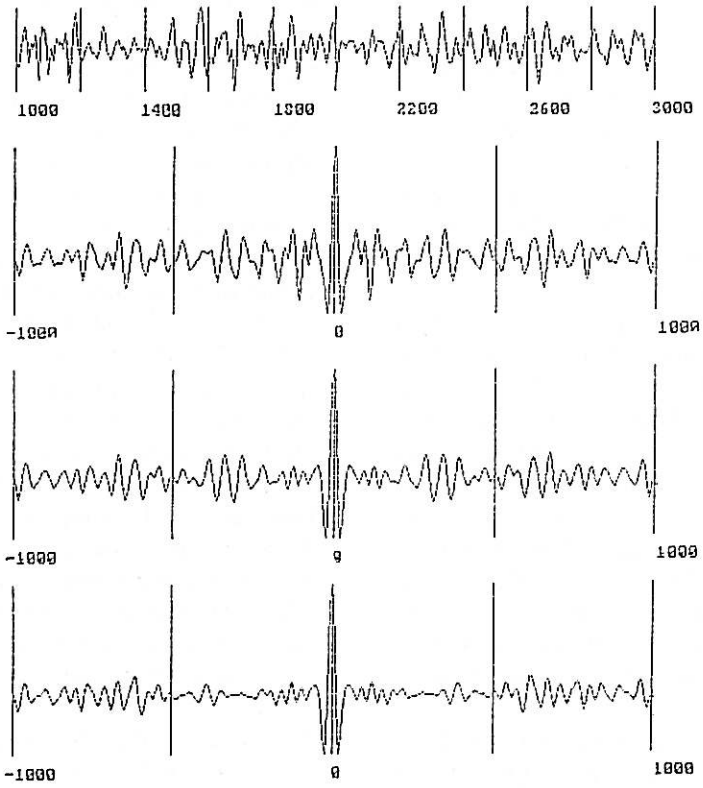


FIG. 8. Autocorrelation function generated from seismic section V109, CMPs 1240–1260, and time interval 1000–3000 ms. Similar effect is shown regarding multiple attenuation to those used for deconvolution parameters computation in other parts of the sections.

c. Prediction distance

The autocorrelation functions were used to compute deconvolution prediction distance. The zero crossing technique is used to measure prediction distance which is the time of zero amplitude point or crossing on the autocorrelation function. Prediction distance is specified as the second zero crossing (Peacock and Treitel, 1969) which actually will vary as the predominant frequency varies.

Fig. 9 shows the same input trace as Fig. 2a and an enlarged part of the autocorrelation function of Fig. 2b. It illustrates the computation procedures of prediction distance by applying the second zero crossing technique. Several functions were obtained from the same time intervals along the seismic sections and were used to compute the prediction distances at these parts of the sections.

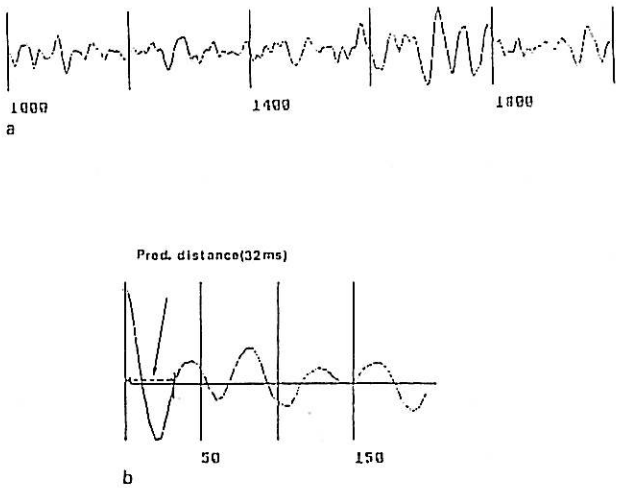


FIG. 9. (a) Input trace from seismic section V100, and design window 1000–2000 ms. (b) Autocorrelation of the input trace showing the computation of prediction distance by applying the second zero crossing technique. Also showing enlarged portion of the existing multiples. Refer to FIG. 2b for multiple time duration.

The functions showed that the prediction distances varied slightly from one part of the section to the other. Such variations could be as a result of lateral change in the characteristics of primary and multiple reflections which affected the frequency of the propagated seismic energy. The variation also could result from a change in frequency with depth which produces an increase in prediction distance as the low frequency become predominant with increasing depth.

d. Prediction operator length

The estimation of operator length for post-stack deconvolution was carried out by using the autocorrelation function for observing the energy of the primary event at zero time amplitude, and the amplitude and extent of multiples following the primary (Figs 1b, 2b and 3b). The testing of multiple attentuation was started by applying the same prediction distances computed from the functions while changing the operator lengths. The selection of the best operator length was started by using operators ranging between 140 and 750 ms and observing their effect on multiple attenuation. As it has been described previously and shown in Fig. 3b, the ratio of the amplitude of the primary to multiple reflections before deconvolution parameters were applied is 3.23:1 and the time extent of multiples is 600 ms. On the deconvolved trace (Fig. 3c–d) the ratio is 10.5:1. Figures 10, 11, and 12 show part of the seismic sections before and after a deconvolution filter of 32 ms gap length, and 300 and 600 ms operator length are applied. The sections are parts of seismic sections V100 and V109 and time interval between 1000–2000 ms. The sections obtained after deconvolution show progress in multiple attenuation as filter operator length increases. The reduction in multiple effect continued until the operator length reached 600 ms. When the 750 ms operator is applied no noticeable improvement is observed. Therefore, the extent of multiple duration is believed to be around 600 ms and the required operator should be not less than 600 ms to work effectively against the existing multiples.

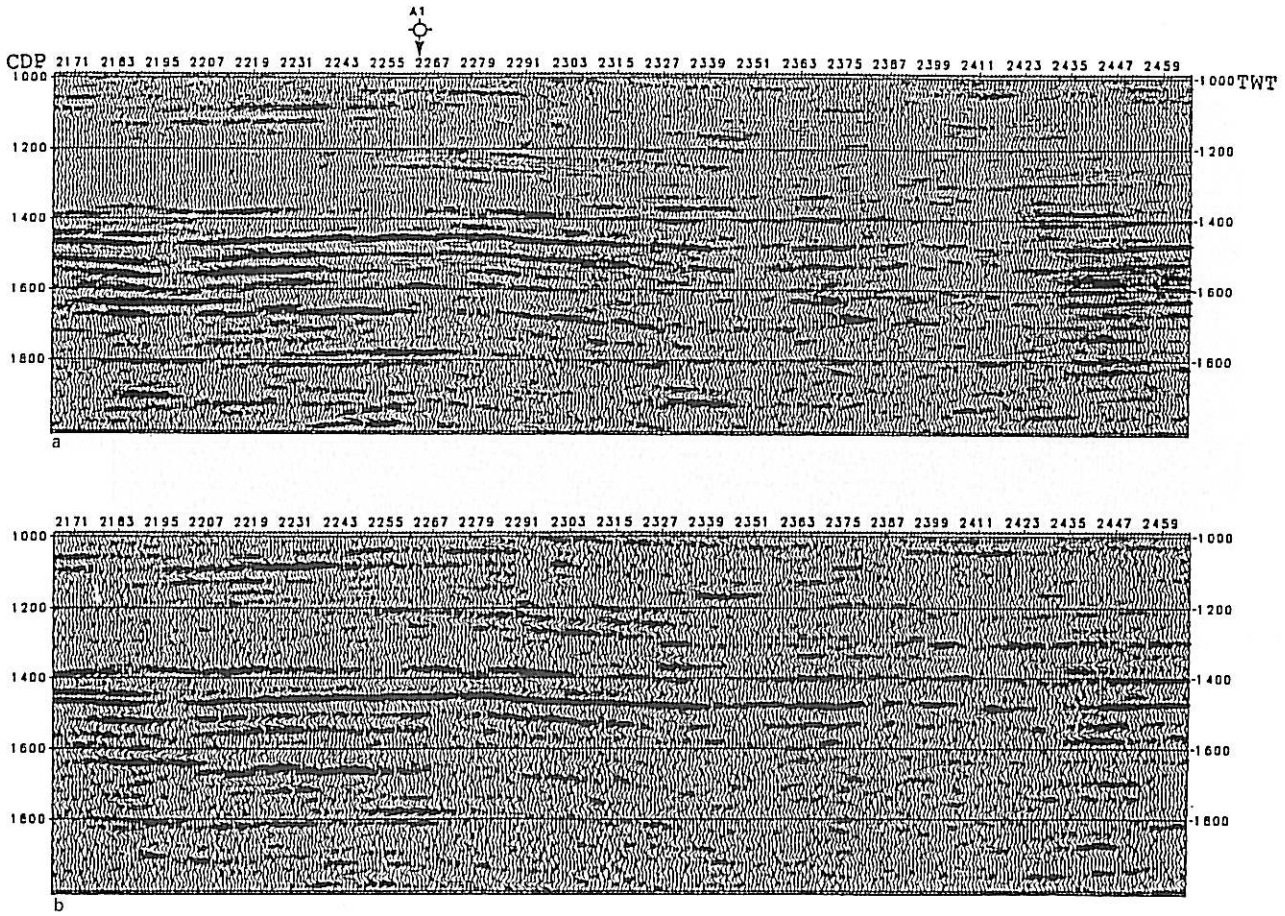


FIG. 10. Part of seismic section V100, CMPs 2166–2466. (a) Before post-stack deconvolution reflections are buried in multiple energy. (b) After post-stack decovolution of 32 ms gap length, 600 ms operator length is applied. It removed a significant amount of multiples and helped distinguish prominent reflections.

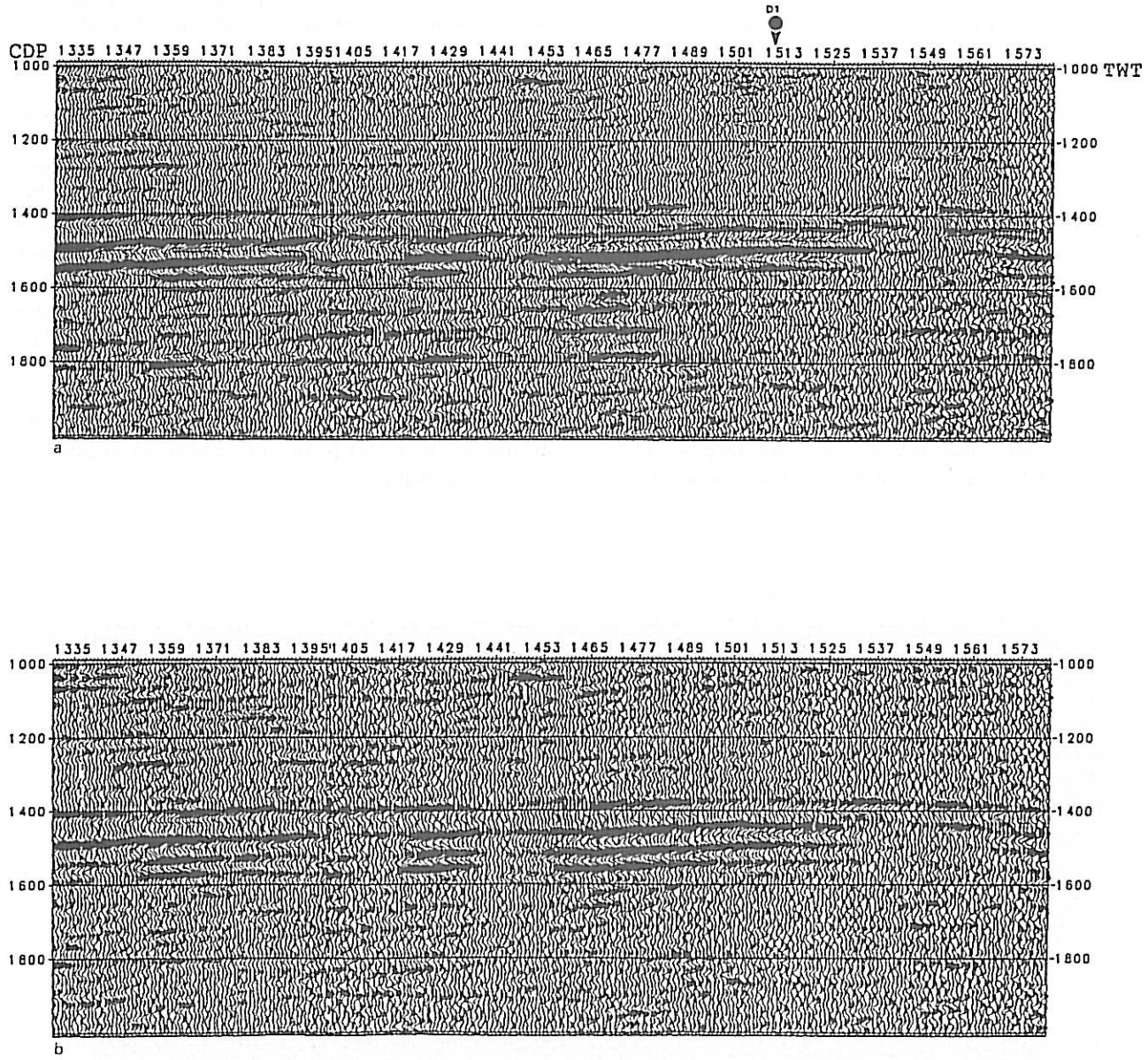
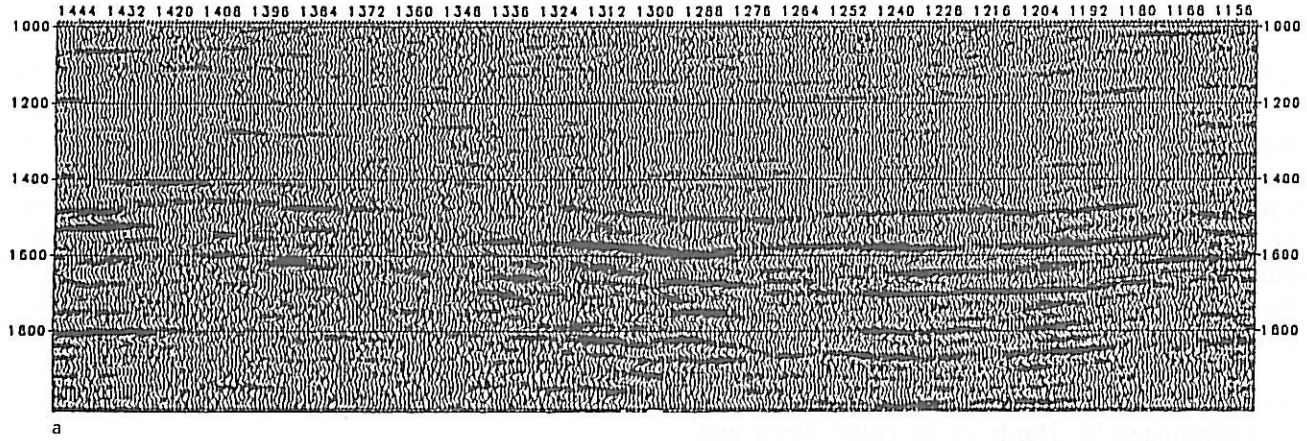
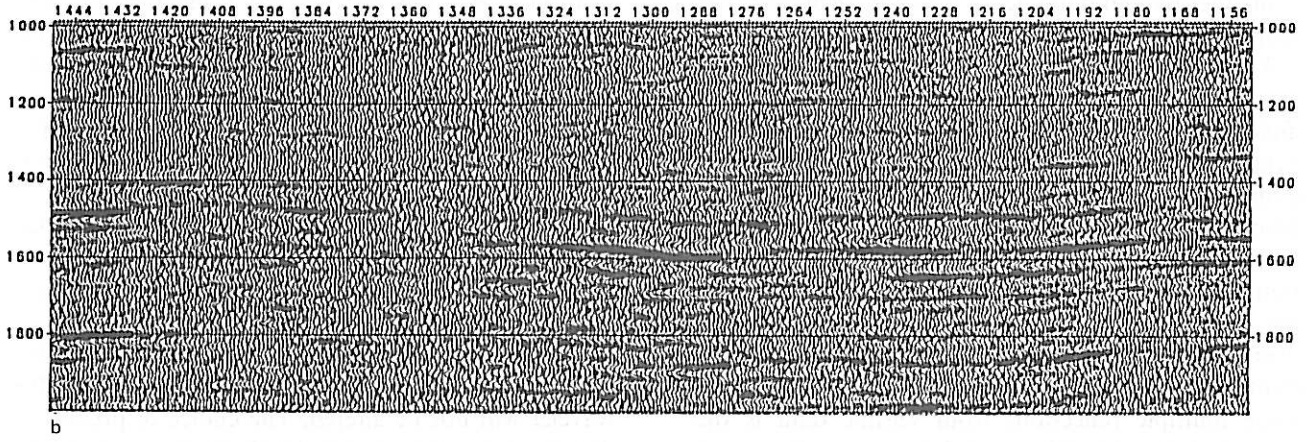


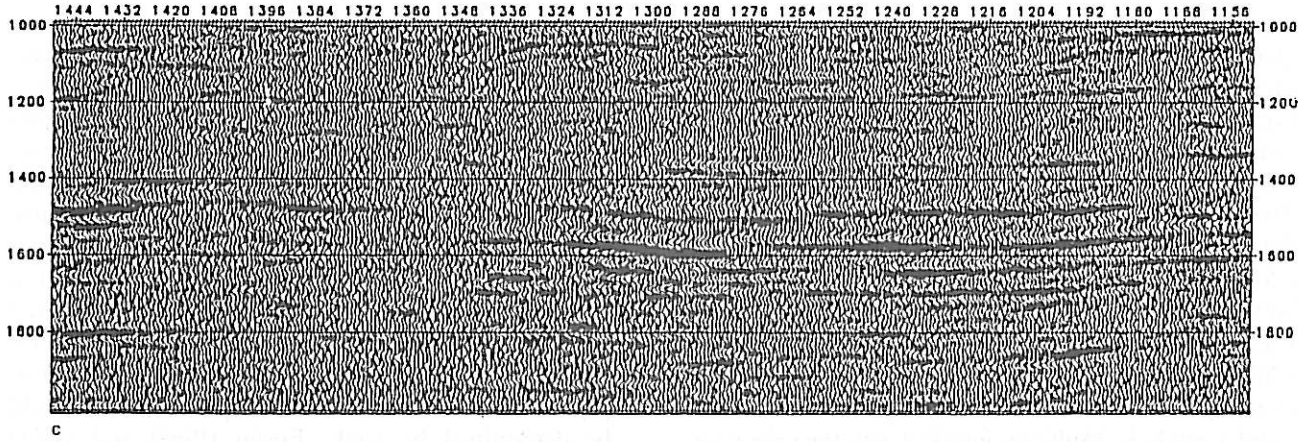
FIG. 11. Part of seismic section V100, CMPs 1330–1580. (a) Before. (b) After post-stack deconvolution applied. It has similar effect as in FIG. 10.



a



b



c

FIG. 12. Part of seismic section V109, CMPs 1151–1449. (a) Before deconvolution, multiple energy is strongly visible especially around and below 1800 time line. (b) After deconvolution of 32 ms gap length, 300 ms operator length applied. (c) After 600 ms operator length is applied. Multiples are suppressed and primary reflections became prominent.

DISCUSSION

a. Multiples

Multiples have been defined by Robinson (1979) as events that make one or more round-trip paths within the sedimentary layers before returning to the surface of the earth. Multiple attenuation techniques are conventionally classified according to the criteria by which they distinguish multiples from primary events. These criteria are the periodic nature of multiples and the move-out difference between multiples and primary reflectors. It has been mentioned by Hardy *et al.* (1989, 1990) and Hardy and Hobbs (1991) that no single technique consistently out-performs the others; performance depends on each and every data example. Yilmaz (1989) has pointed out that there are many assumptions in the predictive technique which are not generally met by real data; hence it is not surprising that multiples are not effectively suppressed.

The source and type of these multiples are not very clear and they could be the result of surface multiples or reverberation within sedimentary units. Multiples can be divided into two main categories: long-path and short-path multiples (Badley, 1985). Stacking and deconvolution are the two main processing steps applied for the removal and attenuation of multiples. It is important that multiples are recognized so that they are not interpreted as primary reflections. Applying the proper technique (Sinton *et al.*, 1978; Hardy *et al.*, 1989) to remove these multiple reflections from seismic data is the primary factor in order to reduce any ambiguity in interpretation. Multiple attenuation is considered to be an essential step towards the recognition, and increase in resolution, of the primary reflection events which represent the main reservoirs in the study area such as the basement reservoirs. Also, it is very important for the enhancement of data quality in order to carry out other processing steps such as attribute analyses and inverse modelling. Final stacked seismic data is used for the recognition and possible establishment of seismic criteria to categorize the primary reflection events of interest. The multiples are clearly visible especially below the basement reflector such as in Fig. 10 between CMPs 2166–2280 and 1400–1800 ms; and Fig. 11 between CMPs 1330–1525 and 1550–1800 ms; and Fig. 12 between CMPs 1449–1345 and below 1700 ms. They appear to have severely affected the primary events and obscured any detailed stratigraphic analysis. Multiples interfere with the primaries, hence, recognizing major reflections events and their extension along the seismic section becomes very difficut. The seismic sections obtained after the predictive deconvolution technique is applied show that weak remnant multiples still exist. These remnant multiples are probably the result of relatively high amplitude interlayer multiples which are not explicitly predicted by the deconvolution operator. Complete suppression of multiples is the desired result from the application of various multiple suppression techniques; however, multiples on a section exhibit a range of properties and so only those multiples which conform to the predicted assumptions made will be removed.

b. Choice of Prediction Distance

The prediction distance is chosen to be equal to the time of a specified zero amplitude point or crossing on the autocorrelation. It has been indicated by Peacock (1969) that the prediction distance equal to the second zero crossing (Fig. 9) is generally the best choice and it will obviously vary as the predominant frequency varies. Sinton *et al.* (1978), during their study of deep crustal reflections in the western Gulf of Mexico, have applied predictive deconvolution operators containing gap lengths with a duration of 4 to 5 sec. They have been used to suppress long delay multiple reflections which obscure primary reflections from within the earth's crust. The prediction distance of a predictive filter can be used to control the length of the reflection wavelet on output data. If the prediction distance is longer than the basic wavelet then the wavelet will not be altered. The choice of prediction distance for optimum wavelet shortening is normally a compromise between the shortest wavelet, for maximum resolution and the overall signal-to-noise ratio of the data (Peacock, 1969).

c. Choice of Operator Length

The choice of proper deconvolution operator length has been discussed by many workers such as Foster *et al.* (1968), Hatton *et al.* (1986), Yilmaz (1987) and White (1987). It has been mentioned by Hatton *et al.* (1986) that as a rule of thumb, the window length (design gate) is to be ten times the maximum autocorrelation lag (operator length). Another suggestion by Yilmaz (1987) for pre-stack deconvolution indicated that the window should be no less than eight times the operator length. Short windows embracing few reflections yield poor statistics. For post-stack deconvolution the parameters should be determined by trials. Foster (1968) and White (1987) have discussed the estimation problem in the deconvolution process. They have pointed out that

lengthening the deconvolution operator tends to compress the output wavelet more. The resulting improvement is represented by a decrease in distortion of output with increasing operator length. The autocorrelation functions obtained from different design gates (Figs 1, 2, and 3) show that the operator length is exceeding the suggested rule of thumb estimates. The main multiples extend to around 600 ms as shown in Fig. 3 which suggests that the filter should have the same length in a gate of only 2000 ms. The suggested rule of thumb percentage between the design gate and operator length fall far short of the required operator as indicated by the obtained autocorrelation functions. Figs. 1, 2 and 3 indicate that the extent of multiples is still clear even when the 300 ms operator was applied. In this set of data a time interval of 3000 ms a filter with operator length of 600 ms is shown to be the most effective operator for attenuating the existing multiples.

CONCLUSIONS AND RECOMMENDATIONS

The study shows that further investigation is required regarding the estimation and application of the deconvolution parameters in relation to multiple suppression during the seismic data processing. The sources of multiple generation seem to be more complicated than generally assumed, and the suppression of multiples effectively requires the availability of detailed information about the reflectors and their geometry. It seems that there is no practical and clear computational procedure in the literature about how the deconvolution parameters should be estimated and applied for pre-stack and post-stack deconvolution. The suggested rule of thumb techniques, which are mainly for pre-stack deconvolution to relate operator length to design gate, have not described the practical conditions in which such techniques should be applied. In this set of data a deconvolution filter with 32 ms prediction distance and operator length of 600 ms is shown to be the most effective operator for attenuating the existing multiples.

It is evident from this study that although the applied post-stack deconvolution on the observed seismic data gave encouraging results, they still have not shown the expected improvement regarding multiple suppression. Therefore, elaborate planning procedures prior to the acquisition of seismic reflection data might improve the quality of the seismic data. The planning includes the generation of modelled sections from the CDP gathers and well data. The company should ask the contractor to provide model of CDP gather with multiples included. This could aid in the assessment of the existing type of multiples. The multiple effects might be minimized by testing different patterns during the gathering of field data. The optimum recording and optimum offset could be designed to cancel the multiple at certain intervals by the choice of source-receiver offset which has a suitable angle for receiving the reflected seismic energy from primary reflectors and rejecting energy from the multiples.

ACKNOWLEDGEMENT

I would like to express my thanks to the management of the Petroleum Research Centre, special thanks go to Mr M. Idris the Secretary of People's Committee of the PRC for permission to publish this paper. I wish to thank Dr W. Ashcroft from the Geology and Petroleum Geology Department, University of Aberdeen for his help, guidance and valuable discussions in preparing this work. Thanks are also extended to the management and staff members of the Libyan National Oil Corporation and Zuetina Oil Compay for providing the data of the study area.

REFERENCES

Arya, V.K. and Agwal, J.K. (Eds.), 1982. Deconvolution of seismic data: Hutchinson Ross Publishing Company.

Badley, M.E., 1985, Practical seismic interpretation: IHRDC, Publisher.

Berkhout, J.A., 1977. Least-squares inverse filtering and wavelet deconvolution, Geophysics 42, 1369–1383.

Dobrin, M.B. and Savit, C.H., 1988. Introduction to geophysical prospecting (4th ed.). McGraw-Hill book Company, Singapore.

Foster, M.J., Sengbush, R.L. and Watson, R.J., 1968. Use of Monte Carlo techniques in optimum design of the deconvolution process, Geophysics 33, 945–95949.

Griffiths, L.J., Smolka, F.R. and Tremly, L.D., 1977. Adaptive deconvolution: a new technique for processing time-varying seismic data. Geophysics 42, 742–759.

Hardy, R.J.J. and Hobbs, R.W., 1991. A strategy for multiple suppression. First break 9, 139–144.

Hardy, R.J.J., Hobbs, R.W., Jones, I.F. and Warner, M.R., 1990. The reliability of multiple suppression. First Break 8, 297–304.

Hardy, R.J.J., Warner, M.R. and Hobbs, R.W., 1989. Labelling long-period multiple reflections. Geophysics 54, 122–126.

Hatton, L., Worthington, M.H. and Makin, J., 1986. Seismic data processing: Theory and practice, Blackwell, Scientific Publisher, London.

Peacock, K.L. and Treitel, S., 1969. Predictive deconvolution: theory and practice. Geophysics 34, 155–169.

Robinson, A.E. and Durrani, T.S., 1986. Geophysical signal processing. PHI publisher. p. 481.

Robinson, E.A., 1979. Predictive deconvolution. Development in geophysical exploration methods–2, A.A. Fitch, (Ed.). 1979, p. 77–106.

Robinson, E.A., 1967. Predictive decomposition of time series with application to seismic exploration. Geophysics 32, 418–484.

Siton, J.B., Ward, R.W. and Watkins, J.S., 1978. Suppression of long-delay multiple reflections by predictive deconvolution: Geophysics 43, 1352–1367.

Treitel, S. and Robinson, E.A., 1966. The design of high resoution fiters. Inst. Electr. Electron. Eng., GE-4: 25–38.

White, R.E., 1987. Estimation problem in seismic deconvolution, in: Deconvolution and inversion: M.H. Worthington (Ed.). Blackwell scientific publications p. 5–37.

Yilmaz, O., 1987. Seismic data processing. Investigations in geophysics, Vol. 2: S.M. Doherty (Ed.). Society of Exploration Geophysicist.

PRJ, Vol. 5 (January 1993); P. 37–45, 14 FIGS, 1 TABLE.

AMPLITUDE FEATURES OF FAST COMPRESSIONAL WAVES IN POROUS MEDIA ON ZERO-OFFSET SYNTHETIC SEISMOGRAMS

A.A.A. Othman*

مظاهر سعات الموجات التضاغطية السريعة في الأوساط المسامية على السيسموجرامات التخليقية صفرية الإزاحة

عادل علي علي عثمان

تتأثر سعة الموجات السيزمية بنوع الوسط التي تمر خلاله. لذلك صمم نموذج جيولوجي لدراسة التغير في سعات الموجات السيزمية داخل عدة صخور لها درجات مسامية مختلفة. تم إختيار أربعة أنواع من الصخور لتوضيح مظاهر اختلاف السعات وذلك باستخدام السيسموجرامات التخليقية.

ABSTRACT

The seismic amplitudes are clearly affected by the type of medium through which waves are propagated. A geologic model was designed to study the changes in amplitudes of the seismic waves within several rocks of different porosities. Four rocks are selected to show these features using synthetic seismograms.

INTRODUCTION

The amplitude of seismic waves decay by one of several processes like scattering, geometrical spreading, reflections, transmissions, dispersion or intrinsic dissipation. The intrinsic dissipation is present when the medium is anelastic. The present study considers the medium as elastic, homogeneous, and isotropic. Fluid-mineral chemical interactions and the microcracks were not studied.

Geophysicists, in the sixties, became interested in using the amplitude of the reflected events as a direct method to the presence of hydrocarbons (Domenico, 1974). Until 1970, only the variations in the amplitude of the reflected signal were used as a qualitative tool for identifying seismic events. A quantitative analysis of the character of reflected signal might lead to more information of some of the acoustical properties of the rock formations (Sheriff, 1974).

The velocity of seismic waves that travel through porous media depends not only on the rock matrix velocity, but also on the porosity and the characteristics of the interstitial fluids. Amplitudes of reflected seismic waves are important evidence of the anomalous effect of interstitial fluids (water and/or hydrocarbons). This depends on the reflection coefficients of the interfaces, separating different lithologies in a sequence. The polarity of the reflected seismic pulse can help to identify a saturated reservoir interface (Sheriff, 1974). Phase reversal occurs if the reflectivity changes sign.

Bright spots became the hottest topic in exploration, and with good reason, because they were effective in pointing gas reservoirs in the Gulf of Mexico and other areas with similar geologic characteristics. Observations of time sections, led to false synclinical structures corresponding to reflections from below the gas horizons (Hammond, 1975). Some characteristics of the time signal is expected to show certain typical changes over the region containing gas, oil or other fluids.

Quantitative estimations are presented here to discuss some of the above mentioned parameters, taking in consideration that the computations are carried out for the zero-offset case.

*University of Qatar, Geology Dept, P.O. Box 2713, Doha, Qatar

THEORY

Exploration geophysicists are interested in the lithology, porosity, permeability, saturation and type of pore fluid of the subsurface formations. Therefore, there are many authors, who tried to relate the propagated wave velocity to rock parameters. The time average equation (Wyllie et al., 1962) empirically relates velocity and formation parameters for wide range of porosity as:

$$v=\{(\phi/v_f)+(1-\phi)/v_m\}^{-1} \quad (1)$$

where ϕ is porosity, v is liquid saturated rock velocity, v_f is pore fluid velocity, v_m is matrix velocity (massive rock).

The time average equation (1) displays the relationship between velocity and porosity which, according to Gardner and Harris, 1968, can be used for shallow porous layers. This equation cannot be applied for gas-saturated materials. Therefore, a modification for the equation is needed. In case of gas-saturated reservoirs, the modified Wyllie equation (Wyllie et al, 1962), would take the following new form (Marschall, 1984):

$$v=\{(\phi s_w/v_w)+[\phi(1-s_w)/(v_g \log(c_g/c_m))] +(1-\phi)/v_m\}^{-1} \quad (2)$$

here v is the wave velocity in a gas and fluid saturated porous medium, v_w is the wave velocity in water, v_g is the wave velocity in gas. S_w is the water saturation fraction, c_g is gas compressibility, c_m is matrix compressibility. The compressibility ratio of the fluids (gas) with respect to solids is nearly equal to 10 (Marschall, 1984) and in equation (2), the logarithm of this ratio will equal one.

Synthetic seismograms $S(t)$ can be computed from the convolution of the source wavelet $W(t)$ with reflectivity $R(t)$. It may be expressed as:

$$S(t)=R(t)*W(t) \quad (3)$$

The asterisk denotes convolution. The reflection coefficient R is computed from the equation:

$$R=(\rho_{i+1}v_{i+1}-\rho_i v_i)/(\rho_{i+1}v_{i+1}+\rho_i v_i) \quad (4)$$

where i denotes the i-th layer and

$$\rho=\rho_f+(1-\phi)\rho_m \quad (5)$$

where ρ is density, ρ_f is fluid density, ρ_m is matrix density.

Using the modified equation (2), a great number of synthetic traces may be computed, for each of which the suitable reservoir parameters have been modified. This set of traces may be used as a guide line for subsequent interpretation of the actual seismic data, after having applied the appropriate frequency-band limitation in form of the input source wavelet.

THE GEOLOGICAL MODEL

The geological model that has been chosen for investigation is shown in Fig. 1. It consists of three layers (A, B and C). Layers A and C are non-porous shale. Layer B is selected to be either dolomite, limestone or sandstone. The acoustical parameters of the model (slow p-wave and s-wave are neglected) are given in Table 1.

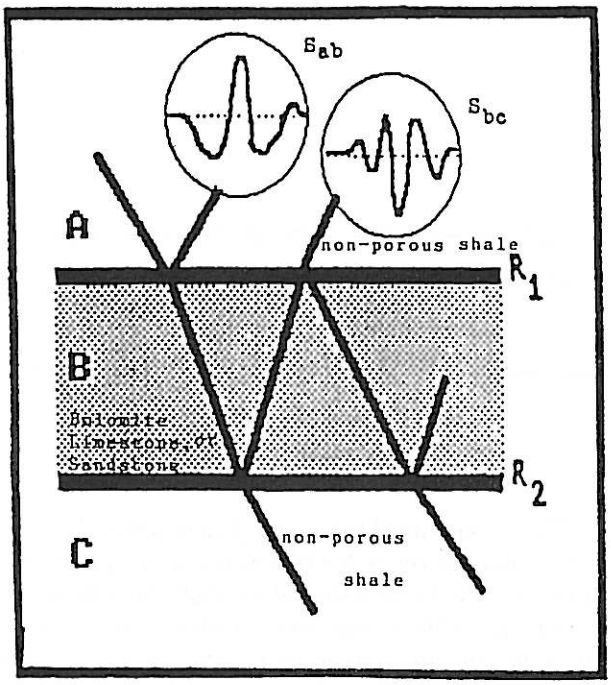


FIG. 1. A three geologic layers model A, B and C with reflection coefficients R_1 and R_2. S_{ab} and S_{bc} denote two reflected signals from the upper and lower interfaces of layer B.

Table 1. Numerical Parameters Used in the Studied Model

	Velocity (m/s)	Density (g/cc)	Porosity (%)
Layer A:			
Shale	4500	2.60	0
Layer B:			
Dolomite	7000	2.87	5 to 15
Limestone	6400	2.69	10 to 20
Sandstone	5500	2.65	15 to 35
Shale	4500	2.60	40 to 50
Layer C:			
Shale	4500	2.60	0
Fluids:			
Water	1500	1.00	—
Oil	1200	0.85	—
Gas	480	0.15	—

DESCRIPTION OF MODEL OUTPUTS

A simple calculation using the modified equation (2) was carried out to relate velocity with porosity over the given ranges in the studied geologic model (see Table 1). Fig. 2 shows the plots of all four rocks: shale, sandstone, limestone and dolomite at gas-, oil- or water-saturated cases. The wave velocity in dolomite highly decreases with increasing porosity and in gas-saturated case is lower than that in water-saturated one. This relation, for the indicated range, is almost linear in limestone, and the velocity of gaseous case is still lower than that of oil and of water saturated cases. A weak sensitivity appears in saturated sandstones. In shale, velocity is almost non-sensitive to porosity.

A computer program to execute the synthetic seismograms by inserting the porosity and follow its effects on amplitudes was generated by the author. A test was made in Fig. 3 to show the presence of porosity effects, if layer B was a shale flanked by the shale on the top as well as at the bottom. There are no reflection coefficients in the case of massive shale in layer B; i.e. the porosity is zero. According to the introduction of the porosity into layer B, a difference in velocity occured. A series of plots were computed for the dolomite, limestone and sandstone; in both gas- and oil-saturated cases. Every plot consists of three parts; each one contains many synthetic traces calculated over a given range of porosity for every rock type. In each part, a synthetic trace was calculated for a massive (non-porous) rock to consider it in the comparative studies when porosity is introduced into calculations.

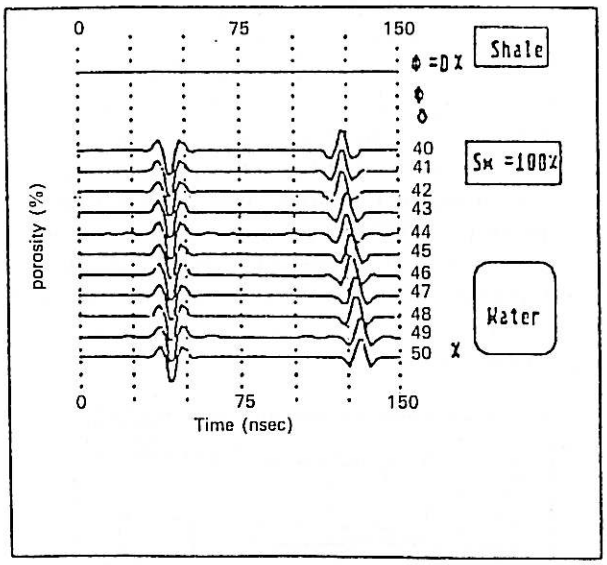


FIG. 3. Calculated synthetic seismograms in case of layer B is water saturated shale, for different porosity values.

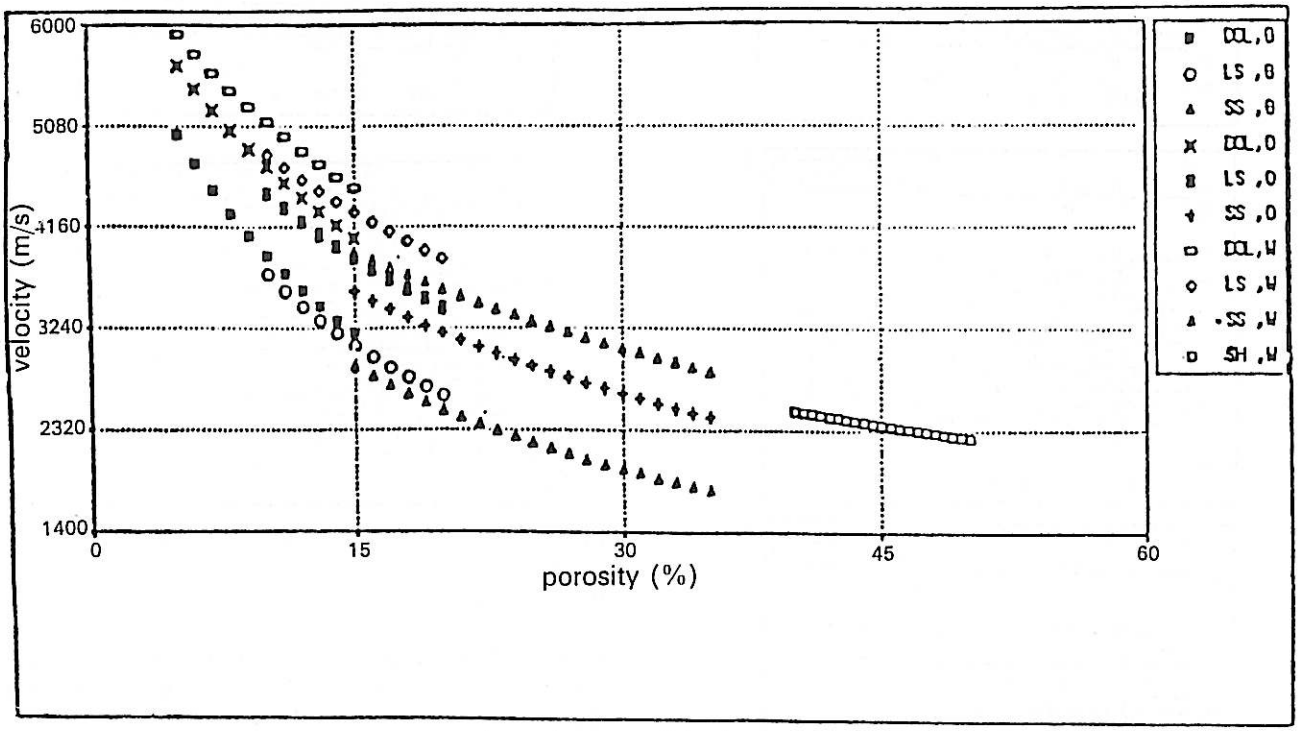


FIG. 2. Seismic velocity as function of porosity for limestone, dolomite, sandstone and shale in the studied model, in (G) gas-, (O) oil-, and (W) water-saturated medium.

SYNTHETIC SEISMOGRAMS IN GAS AND OIL SATURATED CASES

1. Dolomite

In a gas-saturated dolomite, the reflected event comes from the bottom of layer B (dolomite), with a

delay time compared with the massive case, which increases with increasing porosity. These time shifts are larger at higher porosity. Fig. 4A shows, also, a reverse of amplitude polarity starting at a porosity equal to 8%. At the mixed case (gas/water), this polarity reversal took place at a porosity value of 10%, as shown in Fig. 4B. Polarity reversals appear at a porosity of 15% in a water-saturated dolomite, as shown in Fig. 4C. Time shifts of the second event (the reflected from the bottom of layer B) generally decrease by increasing the water saturation percentage in the rock.

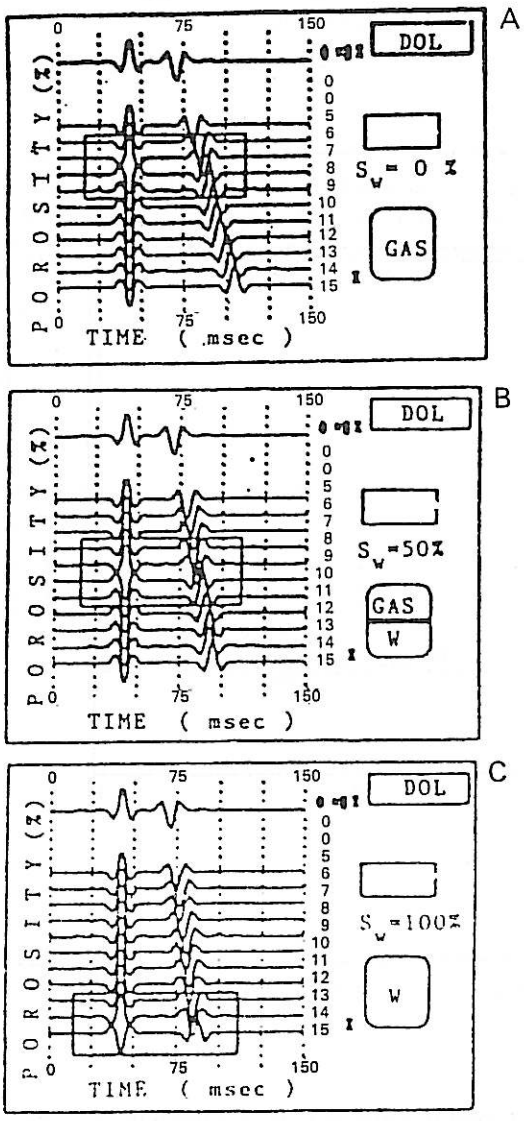


FIG. 4. Synthetic seismograms for partially gas-saturated dolomite, at different water saturations, calculated for layer B in the studied model.

Fig. 5A shows a case of oil saturated dolomite, in which the polarity reversals occur at a porosity equal to 12%. These reversals start at a porosity equal to 14% in the mixed (oil/water) case, see Fig. 5B. Polarity reversals at water-saturated case is

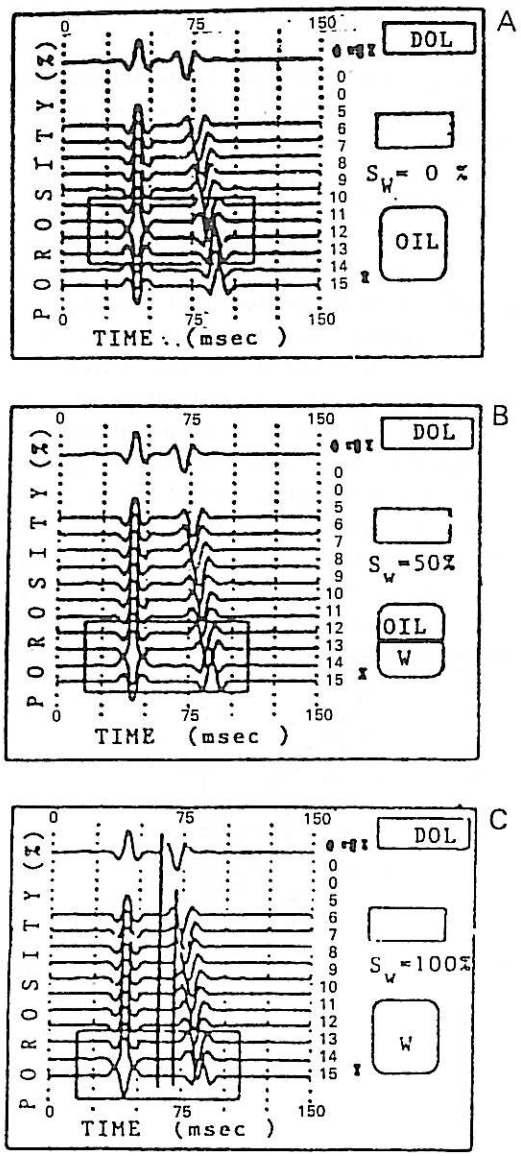


FIG. 5. Synthetic seismograms for partially oil saturated dolomite, at different water saturations, calculated for layer B in the studied model.

mentioned above and is shown in Fig. 5C. The delay shift is, in general, smaller than that in gas-saturated dolomite.

2. Limestone

Amplitude polarity changes sign with respect to a massive limestone, as seen in Fig. 6. Gas-saturated rocks give large transient times for the second event with increasing porosity fractions, see Fig. 6A. These time shifts are smaller in the gas-water mixture case as shown in Fig. 6B. Water-saturated limestone displays a case of polarity reversals starting at lower values of the proposed porosity range as shown in Fig. 6C.

For oil saturated limestones, time delays are the only difference with respect to the gas saturated case.

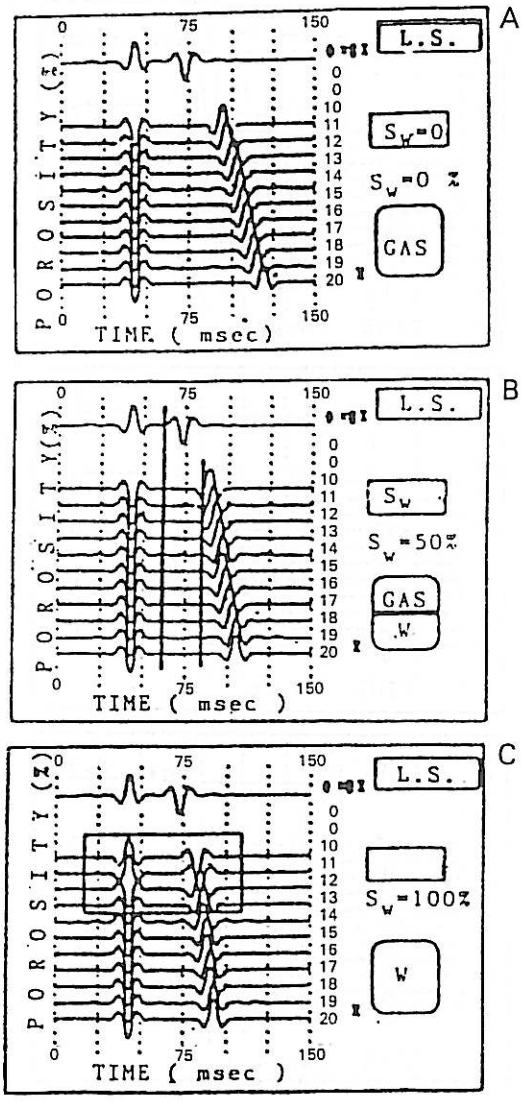


FIG. 6. Synthetic seismograms for partially gas-saturated limestone, at different water saturations, calculated for layer B in the studied model.

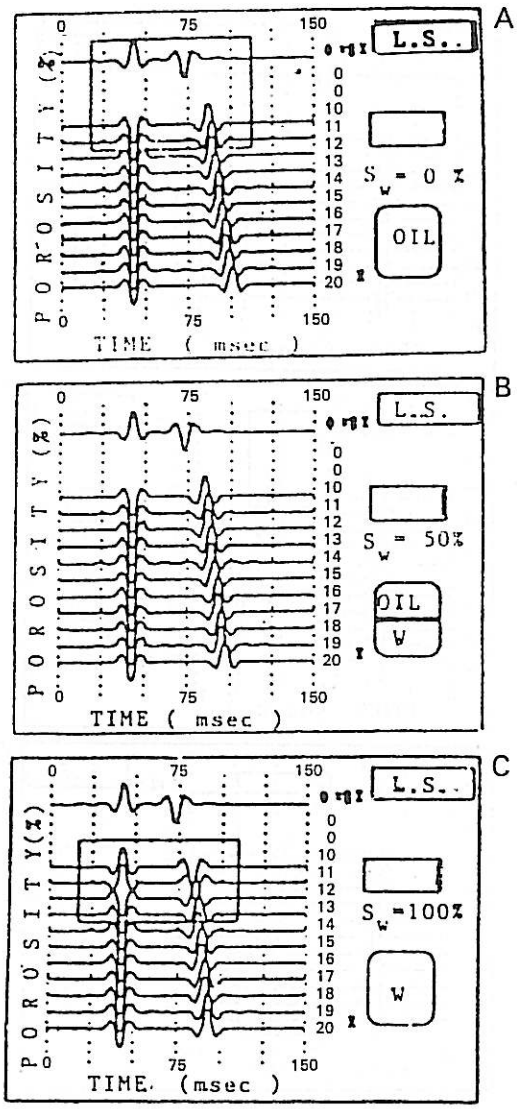


FIG. 7. Synthetic seismograms for partially oil-saturated limestone, at different water saturations, calculated for layer B in the studied model.

These delays are smaller than in gas saturation, as indicated in Fig. 7A. Introduction of water in the model decreases the time shift as shown in Fig. 7B. This is clearly shown in the case of water saturated limestone as seen in Fig. 7C. Reverse of amplitude polarity appears at porosity equal to 12%.

3. Sandstone

A porous sandstone is highly affected by the presence of pore fluids. Some features are observed in Fig. 8A, for the gas-saturated case. Time shifts increased at higher porosity fractions, but once the water is introduced, these time shifts decreased, as shown in Fig. 8B and Fig. 8C.

For oil-saturated sandstone rocks polarity reversals are present all over the porosity range as well as gas saturated case. The observable difference is a decrease of time shifts referring to massive sandstones with respect to gas-saturated one, as displayed in Fig. 9a.

Fig. 9B and Fig. 9C exhibit decrease in time shifts when the percentage of water saturation is increased.

AMPLITUDE CHARACTERISTICS DUE TO LAYER B

The following discussion is restricted to study the forms of the events reflected from the bottom of layer B.

Amplitudes in a porous dolomite have different features over the selected porosity range, at different degrees of water saturation. Fig. 10 shows the effects of three different cases of saturations on the amplitude. A quick comparison between the three cases confirm that in gas-saturated dolomite, the amplitudes are higher (bright spots). The calculated

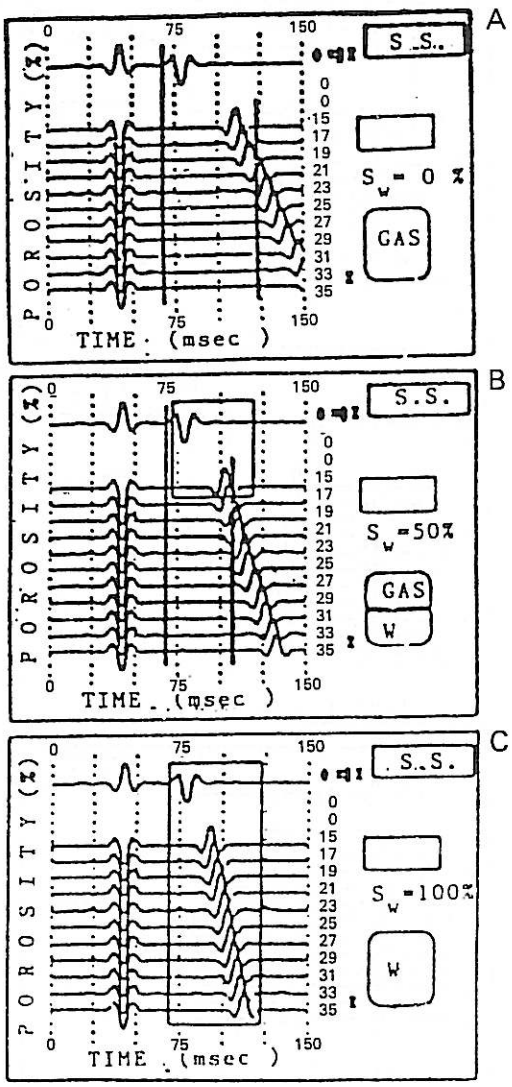


FIG. 8. Synthetic seismograms for partially gas-saturated sandstone, at different water saturations, calculated for layer B in the studied model.

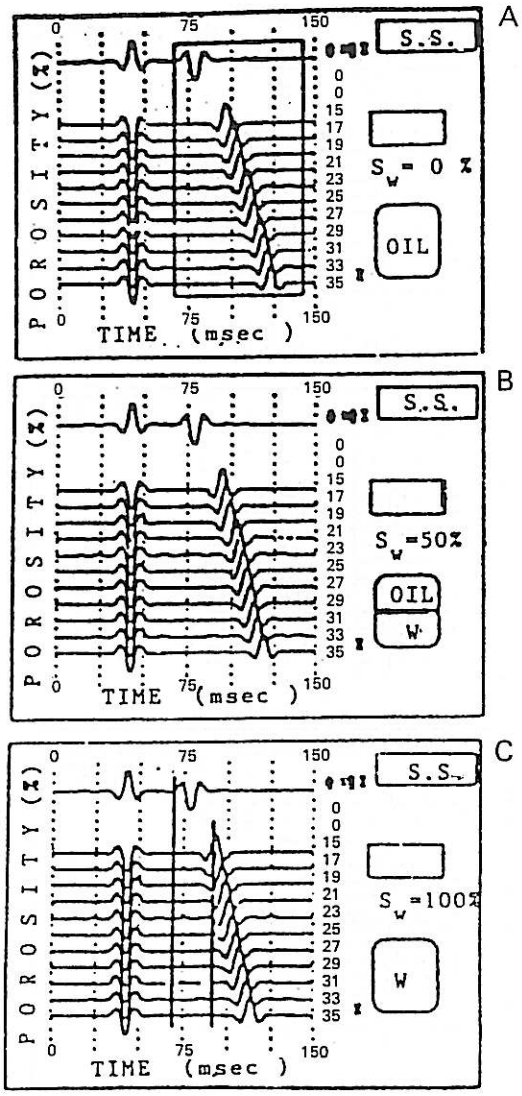


FIG. 9. Synthetic seismograms for partially oil-saturated sandstone, at different water saturations, calculated for layer B in the studied model.

amplitudes show an increase with increasing the porosity values. The presence of water in the formation decreases the amplitudes of seismic events, and moves the upper curve downwards. Before and after intersecting the zero-marked line (solid line), the amplitudes show changes from negative to positive values; i.e. polarity reversals. These reversals start at porosity higher than 6% (for $S_w=0\%$), and higher than 8.25% (for $S_w=50\%$).

Oil-saturation decreases the amplitude lower than that of gas saturated rock. Polarity of amplitudes changes signs at porosity higher than 11.75%. Due to presence of water, the last value will be shifted to porosity higher than 13.25%. If layer B is water saturated dolomite, amplitudes of travelling events increase with increasing porosity. A reverse polarity appears at porosity higher than 12.5%. The amplitudes of the water saturated case are generally larger than that of oil mixded with water. At porosity equals to 8.25%, seismic waves were reflected with the same amplitude, in both oil- and water- saturated cases, as observed in Fig. 10.

This situation is different in porous limestone as observed in Fig. 11. Acoustic waves that travel through a gas-saturated limestone have larger amplitudes which have change polarity upon reflecting at the bottom of layer B. The only exception is for $S_w=100\%$ for porosity values less than about 10.5%. Gas amplitude decreases downwards as water saturation is increased to 50%, (Fig. 11). A similar condition was observed in the case of oil-saturated rock, where the amplitudes were decreased by increasing S_w.

Amplitudes of travelling waves through gas saturated sandstone have a non linear relation with porosity, as shown in Fig. 12. The increase is steady for porosities less than 25%, and takes a linear shape for higher porosities. If the water saturation

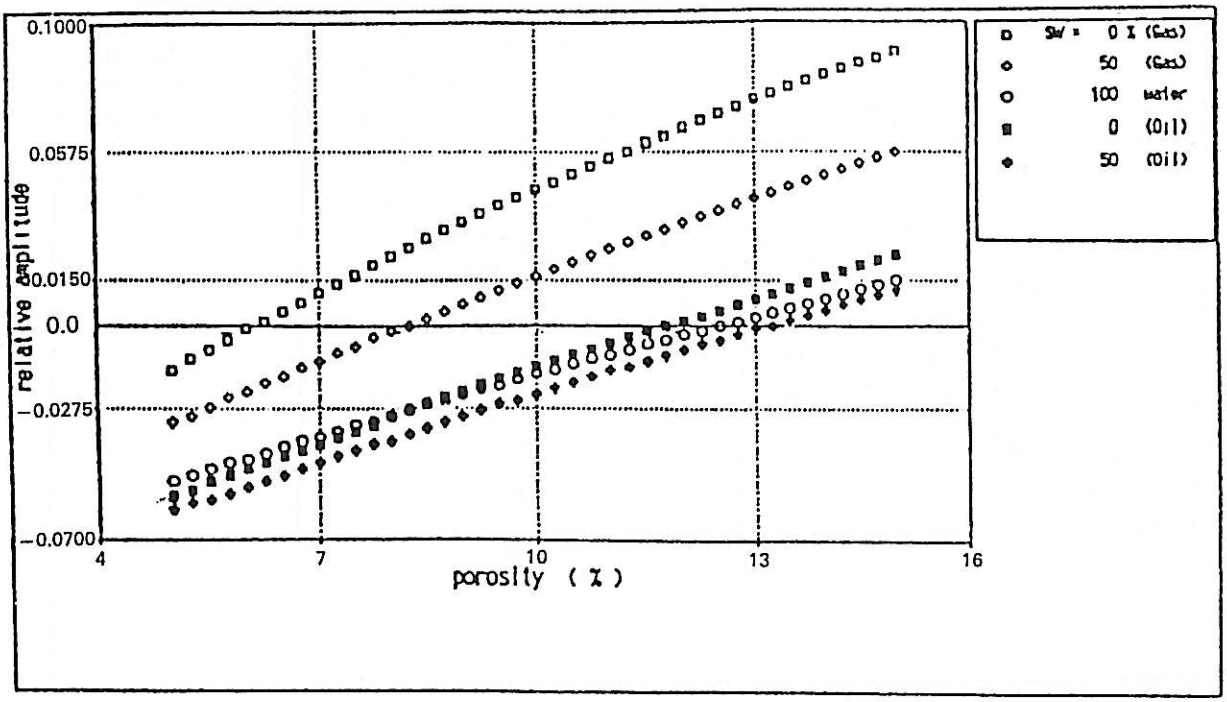


FIG. 10. Seismic amplitude and porosity for S_w=0%, 50% and 100% in both gas- and oil-filling porous dolomite.

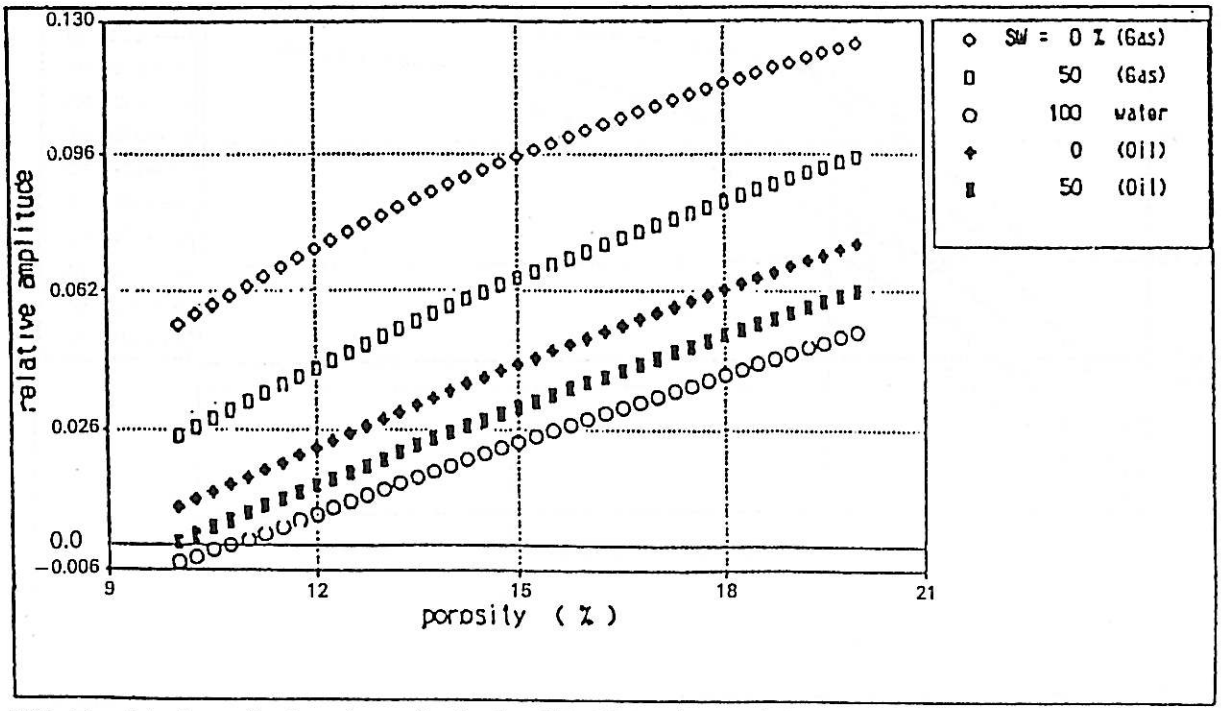


FIG. 11. Seismic amplitude and porosity for S_w=0%, 50% and 100% in both gas- and oil-filling porous limestone.

increases, it decreases the gas amplitudes. Oil saturated amplitudes decrease with increasing water content in the pores, as shown in Fig. 12. Water-saturated sandstones show amplitudes of minimum values and of linear nature with increasing porosity. There are no polarity reversals detected as seen in Fig. 12.

A complete picture was created in Fig. 13. Amplitudes of the waves passing through all the four rocks are displayed together. Polarity reversals take place at porosities starting from 7.5% to 15%. Sandstones have higher gas-saturated amplitudes than other studied rocks in the present work. Shales have also large amplitudes at higher porosities.

FIELD DATA

Three measured field records were collected from different published works to declare the above discussed ideas. These examples include bright spot

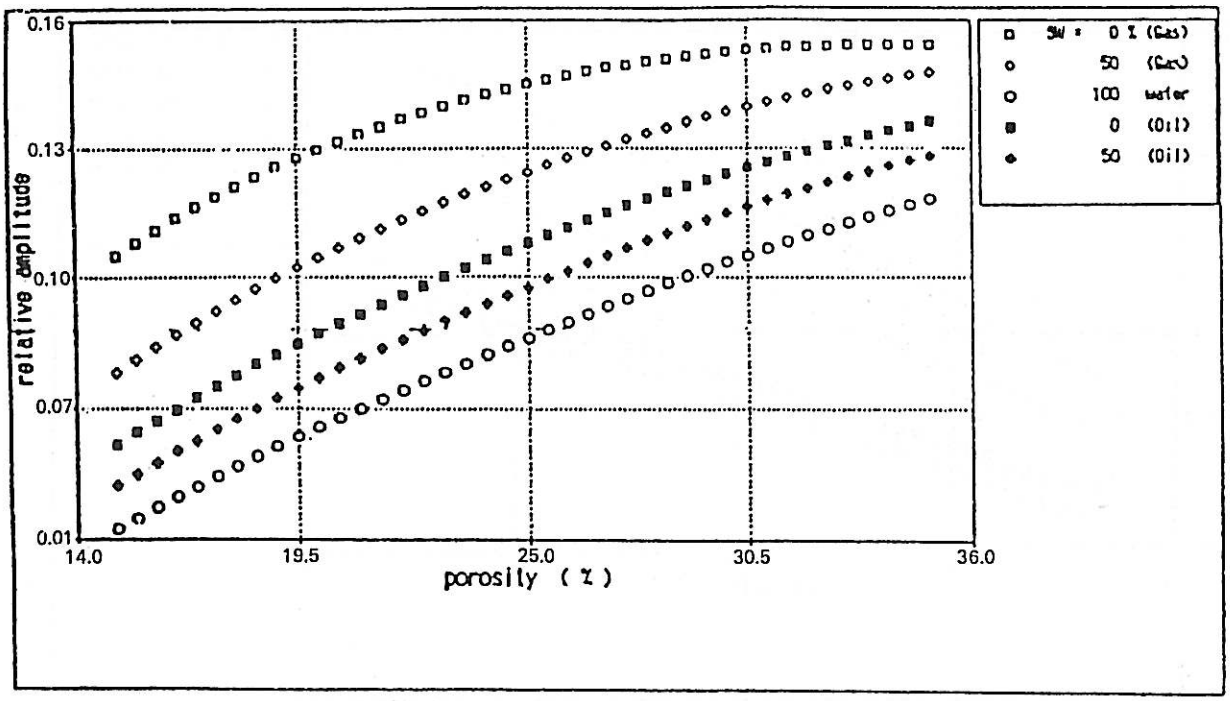


FIG. 12. Seismic amplitude and porosity for S_w=0%, 50% and 100% in both gas- and oil- filling porous sandstone.

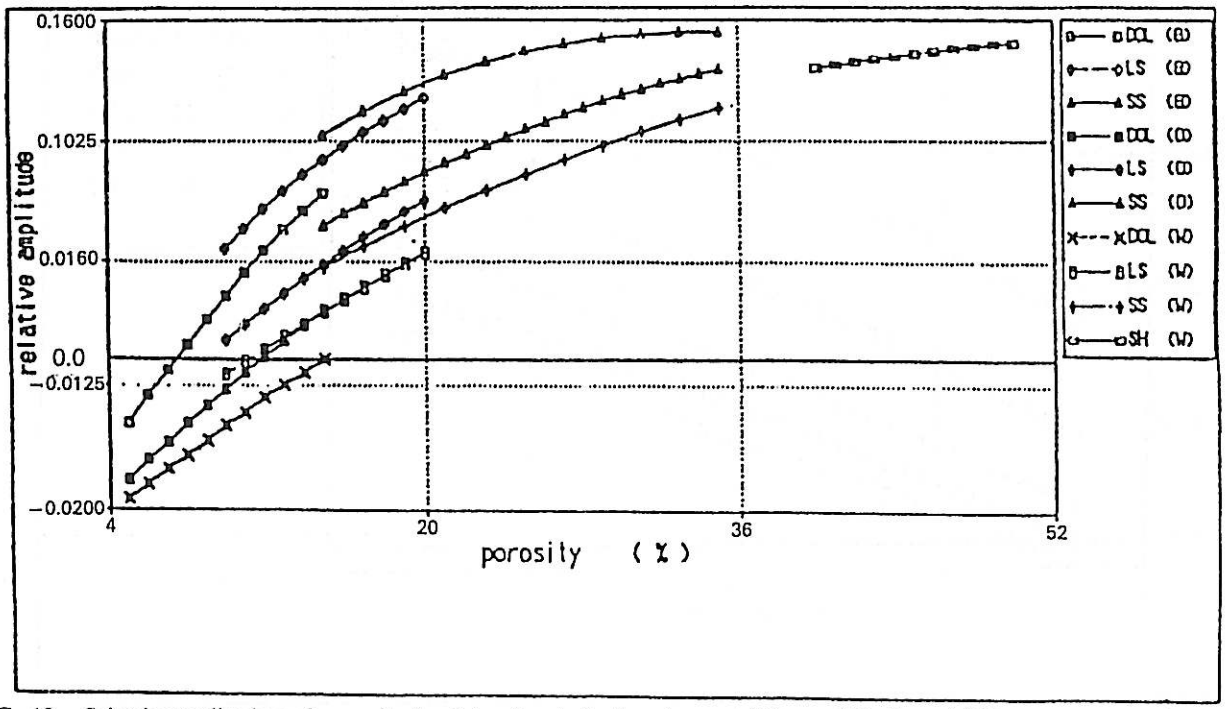


FIG. 13. Seismic amplitude and porosity for dolomite, shale, limestone; at (G) gas- (O) oil- and (W) water- saturated cases of the received second event in the studied model.

amplitudes, which help in the detection of gas reservoirs. Fig. 14A and Fig. 14B show gas fields. Amplitudes are higher than the adjacent horizons, which describe clearly the bright spots, giving to a similar amplitude characteristic like that calculated in the studied model. In Fig. 14B, a drilled well is indicated on the seismic line. Well information is tied with the presented time section, and the black markers are sandstones. Gas saturated sandstone, as mentioned in the previous section, gives higher amplitudes (bright spots).

In Fig. 14C, the two boxes display the polarity reversals which may be interpreted as structural changes (i.e., fault) or as a difference in the pore fluid contents, as observed from the calculated results of the studied model.

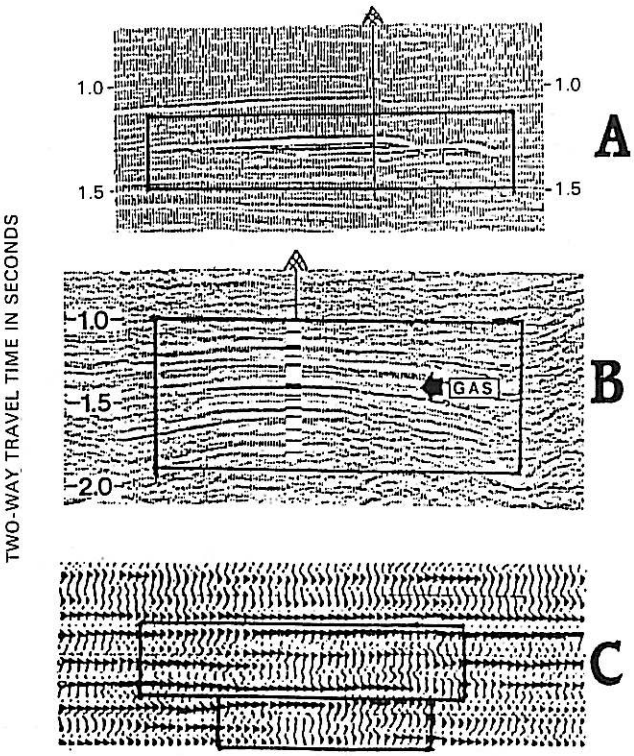


FIG. 14. Field seismic time sections describe the bright spots and polarity reversals signals.

CONCLUSION

The present study deals with travelled amplitudes in porous media. It is carried out through calculations of a designed model. The following conclusions can be considered:

1. Amplitudes of travelled waves in porous media are highly affected by porosity, the type of fluid (gas, oil, water) and the amount of fluid (porosity, saturation). Addition of water in the pores decreases these amplitudes.

2. In dolomite and limestone polarity reversals appear if the varying porosity crosses a specific value.

REFERENCES

Domenico, S.N., 1974, Effect of Water Saturation on Seismic Reflectivity of Sand Reservoirs Encased in Shale, Geophysics, vol. 39, pp. v 759–769.

Gardner, G.H.F., and M.H. Harris, 1968, Velocity and Attenuation of Elastic Waves in Sands, 9th Ann. Logging Symposium, Trans, (SPWLA), pp. M1-M19.

Hammond, A.L., 1975, Bright Spots: Better Seismological Indicators of Gas and Oil, Oil Commentary, vol. 12, pp. 2.

Marschall, R. 1984, Some Aspects of Deconvolution, Preprint, CDC's Petroleum Seminar, Geneva, Switzerland.

Sheriff, R., 1974, Seismic Detection of Hydrocarbons; the Underlying Physical Principles, Preprint, VI Annual Offshore Technology Conference, Houston, Texas.

Wyllie, R.J., Gardner and A.R. Gregory, 1962, Studies of Elastic Wave Attenuation in Porous Media, Geophysics, vol. 27, pp. 569–589; and discussion (1963): Geophysics, vol. 28, pp. 1074.

PRJ, Vol. 5 (January 1993); P. 46–55, 7 FIGS.

DEPOSITIONAL ENVIRONMENT OF THE BAHI FORMATION DEDUCED BY TEXTURAL ANALYSIS, NW SIRT BASIN, LIBYA

A.M.A. Sghair*

إستقراء بيئة ترسيب تكوين الباهي بحوض سرت الترسيبي من خلال نسيج الصخور الرسوبي

عبد السلام محمد الصغير

أجريت دراسة تفصيلية للجزء السفلي لتكوين الباهي، بالجزء الشمالي الغربي من حوض سرت الترسيبي، من أجل وصف نسيج الصخور واستنتاج بيئة الترسيب إلى جانب إختبار التقنيات الحديثة لإستنباط تلك البيئة.

الجزء السفلي من صخور الباهي الرملية عبارة عن رمال ناعمة إلى شديدة الخشونة ورديئة إلى متوسطة الفرز، وجيود حجم ناعمة إلى خشنة، ومعيار تفرطح متوسط إلى مرتفع. وتشير مؤشرات التوزيع التكراري لحجم الحبيبات إلى تكون نموذج مزدوج ضعيف. وقد وجد بأن مؤشرات درجة الفرز والجيود منسجمة والطبوغرافية والمنحدرات القديمة.

وتدل استقراءات البيئة القديمة، المبنية على مزج أربعة معايير حجم لحبيبات متباينة، التي تم الوصول إليها من خلال إستعمال منحنيات الإحتمالات المتراكمة والتباين الطبقي الإقليمي في معايير حجم الحبيبة الواحدة، على أن الصخور الرملية هذه قد غلبت على بيئة ترسيبها الظروف النهرية.

ABSTRACT

A detailed investigation of the lower part of the Bahi Formation in the northwestern Sirt Basin was undertaken to describe its sedimentological texture, to determine its environment of deposition as well as to test the existing techniques of environmental analysis.

The lower part of the Bahi sandstone is fine to very coarse, poorly to moderately well sorted, fine to coarse skewed, and mesokurtic to leptokurtic sand. Grain size frequency distributions tend to exhibit a weakely developed biomodality. Sorting and skewness, consistent with changes in local paleotopography and regional paleoslope.

Environmental interpretations based on four bivariate grain size parameters combinations were achieved with cumulative probability curve techniques and with the regional stratigraphic variations in single grain size parameters. A fluvial sand body environment is deduced.

*Petroleum Research Centre, P.O. Box 6431, Tripoli, G.S.P.L.A.J.

INTRODUCTION

Many previous workers have used the grain size distribution of classic sediments to characterise depositional environments, to recognise the mechanisms of sediment transport and deposition, and to differentiate between environmental settings (Folk and Ward, 1957; Passega, 1957, 1964; Mason and Folk, 1958; Steward, 1958; Friedman, 1961, 1967; Moiola and Weiser 1968; Passega and Byramjee, 1969; Visher, 1969; Folk, 1974; Moshrif, 1980; Abu El-ella and Coleman, 1985).

There have been no detailed grain size analysis of the Bahi Formation in the northwestern part of the Sirt Basin (Az Zahara-Hofarah Platform). Mechanical sieve analysis ($\frac{1}{2}$ phi) were carried out on a total of forty five samples of the Bahi sandstone in the A2-32, A4-32 and F6-32 boreholes (Fig. 1). These samples cover most of the succession, except for the uppermost part (a glauconite-bearing marine sequence) which has not been analysed because of unavailability of samples.

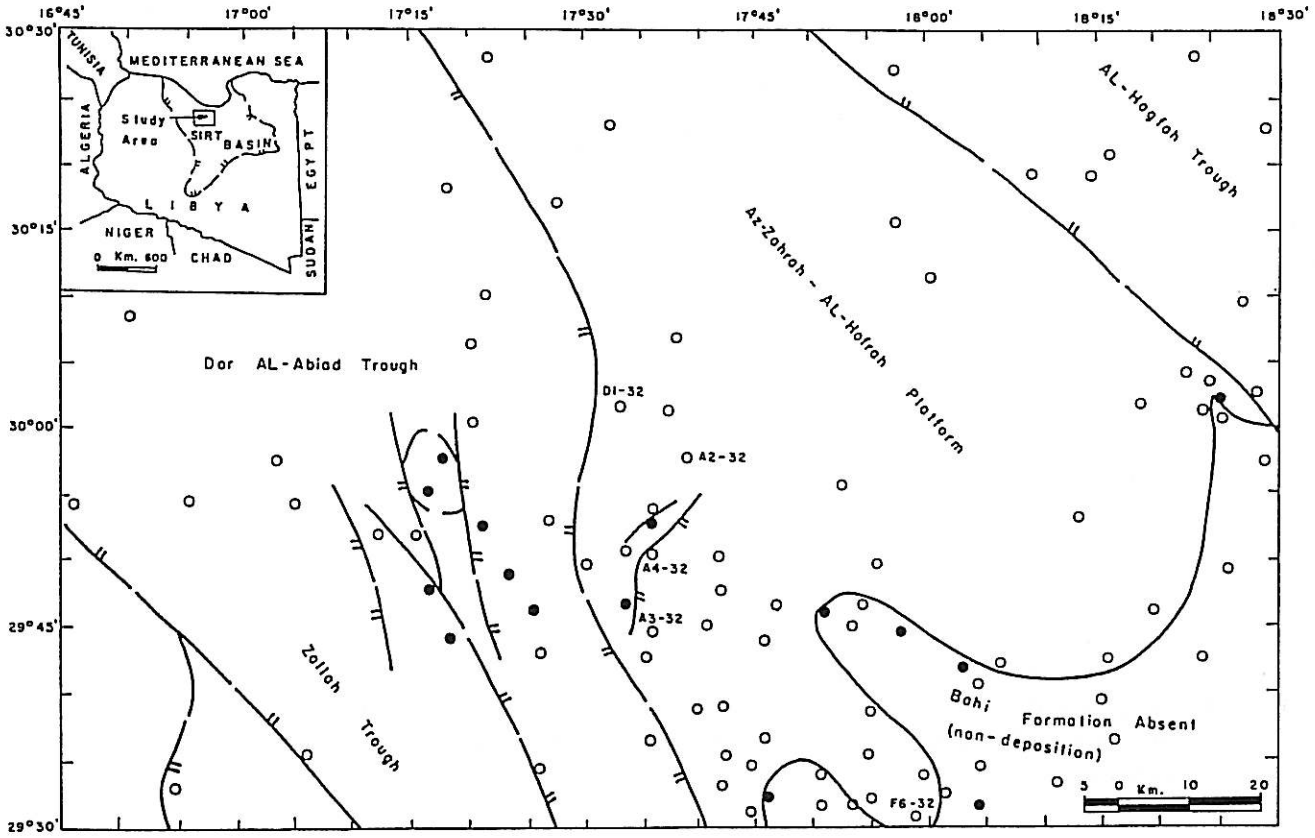


FIG. 1. Map showing the geographic location of the study area.

The work was carried out with the following objectives: To determine vertical and lateral texture variation within the Bahi Formation; to give a clear idea of the depositional environments of the formation and to throw light on the transporting agents of the sediment.

STRATIGRAPHY

The Bahi Formation is found in the subsurface of the northwestern part of the Sirt Basin. It attains a maximum thickness of about 110 meters in A3-32. In various places, the Bahi Formation is overlain by the Lidam Formation or other younger Upper Cretaceous formations (Argub, Rachmat, Sirt, Kalash, etc.), ranging in age from Cenomanian to Maastrichtian, and it is seen to unconformably overlie the Cambro-Ordovician Hofra Formation; in the D1-32 borehole, it rests uncomformably on Devonian sediments. It can be concluded, then, that the Bahi Formation is a diachronous unit, ranging in age from Cenomanian to Maastrichtian (Sghair, 1990).

At the beginning of the Cenomanian and continuing the Maastrichtian, a transgressive sandy base is recognised which has been given various names in the Sirt Basin (Bahi, Maragh, Basal Sandstones, etc.). During this timespan a major transgression took place in northern Libya. The Bahi Formation at the base of the succession is made up of interbedded sandstone, siltstone, conglomerate and shale. Sandstone is the most common lithology: it is usually medium to coarse in texture with subangular to angular quartz grains. Glauconite is common in the uppermost part, 3 to 6 meters, thick, but seems to be absent in the lower part. The siltstone and shale are red or mottled. Usually there is a basal conglomerate 3 to 6 m thick), consisting of rounded quartzic pebbles with a sandy or shaley matrix (Barr and Weegar, 1972).

METHOD AND PROCEDURES

In the laboratory, samples were evenly crushed and checked using a binocular microscope to ensure that the grains were completely separated. The samples were dried and 50 grams were weighed and sieved using $\frac{1}{2}$ phi sieve intervals for 15 minutes on a Ro-Tap shaker. Each fraction was weighed by a beam balance accurate to one hundredth of a gram and the frequencies were then obtained. From the grain-size analysis data, cumulative frequency curves were drawn on arithmetic probability paper using a phi scale. Other grain-size parameters determined include maximum size, median size, and "C" the first percentile in the grain-size distribution (Passega, 1957).

Grain size statistical parameters; mean size, standard deviation, skewness and kurtosis, were calculated using linear interpolation on the weight percentage distributions and the following formulas (Folk and Ward, 1957):

$$\text{Mean size} = \frac{P16 + P50 + P84}{3};$$

$$\text{Standard deviation} = \frac{P84 - P16}{4} + \frac{P95 - P5}{6.6}$$

$$\text{Skewness} = \frac{P16 + P84 - 2P50}{2(P84 - P16)} + \frac{P5 + P95 - 2P50}{2(P95 - P5)};$$

$$\text{Kurtosis} = \frac{P95 - P5}{2.44(P84 - P16)}$$

Where P16, P50 etc. are the grain size in phi units ($-\log 2$ of grain size in mm) corresponding to the 16th, 50th, etc. percentiles on the cumulative curve of grain size distribution. Subsequently, graphs of all possible parameters were made.

GRAIN SIZE DISTRIBUTION

The most commonly used method of displaying the results of grain size analysis is by plotting cumulative percentage against grain size, expressed on a logarithmic scale. The comparison of grain size curves and the interpretation of separate populations is aided by the use of log probability plots. The interpretation of the shapes of cumulative grain size distributions in terms of sedimentary response to hydraulic conditions has attracted the attention of many geologists (e.g. Visher, 1969; Freeman and Visher, 1975). The cumulative curve for each sample was first drawn separately, then the curves representing each borehole were compounded on the same plot. Representative cumulative curves are given in Figs. 2a–c. It should be kept in mind that the record reflected by the grain size analysis has been affected by diagenetic changes in that some grains have been enlarged by overgrowth and some reduced in size by pressure solutioning. An additional problem in the grain size distribution studies is that the same sedimentary processes occur in a number of environments and thus textural results are similar. Bearing these constraints in mind, examination of the different segments in each cumulative curve leads to the following general observations:

(1) The suspension population represents about 10% of the distribution in most samples. This may also contain small heavy minerals which belong to the 'tractive' load.

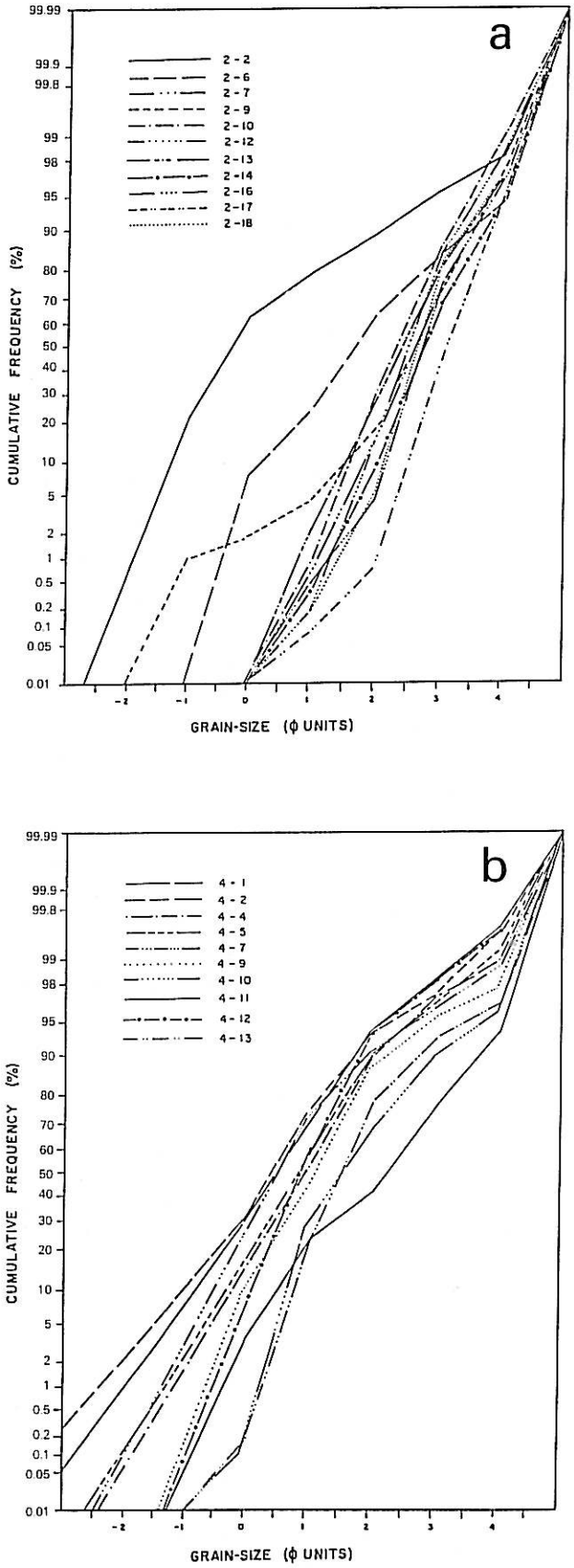
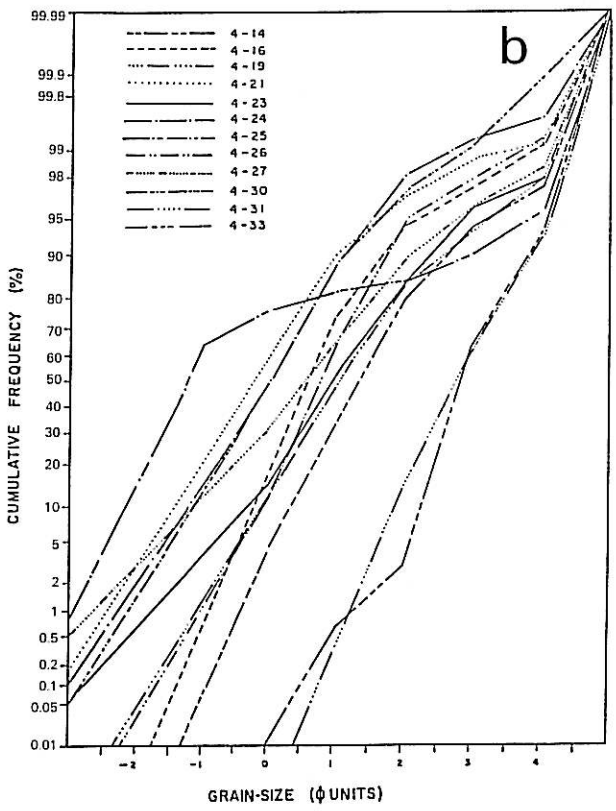


FIG. 2. Cumulative-frequency curves, showing the relationship between sediment transport dynamics with populations and truncation points in a grain-size distribution.



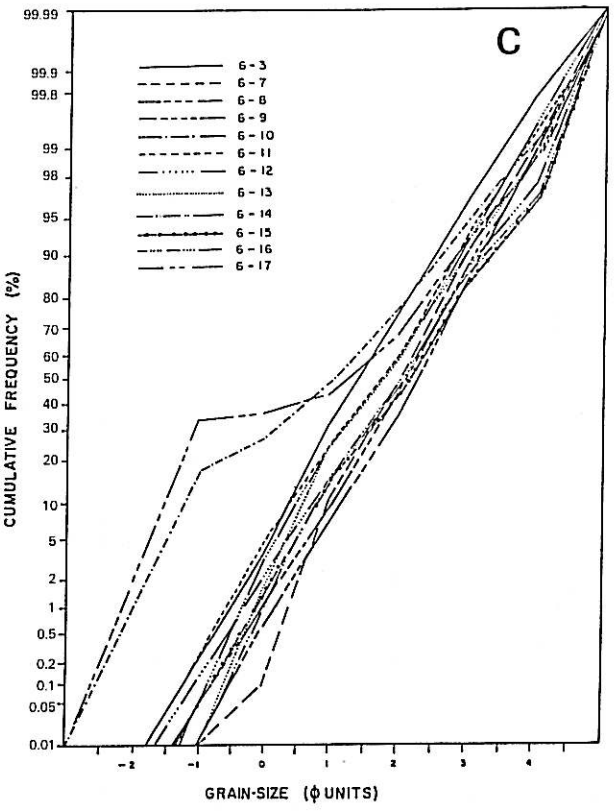


FIG. 2.—*Contd.*

(2) The saltation population is well developed: it represents more than 85% of the distribution.
(3) The traction population is usually very small and represents only about 1% of the distribution, except for a few samples where it represents more than 60% of the distribution. This reflects two main modes of transportation of the Bahi sediment; a saltation load transport for most samples and surface creep or rolling transport for others.

STRATIGRAPHIC VARIATION IN GRAIN-SIZE PARAMETERS

The formulae of Folk and Ward (1957), and Folk (1974), have been used in this study, to determine grain size statistical parameters (mean size, standard deviation, skewness, kurtosis), because they cover most of the sediment distribution data for the Bahi samples especially in the tails of the distribution. Vertical profile for each borehole in the Bahi Formation shows the stratigraphic variation in mean size, standard deviation, skewness and kurtosis (Figs. 3a–c).

Mean Characteristics

The mean size value of the Bahi sediment in the A2-32 borehole ranges between 3.13 to 1.75 phi (very fine to fine sand) in most of the samples. One sample has a value of −0.02 phi (very coarse sand) in the upper part of the section. However, this section can be divided into two parts according to the mean size value, the sediment in the lower part being very fine to fine sand and, in upper part, very coarse sand (Fig. 3a). Whereas in the A4-32 borehole the mean size values range between 2.95 to −1.50 phi (fine to very coarse sand). Here the Bahi sandstone can be divided according to the mean size of the sediments. In the lower part, the mean size value shows a coarsening upward pattern from fine into coarse and then very coarse sand followed by repetitive grading from medium to coarse sand. In the upper part the mean size values range from fine to medium into coarse and very coarse sand (Fig. 3b). While the mean size value in the F6-32 borehole ranges between 2.23 and 0.43 phi (fine to coarse sand). According to the grain size values the Bahi sandstone can be divided into; the lower part, coarsening upward from fine to medium to coarse sand, and the upper part, also coarsening upward, ranging from fine to medium sand (Fig. 3c). Generally, the overall mean size values of the three borholes exhibit a coarsening upward trend from very fine sand to very coarse sand. This variation in mean size could be related to variation in the energy of transporting agents and/or change in the source of the sediment during deposition.

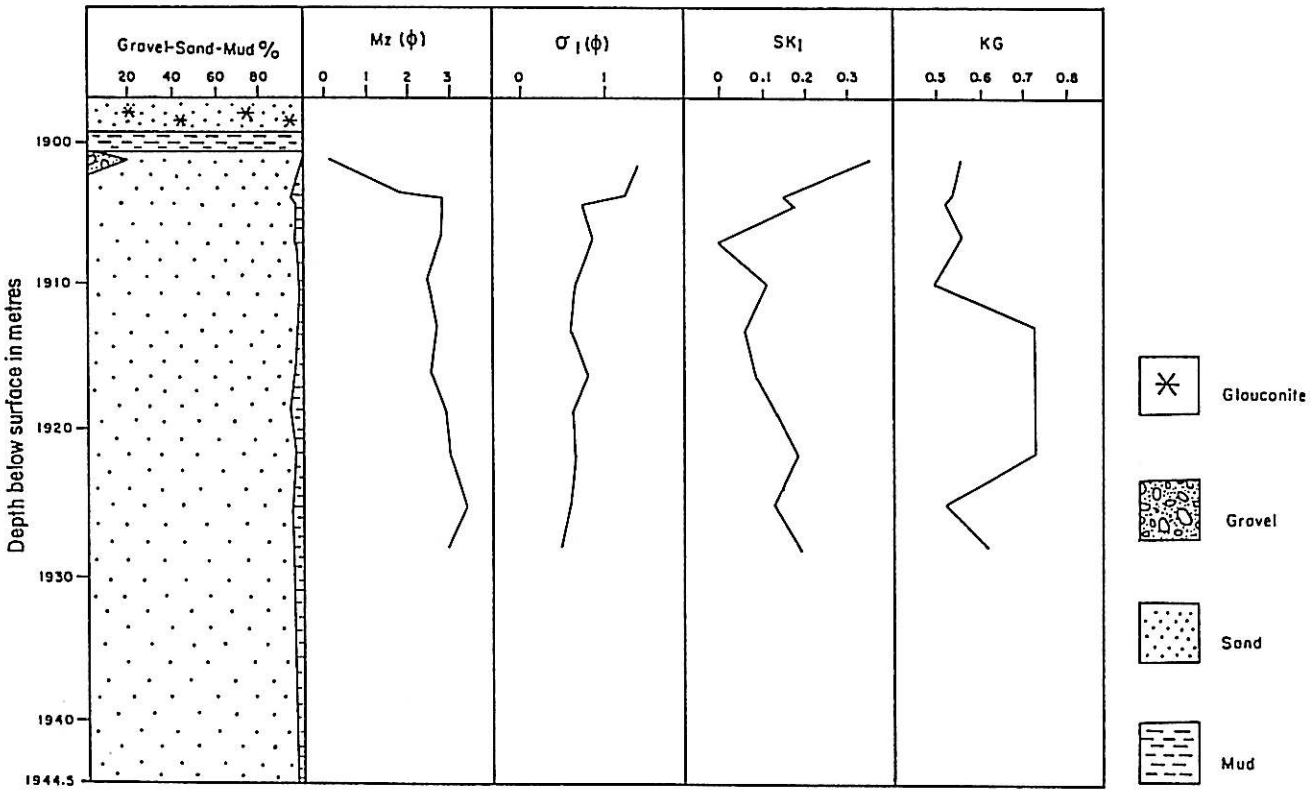


FIG. 3a. Vertical variation of gravel-sand-mud composition and grain-size parameters in the Bahi Formation (A2-32 borehole).

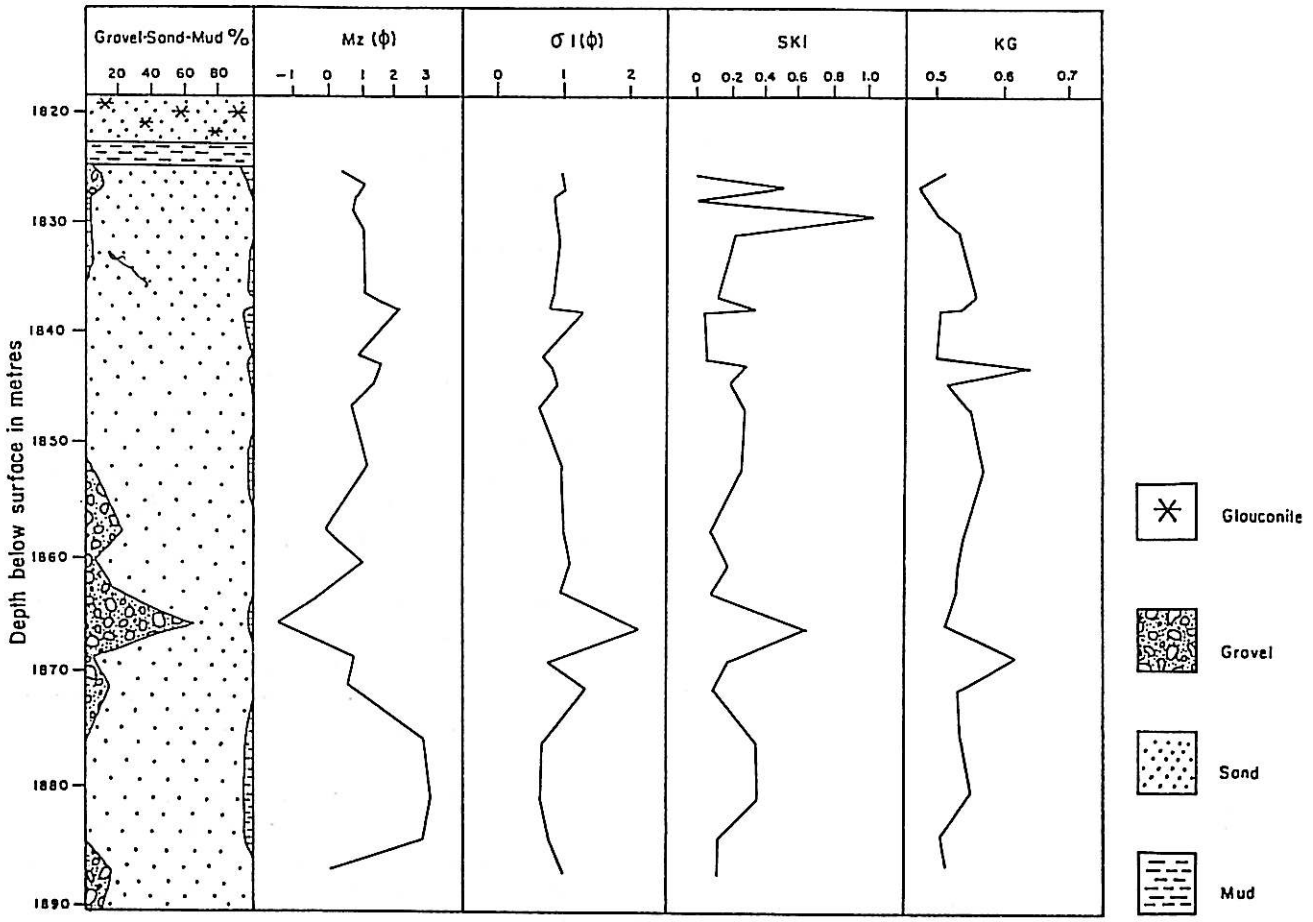


FIG. 3b. Vertical variation of gravel-sand-mud composition and grain-size parameters in the Bahi Formation (A4-32 borehole).

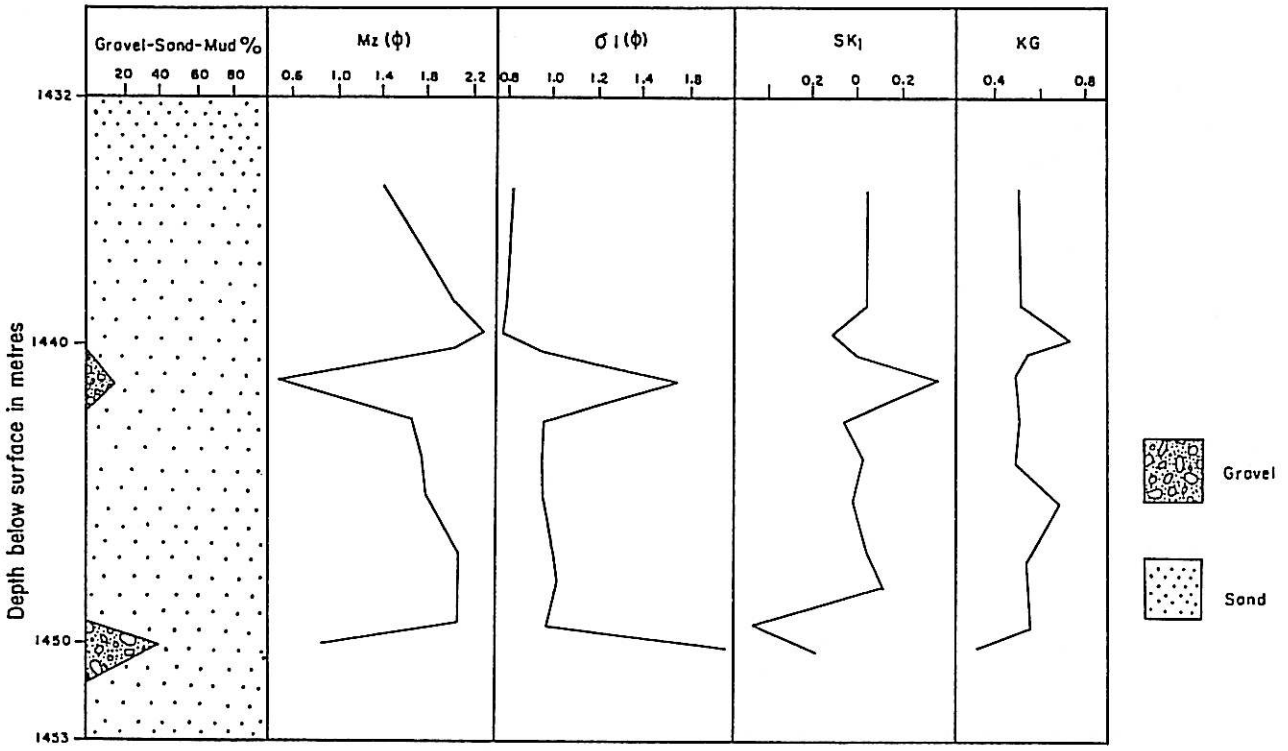


FIG. 3c. Vertical variation of gravel-sand-mud composition and grain-size parameters in the Bahi Formation (F6-32 borehole).

Sorting Characteristics

Most of the samples in the A2-32 borehole are moderately to moderately well sorted (8 out of 11) and show uniform standard deviation values ranging between 0.50 and 0.79 phi, with an average of 0.62 phi. The remaining three samples of which two are from the upper part of the section sampled, are poorly sorted, ranging between 1.19 and 1.37 phi, and one sample from the lowest part of the section is well sorted, 0.38 phi, (Fig. 3a). Whereas the samples from the A4-32 borehole are moderately to moderately well sorted (16 out of 22), and show uniform standard deviation values ranging between 0.60 and 0.98 phi with an average of 0.79 phi. The remaining samples are poorly to very poorly sorted and range from 1.03 to 2.09 phi with an average of 1.31 phi (Fig. 3b), whereas in the F6-32 borehole the samples are moderately sorted (10 out of 12), and show uniform standard deviation values ranging between 0.77 and 0.97 phi with an average of 0.8 phi, except for two samples from the upper and lowest part of the sampled section which are poorly sorted and range between 1.52 and 1.71 phi with an average of 1.62 phi (Fig. 3c). Lateral and vertical variation of the sorting in the Bahi sediment from one borehole to another may reflect different sediment sources but may also reflect the nature of the transporting agents at the time of deposition.

Skewness Characteristics

Values of inclusive graphic skewness in the A2-32 borehole, range from the strongly fine skewed to near symmetrical, with an overall range between -0.01 and $+0.34$ (Fig. 3a), whereas in the A4-32 borehole, skewness values range from strongly fine skewness to a near symmetrical curve, with an overall range between -0.07 and 0.56, except for one sample which shows a strongly coarse skew 0.56, (Fig. 3b). In the F6-32 borehole, skewness values range from strongly fine skewed to strongly coarse skewed, with an overall range between -0.49 and $+0.33$ (Fig. 3c).

The overall average inclusive graphic skewness in the three boreholes show strongly fine skewed to a near symmetrical distribution. This asymmetry in the sediment distribution, both laterally and vertically, may result from multiple sources for the Bahi sediment.

Kurtosis Characteristics

In the samples from the A2-32 borehole, graphic kurtosis is leptokurtic to very leptokurtic with a range between 1.134 and 2.596, except for three samples from the middle and lower part of the sampled section which are mesokurtic (Fig. 3a). In the A4-32 borehole, the samples are leptokurtic to very leptokurtic with ranges between 0.134 and 1.517, except for eight samples which are mesokurtic and

one which is platykurtic (Fig. 3b). In the F6-32 borehole, most of the samples are mesokurtic with ranges between 0.907 and 1.092. Two samples however are very leptokurtic, two are platykurtic and one sample is very platykurtic (Fig. 3c). Generally, the Bahi sediment in these boreholes is leptokurtic to very leptokurtic, indicating that the central part of the samples are better sorted than the tails, whereas some samples are mesokurtic, showing similarity in sorting between the central and the tails portions of the sediment distribution curves. This indicates different degree of sorting which may reflect multiple sources for the sediment and/or more than one mode of transportation.

ENVIRONMENTAL INTERPRETATION

For more than 30 years sedimentologists have been seriously attempting to use textural analysis to deduce depositional environments. Scatter plots of inclusive standard deviation against inclusive graphic skewness, inclusive standard deviation against graphic mean size and median against inclusive standard deviation have been constructed in an attempt to recognise the depositional environment or environments for the Bahi sediment.

Plots of inclusive standard deviation against graphic skewness have been used by many workers to differentiate between river and beach sands (e.g. Friedman, 1961 and 1967; Moiola and Weiser, 1968 and others). Friedman (1967) shows that a plot of inclusive graphic skewness versus inclusive graphic standard deviation gives a good separation between beach and river sands. Beach sands tend to be better sorted than river sands and thus tend to have lower numerical standard deviation values (Friedman, 1961). A plot of these two grain size parameters for the Bahi samples in the three boreholes is shown in Fig. 4. Using Friedman (1967) and Moiola and Weiser (1968) boundary lines, the majority of the samples are classified as river sands except for one sample from the A2-32 borehole which is classified as a beach sand. None of the analysed samples in the three boreholes include the uppermost part of the formation which is known, on mineralogical grounds, to represent the initiation of a marine cycle (glauconitic sandstone).

Plots of standard deviation against mean size is also considered to be most effective in differentiating between depositional environments. Moshrif (1980) used a combination of the "environmental boundaries" of Friedman (1961, 1967) to differentiate between beach, dune and river sands. Applying these boundary lines to the Bahi samples from the three boreholes (Fig. 5a), most of them are classified as river sands, whereas a few samples from the A2-32

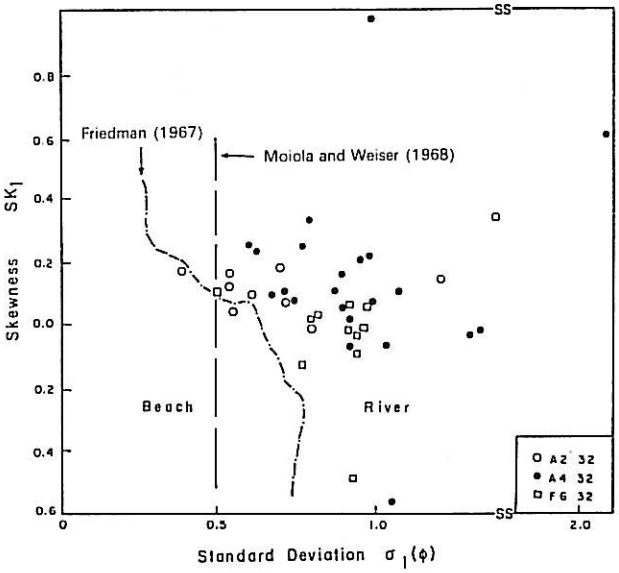


FIG. 4. Plot of inclusive graphic standard deviation against inclusive graphic skewness, showing the environment of deposition in the Bahi Formation in the boreholes studied, based on Friedman (1967) and Moiola and Weiser (1968).

and A4-32 boreholes are classified as dune sands. Applying Moiola and Weiser's framework (1968) for these parameters (standard deviation and mean size), show, however, that all the analysed samples are classified as river sands (Fig. 5b).

Steward (1958) used a scatter plot of standard deviation against median to differentiate between

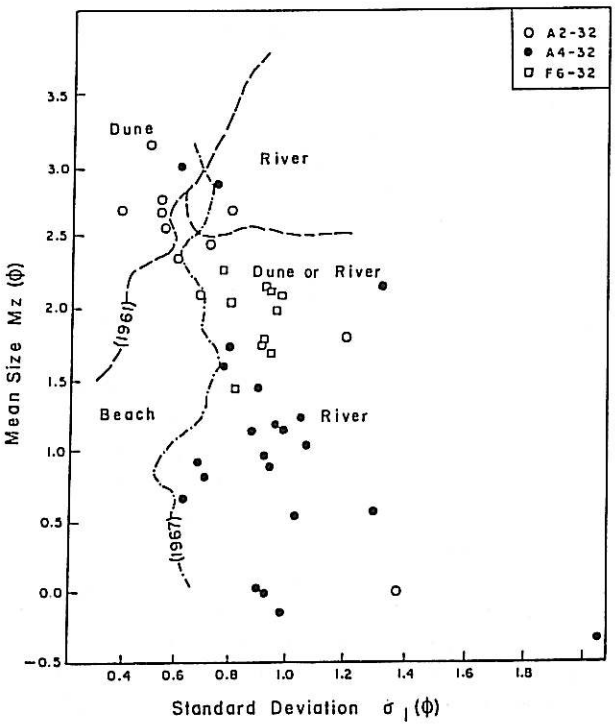


FIG. 5a. Plot of inclusive graphic standard deviation against mean size, showing the environment of deposition in the Bahi Formation in the boreholes studied, based on Friedman (1961, 1967).

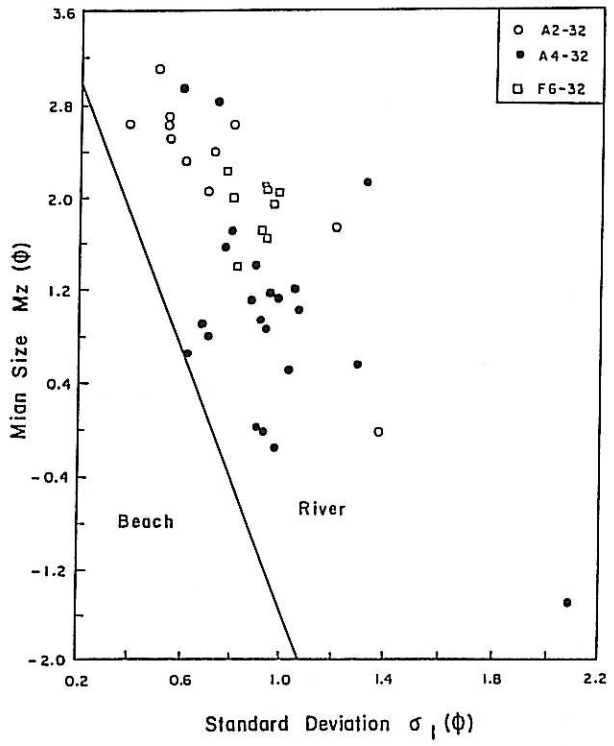


FIG. 5b. Plot of inclusive graphic standard deviation against mean size, showing the environment of deposition in the Bahi Formation in the boreholes studies, based on Moiola and Weiser (1968).

river processes, wave processes, and slow deposition in quiet water. Stewart's diagram (Fig. 6), shows that wave processes are responsible for most of the samples in the Bahi sandstone in the A2-32 borehole, and the river processes for most of the samples in the A4-32 borehole, except for two samples which fall on the wave processes side. Seven samples in the F6-32 borehole fall on the river processes side and one sample falls on the wave processes side. The remaining samples from the three boreholes fall outside both fields. They fall close to the river processes field, and their plot position may not be particularly significant. This suggests that the Bahi sediments were deposited under the changing mechanical conditions which would be expected as a fluvial regime passed, by degrees, into a littoral one.

Passega (1957, 1964) stated that sample point patterns representing the variations in a deposit of two parameters, C and M, are characteristics of the depositional agent. The C is the one percentile diameter (in micron), an approximation of the maximum grain size; and M is the fifty percentile particle diameter, the median. Passega stated that the CM pattern is geological tool which can be used to analyse the depositional conditions in recent sediments and thus enable a reconstruction to be made of the conditions of deposition for ancient sediment suites. The CM diagram illustrates the relationship between grain size

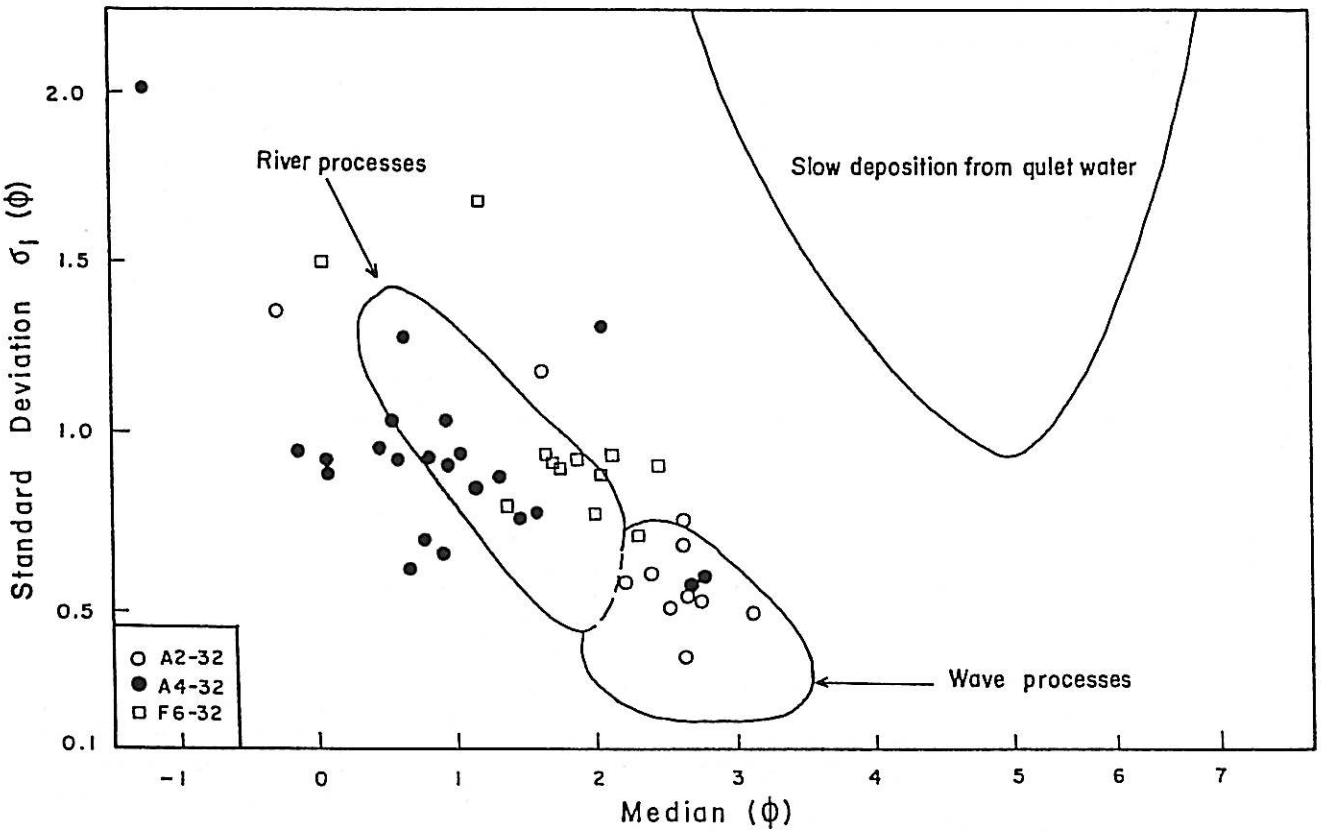


FIG. 6. Plot of inclusive standard deviation against median, showing the nature of deposition of the Bahi Formation in the boreholes studied, based on Steward (1958).

and the hydraulic conditions under which clastic deposits have accumulated. Passega (1964) subdivided the CM patttern by points N, O, P, Q, R and S into five segments each of which corresponds to a particular sedimentation mechanism. This implies that clastic sediments of a certain grain size are available under particular hydraulic conditions. The mechanism of transportation are represented mainly by rolling (NO); rolling and suspension (OP); suspension and rolling (PQ); graded suspension (QR) and uniform suspension (SR). Pelagic suspension (T) represents the finest sediments (below 15 micron). In 1969 Passega and Byramjee further subdivided the CM diagram into 9 classes as shown in Fig. 7. Data falling in classes I, II, III, and IX indicates that the grains have been transported by rolling while those falling in classes IV, V, VI, VII and VIII indicate grains which have been transported by saltation. The CM technique is mostly applied at the lamina scale but in this study has been applied to all grain size analysis samples even though the value may be limited.

Fig. 7, shows the distribution for the samples from the Bahi sediment in the three boreholes. Most of the samples in the A2-32 borehole fall within classes IV and V, indicating that they were transported by saltation, except for two samples which fall in classes I and II indicating that they were transported by rolling. In the A4-32 and F6-32 boreholes, most of the samples fall in class I indicating that they were transported by rolling, except for two samples in F6-32 borehole which fall in class IV indicating that they were transported by saltation.

CONCLUSIONS

Keeping in mind that grain diminution and overgrowth may modify the size characteristics of the sediment, and the fact that the cement may itself break down into grains the following general conclusions can be drawn:

Cumulative frequency curves show two main modes of transportation for the Bahi Sandstone; saltation load transport for most of the samples and surface creep or rolling transport for the others.

Histograms show that most of the Bahi Sandstone samples are unimodal for the A2-32 and A4-32 boreholes, with few samples showing biomodality in the latter borehole, whereas in the F6-32 borehole the majority of the samples show a biomodal distribution.

Sediment distribution in the formation exhibits a coarsening upward trend ranging from very fine to very coarse sand, moderately to very poorly sorted, characterized by a strongly fine to strongly coarse

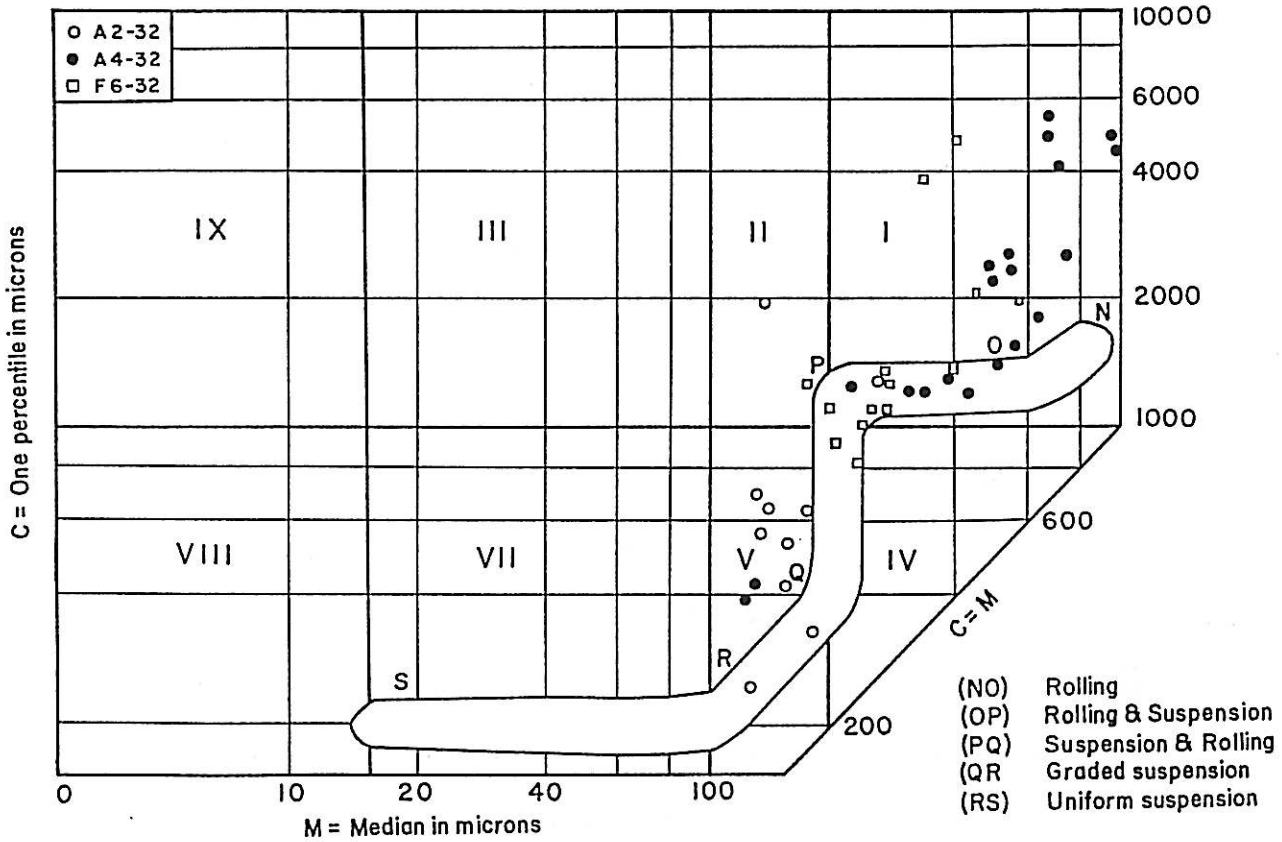


FIG. 7. Plot of C (1st percentile) against M (Median in diameter), showing the nature of transportation of the Bahi Formation in the boreholes studied, based on Passega and Byramjee (1969).

skewness which varies from leptokurtic to very leptokurtic with some samples being mesokurtic. This variation could be related to variation in the energy of transportating agents and/or changes in the source of the sediment during the Bahi deposition.

Sorting data plotted against mean size and skewness show that the Bahi Formation largely comprises river sands, with few samples which are to be regarded as beach sands.

Sorting evidence plotted against the median shows that the process agent for the Bahi sediment is river and wave systems.

ACKNOWLEDGEMENT

This paper is a part of a thesis submitted to Glasgow University, Scotland., The work was sponsored by the Petroleum Research Centre.

I particularly wish to thank Dr. J.K. Ingham, who supervised the thesis. I am specially grateful to Prof. B. Bluke from the Geology Dept., Glasgow University, for his helpful support for clarifying many doubts and problems.

I would like to express my thanks to the National Oil Corporation and Oasis Oil Company, Tripoli, Libya for permitting and providing the rock samples for analysis.

REFERENCES

Abu El-elela, R. and Coleman, J.M., 1985, Discrimination between the Depositional Environments using Grain-Size Analysis, 32, 743-748.

Barr, F.T. and Weegar, A.A., 1972, Stratigraphic Nomenclature of the Sirt Basin, Libya, Petroleum Exploration Society of Libya, Grafiche Trevisan Castle Franco, Italy, 179 pp.

Folk, R.L., 1954, The Distinction between Grain Size and Mineral Composition in Sedimentary Rock Nomenclature, J. Geol., 62, 344–359.

Folk, R.L. and Ward, W.C., 1957, Brazos River Bar: A Study in the Significance of Grain-Size Parameters, J. Sedim. Petrol., 27, 3–26.

Folk, R.L., 1974, Petrology of Sedimentary Rocks, Hemphill Publ. Co., Austin, Texas, 181 pp.

Freeman, W.E. and Visher, G.S., 1975, Stratigraphic Analysis of the Navajo Sandstone. J. Sedim. Petrol., 45, 651–668.

Friedman, G.M., 1961, Distinction between Dune, Beach, and River Sands from their Textural Characteristics, J. Sedim. Petrol., 31, 514–529.

Friedman, G.M., 1967, Dynamic Processes and Statistical Parameters Compared for Size Frequency Distribution of Beach and River Sands, J. Seim. Petrol., 37, 327–354.

Mason, C.C. and Folk, R.L., 1958, Differentiation of Beach, Dune and Aeolian Flat Environments by Size Analysis, Mustang Island, Texas, J. Sedim. Petrol., 28, 211–226.

Moiola, R.J. and Weiser, D., 1968, Textural Parameters; An Evaluation. J. Sedim. Petrol., 38, 45–53.

Moshrif, M. A., 1980, Recognition of Fluvial Environments in the Biyadhi-Wasia Sandstones (Lower-Middle Cretaceous) as Revealed by Texture Analysis. J. Sedim. Petrol., 50, 603–612.

Passega, R. 1957, Texture as Characteristic of Clastic Deposition. Bull. Am. Assoc. Petrol. Geol., 41, 1952–1984.

Passega, R., 1964, Grain Size Representation by CM Patterns as a Geological Tool. J. Sedim. Petrol., 34, 830–847.

Passega, R. and Byramjee, R. 1969, Grain-Size Image of Clastic Deposits, Sedimentology, 13, 233–252.

Sghair, A.M., 1990, Stratigraphy, Lithofacies and Environmental Analysis of the Bahi Formation (Late Cretaceous) in the Northwestern Sirte Basin, Libya, M.Sc. Thesis 171 p.

Steward, H.B., 1958, Sedimentary Reflections of Depositional Environments in San Miguel Lagoon, Baja California, Mexico, Bull. Am. Assoc. Petrol. Geol., 42, 2567–2618.

Visher, G.S., 1969, Grain Size Distribution and Depositional Process, J. Sedim. Petrol., 1074–1106.

PRJ, Vol. 5 (January 1993); P. 56–61, 6 FIGS, 2 TABLES.

MICROPROBE ANALYSIS OF THE GLAUCONITE PELLETS OF THE LIDAM FORMATION NW SIRT BASIN, LIBYA

M. El-Bakai*

استخدام المسبار المجهري في دراسة حبيبات الجلوكونيت بتكوين الليدام بالمنطقة الشمالية الغربية لحوض سرت الترسيبي

محمود البكاي

تم تصنيف معدن الجلوكونيت في تكوين الليدام ، بالمنطقة الشمالية الغربية من حوض سرت الرسوبي ، إلى ثلاثة أنواع هي خضراء غامقة وخضراء فاتحة والصفراء البنية .

وقد بينت الفحوصات ، التي أجريت باستخدام المسبار المجهري ، للثلاثة أنواع بأن الحبيبات الصفراء البنية المصغرة كانت أصلاً حبيبات خضراء غامقة غير أن الألومينيوم السداسي الأوجه حل محل أيونات الحديديك والحديدوز وكذلك البوتاسيوم . وتعكس هذه الحبيبات ، الصفراء البنية ، التأثير الكبير لظروف الأكسدة ، إما من خلال التكشف أو أثناء تنقلها بواسطة تيارات المياه الضحلة العكرة في أوقات انخفاض مستوى مياه سطح البحر أثناء المرحلة السينومانية المتأخرة والمرحلة التورونية المبكرة . أما الحبيبات الداكنة اللون ربما تمثل المرحلة الإنتقالية ما بين النوعين الآخرين .

كما تبين الدراسة أن متوسط قيمة أكسيد البوتاسيوم بالحبيبات الخضراء الغامقة (معدن الجلوكونيت) يبلغ 8.7 الأمر الذي يعكس التركيز المحلي لأكسيد البوتاسيوم . وتشير استدارة حبيبات الجلوكونيت واحلال الدولوميت محلها بأنها ربما قد إنتقلت مبكراً على المنحدرات الخارجية . فحبيبات الجلوكونيت مؤشرات بحرية هامة ، عادة ما توجد بالبيئات الضحلة عند اعماق تتراوح بين 60 و500 م . فهي من خصائص الأجزاء الداخلية للأرفف القارية ، وتمثل هذه الطبقة الغنية بالجلوكونيت ، والتي ترجع إلى المرحلة السينومانية ، قاعدة تتابع يمثل تقدم مياه البحر.

ABSTRACT

The glauconite pellets of the Lidam Formation in north-west Sirt Basin, Libya, have been classified into three types. They are grass-green pellets, light-green pellets and brownish-yellow pellets.

The microprobe analysis of the three types shows that the brownish-yellow pellets are the same as grass-green pellets, but the Fe^{3+}, Fe^{2+} and K were possibly replaced by Al_{VI}. These brownish-yellow grains reflect a history of more oxidizing conditions, either through subaerial exposure or transport in shallow turbulent waters during Upper Cenomanian-Lower Turonian low sea level stands. The light-green pellets represent the transition stage between the other two types. It also shows that the mean values of K_2O in the grass-green pellets (glauconite mineral) is 8.7 which reflect localized concentration of K_2O. The roundness of glauconite pellets and their replacement by dolomite suggest that they might have been transported early to the outer ramp. The glauconite pellets are a valuable marine indicator. They occur mainly in relatively shallow water, at depths between 60–500 m. They are particularly characteristic of the inner part of the continental shelf. This highly glauconitic bed of Cenomanian age mark the base of a transgressive sequence.

INTRODUCTION

The Lidam Formation in the study area (Fig. 1) is composed of very shallow marine carbonates with thin lenses of sandstones, particularly in the lower part. The lower part of the Lidam Formation shows a local mixing with the sandstone of the Bahi formaton. Very common greenish-grey dolomitic

*Petroeum Research Centre, P.O. Box 6431, Tripoli, G.S.P.L.A.J.

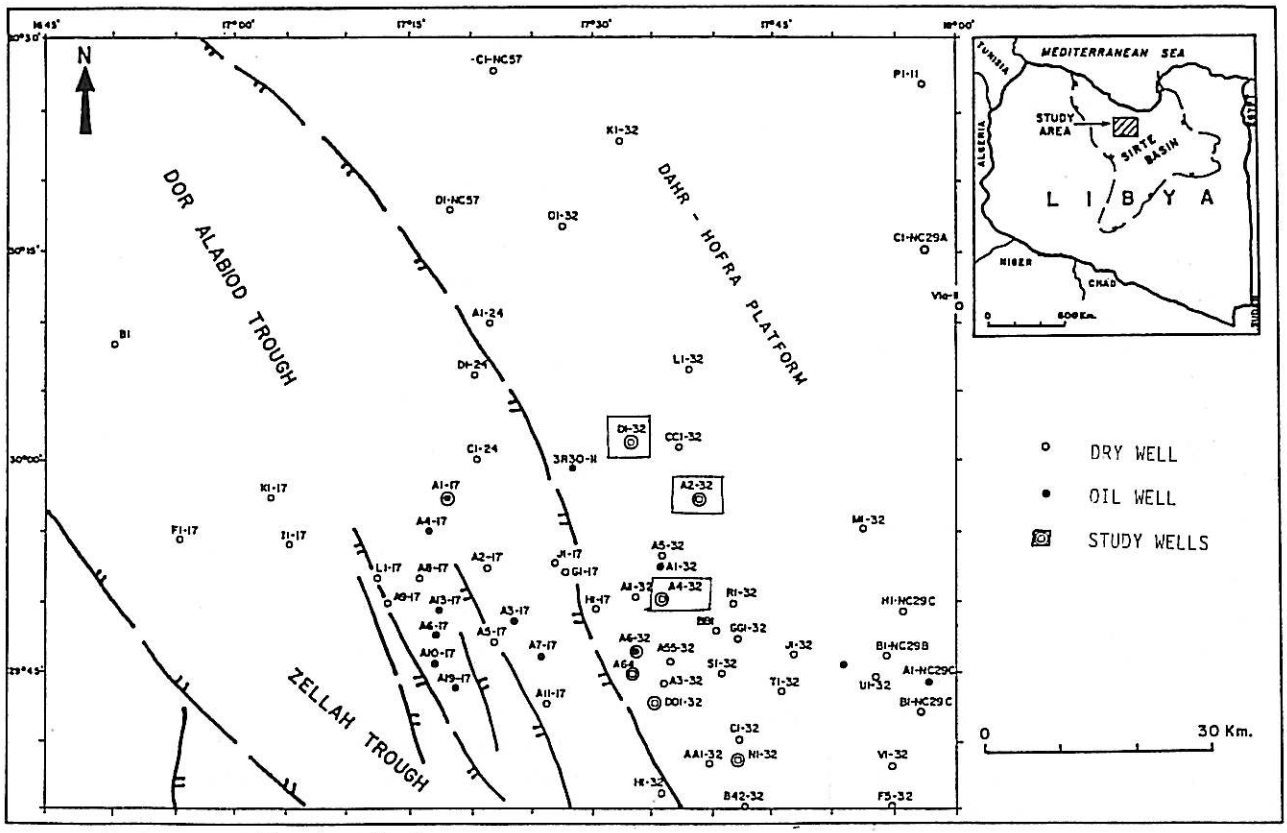


FIG. 1. Study area and location of wells.

glauconite beds were encountered in wells D1-32 and A2-32. Glauconite pellets were found throughout the Lidam sediments, but more commonly in the lower part (El-Bakai, 1989).

The Lidam Formation unconformably overlies various units including the Nubian Formation, the Bahi Formation and igneous-metamorphic basement. It is usually overlain by the Upper Cretaceous Etel Formation with apparent conformity (Barr and Weegar, 1972). The Lidam Formation is considered as Cenomanian in age by Barr and Weegar, (1972, p. 121–122). Hammuda *et al.* (1985), documented this formation as Cenomanian-Turonian in age.

STRATIGRAPHY

The Lidam formation in its type section (Fig. 2), consists mainly of well to moderately cemented calcarenite, calcilutite containing skeletal material and pellets at the upper part. The rock of the Lidam Formation in the lower part is dominante by dark greenish glauconitic dolomite. The thickness of this interval varies between 3 to 6 metres. The size of the glauconite pellets in the lower part of the formation ranges from 0.3 to 20 mm. This zone of glauconite probably represents the base of the Cenomanian transgression in the Sirt Basin.

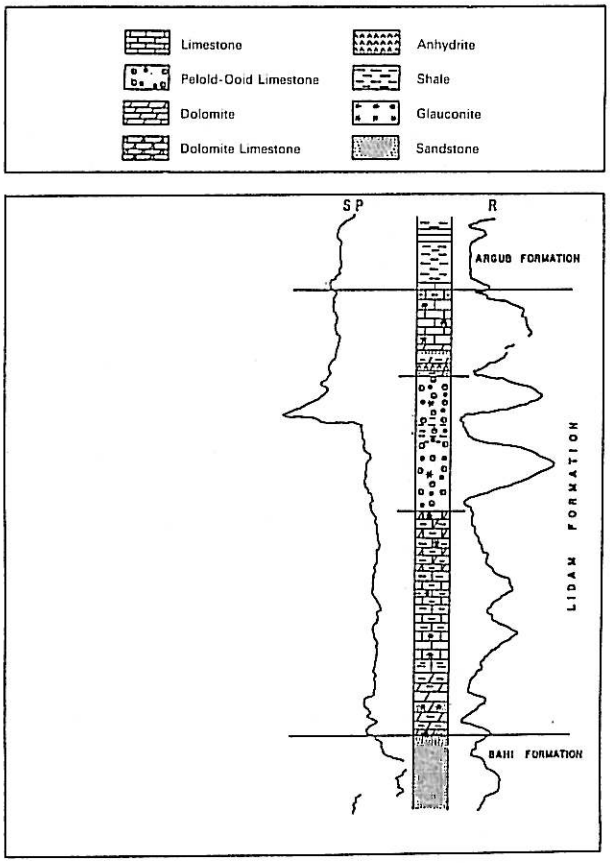


FIG. 2. Type well of the Lidam Formation in the study area (D1-32).

The Lidam Formation is considered Cenomanian in age. It is equivalent in age and, sometimes, in lithology to surface outcrops of the Yefren member and Nalut Formation in Jabal Nefusa North-Western Libya.

METHODS OF STUDY

Polished thin sections were prepared from selected core samples obtained from wells D1-32, A2-32 and A4-32.

The analysis of the glauconite pellets were made at the center and cortices of each pellet.

GENERAL STATEMENT

Glauconite is a mica mineral which occurs almost in marine sediments. It is generally accepted that glauconites are probably formed by marine diagenesis in shallow water during periods of slow or negative sedimentation. Its chemical formula is

$$(K, Na, Ca)_{1.2-2.0}(Fe^{+3}, Al, Fe^{+2}, Mg)_{4.0}$$
$$[Si_{7-7.6}Al_{1-0.4}O_{20}](OH)_4.n(H_2O)$$

The thickness of these intervals is 10 ft (3 m) in well A2-32 at depth 6215–6225 ft (1866–1869 m). It is 23 ft (7 m) thick in well D1-32 at depth 7190–7213 ft (2159–2166 m).

The polished slab cores are dark greenish-grey, highly bioturbated with pure dolomite concretions and assciated with pyrite nodules. No skeletal allochems can be observed in the thin-sections. Only interminate allochem ghosts occur, representing fossils completely replaced by either secondary anhydrite or dolomite crystals. Elsewhere in the Lidam Formaton e.g. the upper part of the formation, some glauconite had replaced shells or had filled micropores with echinoderms, bryozoans or foraminiferas.

The glauconite pellets are moderately well sorted and usually larger than the dolomite crystals and quartz grains. Their size range between 0.3 to 2 mm. The glauconite pellets are mainly well rounded to elliptical with rare irregular and narrow cracks. Their margins are limonite resulting from the oxidation of ferous iron (Adams *et al.*, 1984). They commonly occur in varying abundance throughout the entire sequence of the Lidam sediments in the study area (con. 32), and can be classified according to the colour into three types:

- Grass-green pellets
- Light-green pellets
- Brownish-yelow pellets

The three types are similar to those described by Baily and Atherton (1969).

Some glauconite pellets display brownish cores and pale green margins, while others show dark margins.

ELECTRON MICROPROBE ANALYSIS

Analysis of six polished thin-sections consisting of 30 to 75 glauconite grains using the Electron Microprobe shows significant differences between the three types of glauconite pellets. Microprobe analysis indicated higher content of FeO and K_2O for the grass-green and light grains, and lower content for the brownish grains. P_2O_5 and Al_2O_3 content are higher for the brownish pellets and much lower for the green pellets (Tables 1 and 2).

Iron and potassium: The analysis indicated that FeO content in the light-green pellets varies between 4.10% to 19.07% (mean 16.07%), FeO content in the grass-green pellets between 15.09% and 22.31% (mean 19%, Table 1), while in the brownish pellets FeO varies between 0.46% to 19.39% (mean 14.79%). Iron content was also found to vary significantly between the center and margin of the brownish grains. FeO content varied between 14.09% to 19.39% (mean 16.8%) in the margins of the brownish-yellow grains, whereas the variation is between 0.46% to 9.38% (mean 5.8%) in the core. Microprobe analysis of the grass-green glauconite pellets gave K_2O values from 7.97 to 9.36% (mean 8.7%) reflecting the highly localized concentration of K_2O.

The values of K_2O within the light-green glauconite grains range between 2.51% and 19.19% (mean 8.28%). The values within the brownish grains are from 0.2% to 9.1% (mean 8.15%). There are slight differences between the cores and margins of the light-green grains (mean value of cores is 7.68%, while it is slightly higher in the margins 8.98%). There are significant differences in K_2O values between the cortices and centers of the brownish grains; the mean value in cortices is 10.05% but in the center the mean value is much lower 6.15%.

Fig. 3 shows the relation between K_2O and FeO in the three glauconite pellets. The three glauconite grains show a direct correlation between FeO and K_2O. K_2O in light-green grains increases from about 7% at an FeO content of 12% to about 9.2% at an FeO content of 19%. It seems that potassium started to enter the glauconite during the second stage of formation after the grains have achieved and FeO content between 12–19% (Bornhold and Giresse, 1985). The same relationship was observed between K_2O and FeO in the grass-green and brownish-yellow glauconite grains (i.e. K_2O increases with increasing FeO content, see Fig. 3).

Table 1. Microprobe Analysis for Glauconite

SiO_2	TiO_2	Al_2O_3	FeO	MnO	MgO	CaO	Na_2O	K_2O	SO_3	P_2O_5	Total	Spot	Notes
52.95	0.00	10.75	15.81	0.00	4.43	0.19	0.00	8.37	0.00	0.00	92.49	1	GGC
53.00	0.00	10.26	16.02	0.00	4.89	0.18	0.40	8.05	0.00	0.00	92.80	2	GGM
52.81	0.00	12.30	15.23	0.00	3.75	0.48	0.00	8.18	0.00	0.00	92.75	3	GBM
52.90	0.00	14.95	11.55	0.00	3.77	0.28	0.00	7.49	0.00	0.00	90.94	4	GBC
51.58	0.00	14.92	10.75	0.00	3.63	0.47	0.00	7.42	0.00	0.00	88.76	5	GMB
53.22	0.00	9.75	16.31	0.00	4.60	0.33	0.31	8.05	0.00	0.00	92.57	6	GLC
51.98	0.00	9.63	17.62	0.00	4.38	0.23	0.28	8.43	0.00	0.00	92.57	7	GLM
51.21	0.00	8.83	19.27	0.00	3.89	0.17	0.00	8.73	0.00	0.00	92.10	8	GGC
51.51	0.00	10.05	19.09	0.00	3.92	0.00	0.48	9.00	0.00	0.00	94.05	9	GGM
53.58	0.00	11.03	15.09	0.00	4.32	0.24	0.00	7.97	0.00	0.00	92.23	10	GGC
51.55	0.00	9.80	16.55	0.00	4.18	0.24	0.00	8.02	0.00	0.26	90.60	11	GGM
52.34	0.00	11.37	15.48	0.00	3.75	0.32	0.00	8.25	0.00	0.22	91.73	12	GBC
52.43	0.00	11.99	15.16	0.00	3.73	0.37	0.00	8.25	0.20	0.35	92.48	13	GBM
51.92	0.00	11.39	15.97	0.00	3.92	0.28	0.00	4.46	0.22	0.26	92.42	14	GLC
52.75	0.00	9.97	17.03	0.00	4.20	0.28	0.00	8.88	0.00	0.22	93.33	15	GLM
49.22	0.00	11.96	14.09	0.00	4.20	2.32	0.00	7.62	0.22	1.83	91.46	16	GBM
49.39	0.00	11.49	14.54	0.00	3.85	0.20	0.00	7.74	0.00	0.36	87.57	17	GLM
52.26	0.00	11.80	16.16	0.00	3.63	0.48	0.00	8.43	0.23	0.29	93.28	18	GLM
49.70	0.00	8.16	20.42	0.00	3.46	0.17	0.39	9.26	0.00	0.00	91.56	19	GBC
52.31	0.00	12.53	12.38	0.00	4.25	0.29	0.00	6.933	0.27	0.34	89.30	20	GLC
52.25	0.00	12.52	12.94	0.00	4.45	0.53	0.00	7.36	0.26	0.24	90.55	21	GLM
51.40	0.00	8.70	17.19	0.00	4.31	0.00	0.00	8.21	0.00	0.33	90.14	22	GGC
51.96	0.00	8.67	17.49	0.00	4.17	0.26	0.00	8.33	0.22	0.22	91.32	23	GGM
51.94	0.00	8.75	19.07	0.00	3.58	0.52	0.26	9.19	0.00	0.35	93.66	24	GLC
51.31	0.00	9.97	18.74	0.00	3.29	0.64	0.00	9.05	0.00	0.56	93.56	25	GLM
51.34	0.00	7.96	21.14	0.00	3.24	0.19	0.00	8.98	0.00	0.00	92.85	26	GGC
50.01	0.00	8.07	20.99	0.00	3.09	0.37	0.00	8.89	0.00	0.36	91.78	27	GGM
51.26	0.00	8.50	20.62	0.00	3.38	0.52	0.00	9.30	0.00	0.31	93.89	28	GGM
51.10	0.00	9.94	19.39	0.00	3.24	0.49	0.00	9.10	0.00	0.38	93.64	29	GBM
51.29	0.00	8.85	19.76	0.00	3.41	0.00	0.00	9.21	0.00	0.26	92.78	30	GBC
51.19	0.00	9.33	19.84	0.00	3.46	0.20	0.29	9.36	0.00	0.31	93.98	31	GGM
50.27	0.00	10.57	17.81	0.00	2.95	2.08	0.00	8.21	0.26	1.40	93.55	32	GLC
52.67	0.00	12.89	16.02	0.00	3.11	0.63	0.36	8.53	0.00	0.34	94.55	33	GLM
51.79	0.00	11.40	16.69	0.00	3.41	0.71	0.34	8.89	0.00	0.61	93.84	34	GBM
51.64	0.00	7.89	20.78	0.00	3.39	0.19	0.00	9.01	0.00	0.36	93.26	35	GGC
48.70	0.00	10.63	17.76	0.00	3.64	1.71	0.00	8.56	0.00	0.38	91.38	36	GGM
50.18	0.00	7.85	21.19	0.00	3.16	0.44	0.00	8.80	0.00	0.62	92.24	37	GGM
50.11	0.00	9.80	19.14	0.00	3.00	0.99	0.00	8.61	0.00	0.80	92.45	38	GGM
49.00	0.00	9.84	18.64	0.00	2.88	2.44	0.00	8.72	0.21	1.96	93.69	39	GBM
48.91	0.00	10.69	19.47	0.00	2.24	0.19	0.34	8.59	0.00	0.33	90.76	40	GGC
49.72	0.00	8.40	22.31	0.00	2.79	0.50	0.34	8.82	0.22	0.37	93.47	41	GGM

Aluminum: Microprobe analysis of the glauconite grains yielded a mean value of 8.9% Al_2O_3 in grass-green pellets, with about 1% increase in the margins. The light-green pellets gave a mean value of 9.73% Al_2O_3 at the margins and 2.03% in the core. The mean value of Al_2O_3 content in the brownish grains is 12.35%, with about 3.1% differences between the inner core (mean 9.25%) and the exterior cortex (mean 13.91%).

The inverse relationship between FeO and Al_2O_3 (Fig. 4) is apparent for both light and grass-green pellets, but unclear for the brownish-yellow grains.

Silicon: There are little differences in SiO_2 content in the three types of glauconite grains. The mean value is 51.06% SiO_2 in the grass-green pellets. It is 52% and 51.77% in the light-green and brownish-yellow glauconite pellets respectively.

Magnesium: The miroprobe analysis showed slight difference of MgO content in the three types of glauconite pellets. The mean values in the grass-green, the brownish-yellow grains and the light-green pellets are 3.62%, 3.68% and 3.93% respectively.

DISCUSSION AND CONCLUSION

From the microprobe analysis (Tables 1 and 2), the following observations are made;

- The Al content is higher in the brownish-yellow grains than in the grass-green and is intermediate in the light-green pellets.
- The K content is slightly higher in the grass-green pellets than in the brownish-yellow pellets.

Table 2. Formula on Basis of Si + Al + Ti + Fe + Mn + Ca = 12, O = 22

Si	Al_{IV}	Al_{VI}	Fe_3	Fe_2	Mn	Mg	Ca	Na	K	S	P	Spot	Notes
7.44	0.56	1.22	1.79	0.07	0.00	0.93	0.03	0.00	1.50	0.00	0.00	1	GGC
7.41	0.59	1.11	1.87	0.00	0.00	1.02	0.03	0.11	1.44	0.00	0.00	2	GGM
7.40	0.60	1.43	1.56	0.22	0.00	0.78	0.07	0.00	1.46	0.00	0.00	3	GBM
7.40	0.60	1.86	1.32	0.03	0.00	0.79	0.04	0.00	1.36	0.00	0.00	4	GBC
7.41	0.59	1.93	1.16	0.13	0.00	0.78	0.07	0.00	1.36	0.00	0.00	5	GBM
7.50	0.51	1.11	1.76	0.16	0.00	0.97	0.05	0.09	1.45	0.00	0.00	6	GLC
7.37	0.63	0.98	1.97	0.12	0.00	0.93	0.04	0.08	1.53	0.00	0.00	7	GLM
7.36	0.64	0.85	2.14	0.18	0.00	0.83	0.03	0.00	1.6	0.00	0.00	8	GGC
7.26	0.74	0.93	2.07	0.18	0.00	0.82	0.00	0.13	1.62	0.00	0.00	9	GGC
7.51	0.50	1.33	1.67	0.10	0.00	0.90	0.04	0.00	1.43	0.00	0.00	10	GGC
7.44	0.56	1.10	1.75	0.25	0.00	0.90	0.04	0.00	1.48	0.00	0.03	11	GGM
7.45	0.55	1.36	1.46	0.39	0.00	0.80	0.05	0.00	1.50	0.00	0.03	12	GBC
7.42	0.59	1.42	1.22	0.57	0.00	0.79	0.06	0.00	1.49	0.02	0.04	13	GBM
7.37	0.63	1.28	1.44	0.45	0.00	0.83	0.04	0.00	1.53	0.02	0.03	14	GLC
7.45	0.55	1.11	1.63	0.38	0.00	0.88	0.04	0.00	1.60	0.00	0.03	15	GLM
7.26	0.74	1.34	0.00	1.74	0.00	0.92	0.37	0.00	1.43	0.02	0.23	16	GBM
7.33	0.67	1.34	1.57	0.24	0.00	0.85	0.03	0.00	1.47	0.00	0.05	17	GLM
7.37	0.63	1.33	1.32	0.59	0.00	0.76	0.07	0.00	1.52	0.02	0.04	18	GLM
7.31	0.69	0.73	2.06	0.46	0.00	0.76	0.03	0.11	1.74	0.00	0.00	19	GGC
7.50	0.51	1.61	1.16	0.32	0.00	0.91	0.05	0.00	1.27	0.03	0.04	20	GLC
7.42	0.58	1.52	1.25	0.29	0.00	0.94	0.08	0.00	1.33	0.03	0.03	21	GLM
7.48	0.52	0.97	1.82	0.27	0.00	0.94	0.00	0.00	1.52	0.00	0.04	22	GGC
7.51	0.49	0.99	1.61	0.51	0.00	0.90	0.04	0.00	1.54	0.02	0.03	23	GGM
7.46	0.54	0.94	1.47	0.82	0.00	0.77	0.08	0.07	1.68	0.00	0.04	24	GLC
7.36	0.64	1.05	1.40	0.85	0.00	0.70	0.10	0.00	1.66	0.00	0.07	25	GLM
7.40	0.60	0.76	2.13	0.42	0.00	0.70	0.03	0.00	1.65	0.00	0.00	26	GGC
7.35	0.65	0.74	1.90	0.68	0.00	0.68	0.06	0.00	1.67	0.00	0.05	27	GGM
7.36	0.64	0.80	1.79	0.69	0.00	0.72	0.08	0.00	1.70	0.00	0.04	28	GGM
7.31	0.69	0.99	1.66	0.66	0.00	0.69	0.08	0.00	1.66	0.00	0.05	29	GBM
7.39	0.61	0.89	1.88	0.51	0.00	0.73	0.00	0.00	1.69	0.00	0.03	30	GGC
7.32	0.68	0.89	1.76	0.62	0.00	0.74	0.03	0.08	1.71	0.00	0.04	31	GGM
7.36	0.65	1.18	0.25	1.93	0.00	0.64	0.33	0.00	1.53	0.03	0.17	32	GLC
7.36	0.64	1.48	1.15	0.72	0.00	0.65	0.09	0.09	1.52	0.00	0.04	33	GLM
7.38	0.63	1.29	1.04	0.95	0.00	0.72	0.11	0.09	1.62	0.00	0.07	34	GBM
7.43	0.57	0.77	1.86	0.64	0.00	0.73	0.03	0.00	1.65	0.00	0.04	35	GGC
7.17	0.83	1.02	1.43	0.76	0.00	0.80	0.27	0.00	1.61	0.00	0.05	36	GGM
7.36	0.64	0.71	1.76	0.83	0.00	0.69	0.07	0.00	1.65	0.00	0.08	37	GGM
7.32	0.68	1.01	1.26	1.08	0.00	0.65	0.16	0.00	1.61	0.00	0.10	38	GGM
7.31	0.69	1.04	0.00	2.32	0.00	0.64	0.39	0.00	1.66	0.02	0.25	39	GBM
7.23	0.77	1.10	1.68	0.73	0.00	0.49	0.03	0.10	1.62	0.00	0.04	40	GGC
7.24	0.76	0.68	1.82	0.89	0.00	0.61	0.08	0.10	1.64	0.02	0.05	41	GGM

Fe_3 value is much higher in the grass-green than in both light-green and brownish-yellow pellets.

The Electron Microprobe analysis leads to the conclusion that the brownish-yellow pellets were grass-green pellets (glauconite mineral), but the $Fe3^+$ were possibly replaced by Al_{VI} (aluminum octahedral). The Fe^{2+} and K were also replaced by Al_{VI}. As a result the grass-green pellets were changed to brownish-yellow pellets. These commonly brownish glauctonite grains, reflect a history of more oxidizing conditions, either through subaerial exposure or transport in shallow turbulent waters during Upper Cenomanian-Lower Turonian low sea-level stands (Giresse and Odi, 1973). The light-green grains were the transition stage between the grass-green and brownish yellow pellets (i.e. brownish yellow and light-green glauconite pellets were formerly all grass-green pellets). The roundness and size of the glauconite pellets found in the outer ramp are incompatible with their setting and strongly suggest that they were transported, and their replacement by late dolomitization (Fig. 5 and 6) suggest that they were transported early.

The glauconite is a valuable marine indicator and it occurs most commonly in relatively shallow water between 60 and 500 m, forming up to 90% of the sediment of the formation. The abundance of glauconite pellets in the base of the Lidam Formation and in the top of the Bahi Formation (both shallow marine deposits), is probably related to the availability of iron from the alteration of the abundant micaceous minerals. These glauconite grains are likely true faecal pellets produced in a large quantity by filter-feeding organisms, and are,

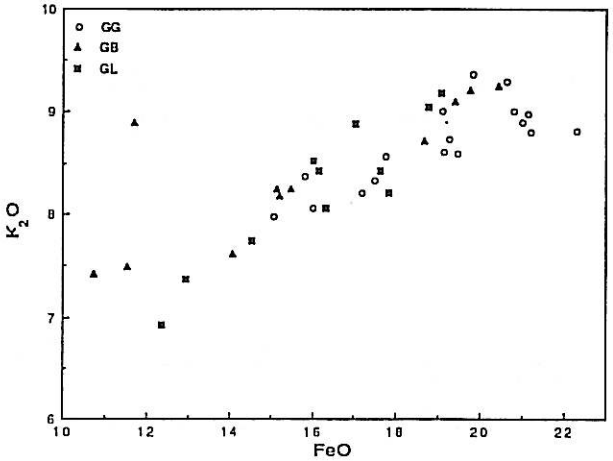


FIG. 3. Relationship between K_2O and FeO for grass-green grains (GG), brownish yellow grains (GB) and light-green grains (GL).

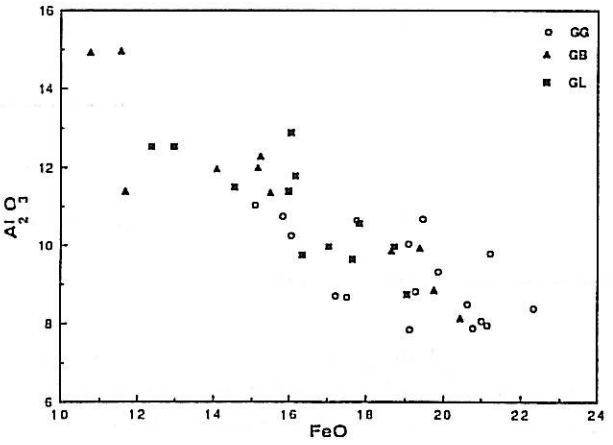


FIG. 4. Relationship between Al_2O_3 and FeO for the same grains in (Fig. 3).



FIG. 5. Microphotograph (SEM) showing the replacement of glauconite pellets by late dolomite.

therefore, essential characteristic of the inner part of the continental shelf (Pryor, 1975). The glauconite within fossils suggests that it developed early and may have been associated with the dissolution of aragonite (Pedley and Bennet, 1985).

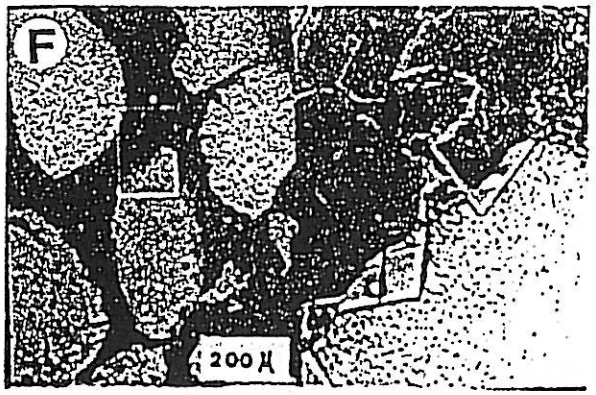


FIG. 6. Microphotograph (SEM) showing the beginning of replacement of glauconite pellets by dolomite.

ACKNOWLEDGEMENT

I would like to express my thanks to the management of the Petroleum Reseach Centre. Special thanks to Mr. M. Idris, the Secretary of People's Committee of the PRC for permission to publish this work. I am grateful to Mr. F. Wilkinson from the Geology Department, Hull University, for his help with microprobe uses. I would like to extend my thanks to my friends and collegues in the PRC. My thanks are also due to Waha Oil Company of Libya, in particular Mr. R. Abu Rawi, the Exploration Manager and the technical staff for providing the core samples used in this study.

REFERENCES

Adams, A.E., Mackenzie, W.S. and Guilford, C., 1984, Atlas of Sedimentary Rocks Under the Microscope: Halsted Press, John Wiley and Sons Inc., U.S.A., 104 p.

Baily, R.J. and Atherton, M.P., 1969, The Petrology of a Glauconite Sandy Chalk. J. Sed. Petr., 39(4), 1420–1431.

Barr, F.T. and Weegar, A.A., 1972, Stratigraphic Nomenclature of the Sirt Basin, Libya. Petr. Expl. Soc. Libya, 179 p.

Bernhold, B.D., and Giresse, P., 1985, Glauconite Sediments on the Continental Shelf of Vancouver Island, British Columbia, Canada, J. Wed. Petr., 55(5), 653–664.

El-Bakai, M.T., 1989, Sedimentology of the Lidam Formation in Northwest Sirte Basin, Libya, Unpubl., M.Sc. Thesis, Univ. of Hull, England, 172 p.

Giresse, P. and Odin, G.S., 1873, Nature Mineralogique et Origine des Glauconites du Plareau Continental du Gabon et du Congo: Sedimentology, 20, 457–488.

Hammuda, O.S., Sbeta, A.M., Mouzoughi, A.J. and Eliagoubi, B.A., 1985, Nomenclature of the Northwestern Offshore of Libya: The Earth Scie. Soc. of Libya Publ., 166 p.

Odin, G.S. and Morton, A.C., 1988, Authigenic Green Particles from Marine Enviroments. In: G.C. Chilingarian and K.H. Wolf (Editor), Development in Sedimentology, Diagenesis II, Vol. 43, 213–264.

Pedley, H.M. and Bennet, S.M., 1985, Phosphorites, Hadgrounds and Sydepositional Solution Subsidence, A Palaeoenvironment Model from the Miocene of the Maltese Islands. Sed. Geol., 45, 1–34.

Pryor, W.A., 1975, Biogenetic Sedimentation and Alteration of Argillaceous Sediments in Shallow Marine Environments: Geol. Soc. Am. Bull., 86, 1244–1254.

PRJ, Vol. 5 (January 1993); P. 62–66, 6 FIGS, 3 TABLES.

KINETICS OF FORMATION OF EPICHLOROHYDRIN FROM ALLYL CHLORIDE BY HYDROGEN PEROXIDE USING SODIUM MOLYBDATE AS CATALYST

I. Ahmad* and A.R. Labib*

حركية الحصول على الأبيكلورهيدرين من الأليل كلوريد مع ما فوق أوكسيد الهيدروجين باستعمال موليبدات الصوديوم كعامل حفاز

إفتخار أحمد و عبدالرزاق اللبيب

لقد تمت دراسة حركية وسبل الحصول على الأبيكلورهيدرين من الأليل كلوريد مع ما فوق أوكسيد الهيدروجين بوجود موليبدات الصوديوم كعامل حفاز، وكانت معادلة التفاعل من الدرجة الأولى بالنسبة للأليل كلوريد وكذلك بالنسبة لموليبدات الصوديوم، وكانت من الدرجة صفر بالنسبة لما فوق أوكسيد الهيدروجين.

كما تمت دراسة تأثير تركيز أيون الهيدروجين على سرعة التفاعل. وتم تحديد طاقة التنشيط واقتراح طريقة التفاعل.

ABSTRACT

The kinetics and mechanism of formation of epichlorohydrin from allyl chloride by hydrogen peroxide in the presence of sodium molybdate as catalyst have been studied. The reaction is first order with respect to oth allyl chloride and sodium molybdate but zero order with respect to hydrogen peroxide. The effect of pH on the reaction rate is also studied. The energy of activation has been determined. A reaction mechanism has also been proposed.

INTRODUCTION

Epichlorohydrin is an important petrochemical which is a base material in the manufacture of epoxy resins. Epoxy resins have become firmly well established in countless applications and techniques. They are used as adhesives, coating and flooring materials. They have applications in paint and varnish industries. The other major use for epichlorohydrin is in the manufacture of synthetic glycerin. Minor applications include its use in epichlorohydrin based rubber, wet strength resins for paper industry, ion exchange resins, surface active agents, inks, dyes, asphalt improvers, corrosion inhibitors, antistats, textile additives and bioproducts. Currently, epichlorohydrin is produced [1] by the chlorohydrination of allyl chloride, derived by chlorination of propylene but the yield is limited to 60–65%.

Many papers and patents have been devoted to the epoxidation of olefins with hydrogen peroxide in the presence of some oxy-compounds of metals such as W, Mo, V, Os, Ti, Zr, Th, Nb, Ta, Cr, Ru and Se [2–5]. The present paper deals with the manufacture of epichlorohydrin from allyl chloride by using hydrogen peroxide as an epoxidising agent in the presence of sodium molybdate as catalyst.

*Petroleum Research Centre, P.O. Box 6431, Tripoli, G.S.P.L.A.J.

EXPERIMENTAL SECTION

All the chemicals used were of analytical (B.D.H.) grade. The concentration of hydrogen peroxide in kinetic runs was measured colorimetrically as described elsewhere [6]. 0.1 M sodium hydroxide solution prepared in isopropanol was used to maintain the required pH of the medium. Measured quantities of allyl chloride, sodium molybdate, sodium hydroxide solution (to maintain required pH) and solvent (50:50 v/v mixture of water and isopropanol) were taken in a stoppered round bottom flask and placed

in thermostated water bath at 50±0.1°C unless mentioned otherwise. After the reactants had reached thermostated temperature, the reaction was started by addition of temperature equilibrated hydrogen peroxide. The kinetics were followed by examining 5 ml aliquots of the reaction mixture for hydrogen peroxide content. The aliquots were added to 5 ml of titanium sulphate solution to stop the reaction. Optical density was measured at 420 nm, and the concentration of hydrogen peroxide was read from the calibration graph.

The presence of epichlorohydrin as a reaction product was confirmed by using Chrompack Packard Gas Chromatograph (model 439) equipped with flame ionisation detector. The column used was 10 m long packed with WCOT fused silica and cp-sil-5CB. Nitrogen was used as a carrier gas.

RESULTS AND DISCUSSION

The progress of the reaction was observed by measuring the disappearance of hydrogen peroxide in the presence of high concentration of allyl chloride. Isolation method is applied for determining the order of reaction. The plot of hydrogen peroxide concentration against time were straight lines (Fig. 1) indicating zero order dependence of rate on hydrogen peroxide concentration. Pseudo-zero-order rate constants were calculated from the slope of these lines and tabulated in Table 1 as k_{obsd}.

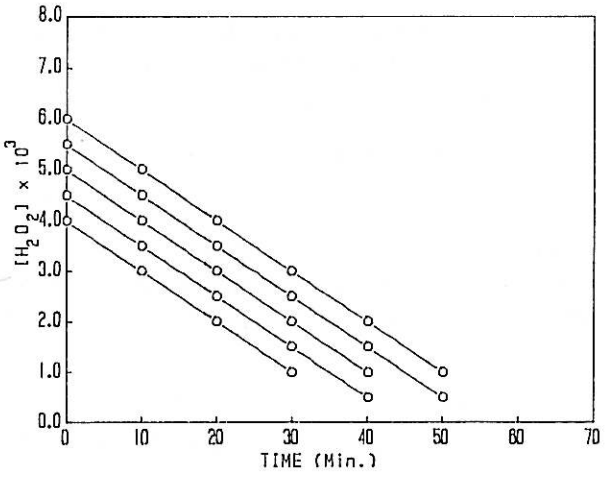


FIG. 1. Pseudo-zero order dependence of rate on hydrogen peroxide concentration.

The order of reaction with respect to catalyst (sodium molybdate) concentration was determined by varying the catalyst concentration and keeping all other variables, such as temperature, pH, concentrations of hydrogen peroxide and allyl chloride constants. k_{obsd} was calculated from the slope of the plots of hydrogen peroxide concentration versus time. The plot of k_{obsd} against the concentration of sodium molybdate was a straight line (Fig. 2) which passes through the origin. This shows first order dependence of rate on catalyst concentration and it also confirms that there is no reaction in the absence of sodium molybdate.

Table 1. Pseudo-Zero-Order Rate for the Oxidation of Allyl Chloride by Hydrogen Peroxide in the Presence of Sodium Molybdate

$[H_2O_2] \times 10^3$ (M)	$k_{obsd} \times 10^6$ (mole dm^{-3} sec^{-1})
4.00	8.14
4.50	8.02
5.00	8.15
5.50	8.23
6.00	8.18

[Allyl chloride] = 20.00×10^{-2} M; [Na_2MoO_4] = 5.00×10^{-4} M; pH, 5.0; Temp. 50°C, solvent, 50% v/v isopropanol.

Similarly the order of reaction with respect to allyl chloride was also determined by varying allyl chloride concentration and keeping all other variables constant.k_{obsd} were calculated from the slope of plots of $[H_2O_2]$ versus tme. k_{obsd} is directly proportional to the concentration of substrate [allyl chloride]. This is indicative of first order dependence of rate on substrate concentration. The results are presented in Table 2.

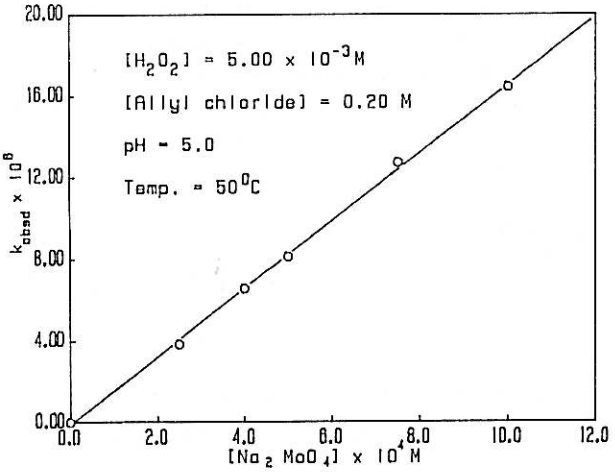


FIG. 2. First order dependence of rate on catalyst concentration.

Preliminary studies have shown that under our experimental conditions, hydrogen peroxide does not change allyl chloride into epichlorohydrin without the presence of catalyst (sodium molybdate) and also the catalyst alone without hydrogen peroxide fails to bring allyl chloride into epichlorohydrin. This suggests the involvement of some oxygenated form of molybdenum in the process as

Table 2. First Order Dependence of Molybdate Catalysed Oxidation Rate of Allyl Chloride on the Concentration of Allyl Chloride

[Allyl chloride] $\times 10^2$ (M)	$k_{obsd} \times 10^5$ (mole dm^{-3} sec^{-1})	$\frac{k_{obsd}}{[\text{Allyl chloride}]} \times 10^3$
10.00	0.81	0.270
20.00	1.21	0.269
30.00	1.63	0.272
40.00	2.03	0.271
50.00	2.41	0.268

$[H_2O_2] = 5.00 \times 10^{-3}$ M; $[Na_2MoO_4] = 5.00 \times 10^{-4}$ M; pH, 5.0, Temp., 50°C; Solvent 50% v/v isopropanol.

oxygen carrier. In aqueous solution molybdate ions hydrolyse into the acid anions as in eqn. (1) and (2):

$$Mo_4^{2-} + H^+ \rightleftharpoons HMo_4^- \quad (1)$$

$$HMo_4^- + H^+ \rightleftharpoons H_2MoO_4 \quad (2)$$

It may be recalled that molybdic acid is converted to peroxymolybdic acid [7, 8] when treated with aqueous hydrogen peroxide which suggests that hydrogen peroxide rapidly and completely oxidise acid anions to peroxyacid anions as in eqn. (3):

$$HMoO_4^- + H_2O_2 \rightarrow HMoO_5^- + H_2O \quad (3)$$

It is presumed here that in the system under investigation peroxymolybdate anion ($HMoO_5^-$) is the epoxidising species and in rate-controlling step it reacts with allyl chloride giving epichlorohydrin and regenerating molybdate anion ($HMoO_4^-$). Molybdate anion is then reconverted into peroxymolybdate anion by hydrogen peroxide. The following indicates the most probable mechanism:

$$CH_2=CH-CH_2Cl + HMoO_5^- \underset{k_4}{\overset{k_3}{\rightleftharpoons}} [\text{intermediate complex}] \quad (4)$$

$$[\text{intermediate complex}] \xrightarrow{k_5} CH_2-\underset{O}{CH}-CH_2Cl + HMoO_4^- \text{ (epichlorohydrin)} \quad (5)$$

Assuming steady-state for the concentration of intermediate complex, the rate of reaction is given by eqn. (6):

$$\text{Rate of reaction} = k_5 [\text{intermediate complex}] \quad (6)$$

Applying steady state approximation for intermediate complex,

$$k_3 [CH_2=CH-CH_2Cl] [HMoO_5^-] - k_4 [\text{intermediate complex}] - k_5 [\text{intermediate complex}] = 0 \quad (7)$$

Thus,

$$[\text{intermediate complex}] = \frac{k_3 [CH_2=CH-CH_2Cl] [HMoO_5^-]}{k_4 + k_5} \quad (8)$$

Substituting eqn. (8) into eqn. (6) gives:

$$\text{Rate of reaction} = \frac{k_3 k_5 [CH_2=CH-CH_2Cl] [HMoO_5^-]}{k_4 + k_5} \quad (9)$$

Or

$$\text{Rate of reaction} = k [CH_2=CH-CH_2Cl] [HMoO_5^-] \quad (10)$$

where, $k = \frac{k_3 k_5}{k_4 + k_5}$

For each experimental set, the pH and catalyst concentration were constant. Then eqn. (10) in terms of catalyst concentration is:

$$\text{Rate of reaction} = k' [CH_2=CH-CH_2Cl] [Na_2MoO_4] \quad (11)$$

As discussed in the previous section, the progress of the reaction was observed by measuring the disappearance of hydrogen peroxide, which is represented by the following:

$$\text{Rate of reaction} = k' [CH_2=CH-CH_2Cl] [Na_2MoO_4] \quad (12)$$

or,

$$\text{Rate of reaction} = k_{obsd} \quad (13)$$

where,

$$k_{obsd} = k' [CH_2=CH-CH_2Cl] [Na_2MoO_4] \quad (14)$$

Eqn. (12) explains the observed order of reaction with respect to allyl chloride, catalyst (Na_2MoO_4) and hydrogen peroxide.

It has been reported [9] earlier that the formation of $HMoO_4^-$ is maximum around pH 3.6. The rates of reaction catalysed by molybdate increase with increasing pH and are maximum at the pH at which $HMoO_4^-$ formation is maximum and thereafter the rates decrease with further increase in pH (Fig. 3). This clearly suggests that peroxymolybdic acid anion is the epoxidizing agent. At this stage it looks instructive to argue why negative charged peroxymolybdate anion and not the unionised peroxymolybdate acid attacks the double bond of the allyl chloride.

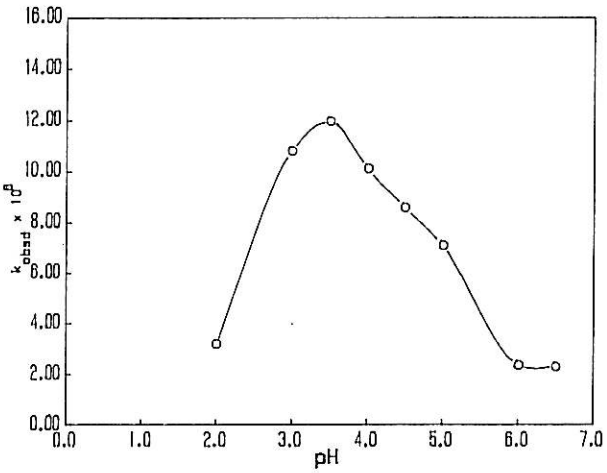


FIG. 3. Dependence of rate on pH of the medium.

In view of the intramolecular hydrogen bond in the epoxidation of olefins by organic peracids [10, 11] and the fact that molybdate has the maximum catalytic activity at a pH where concentrations of the peroxymolybdic acid anion species ($HMoO_5^-$) is maximum. It is proposed that peroxymolybdic acid anion (I) in Fig. 4 is in equilibrium with hydrogen bonded cyclic structure (II) which due to partial positive charge on the peroxy oxygen acts like an electrophile. The proposed transition state of the reaction is shown in Fig. 5.

The reaction was studied at six different temperatures ranging from 35 to 60°C, and the results are given in Table 3. The plots of log k_{obsd} against reciprocal of temperature (1/T) gave a straight line (Fig. 6).

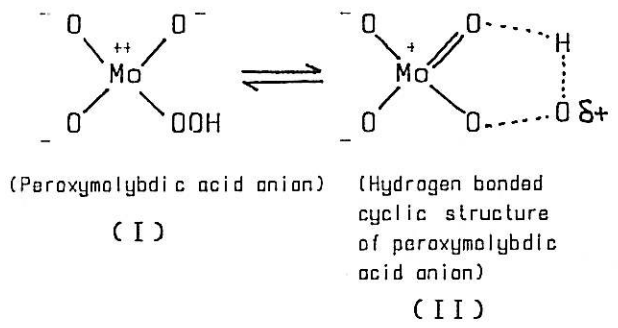


FIG. 4. Cyclic structure of peroxymolybdic acid.

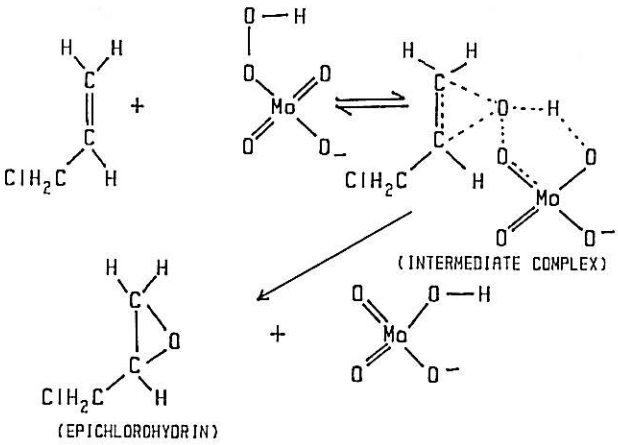


FIG. 5. Mechanism of the reaction.

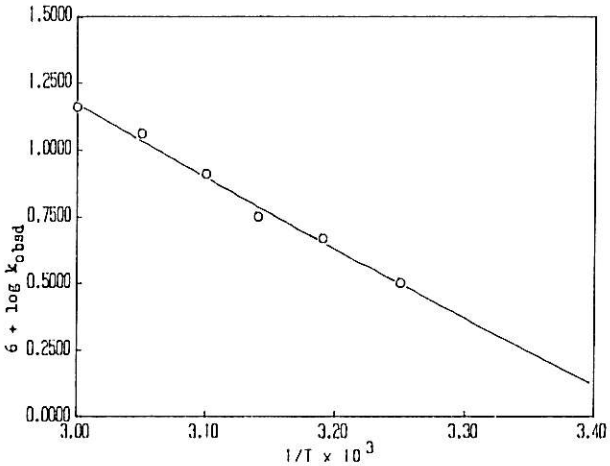


FIG. 6. Dependence of rate on variation of temperature.

Table 3. Effect of Temperature on the Formation of Epichlorohydrin Rate

Temperature (K)	$\frac{1}{T} \times 10^3$	$k_{obsd} \times 10^6$ (mol dm^{-3} sec^{-1})	$6 + \log k_{obsd}$
308	3.25	3.16	0.4997
313	3.19	4.68	0.6702
318	3.14	5.62	0.7497
323	3.10	8.14	0.9106
328	3.05	11.48	1.0599
333	3.00	14.45	1.1599

$[H_2O_2] = 5.00 \times 10^{-3}$ M; $[Na_2MoO_4] = 5.00 \times 10^{-4}$ M; pH, 5.0 [Allyl Chloride] = 0.20 M; Solvent, 50% v/v isopropanol.

The energy of activation was calculated from the slope of this plot to be 51.06 kJ ml^{-1}.

ACKNOWLEDGEMENT

The authors are grateful to the Management of Petroleum Research Centre for providing facilities and encouragement.

REFERENCES

[1] Lowenheim, F.A., and Moran, M.K., 1975, Industral Chemicals, 4th ed., John Wiley and Sons, p. 335.
[2] Ahmad, I., and Degam, M., 1992, Petrol. Res. J., Vol. 4, 52–55.
[3] Ahmad, I., Degam, M., and Labib, A., 1991, Petrol. Res. J., Vol. 4, 53–56.
[4] Allan, G.G., and Neogi, A.N., 1970, J. Catal., **19**, 256.
[5] Mugdan, M., and Young, D.P., 1949, J. Chem. Soc., 2988.
[6] Reichert, J.S., and McNeight, S.A., and Rudel, H.W., 1939, Ind. Eng. Chem., Anal. ed., **11**, 194.
[7] Remy, H., 1956, in Treatise in Inorganic Chemistry, Elsevier, Amsterdam, Vol. II, p. 100.
[8] Sidgwick, N.V., 1950, in The Chemical Elements and Their Compounds, Oxford Univ. Press, London, Vol. 2, p. 1045.
[9] Beg, M.A., and Ahmad, I., 1975, J. Catal., **39**, 260.
[10] Swern, D., 1957, Organic Reactions, **7**, 378.
[11] Skell, P., and Garner, A., 1956, J. Amer. Chem. Soc., **78**, 5430.

PRJ, Vol. 5 (January 1993); P. 67–75, 5 FIGS, 6 TABLES.

SYNTHESIS AND STUDY OF DIFFERENT THIOAMIDES AS CORROSION INHIBITORS

M.A. Khawaja*, S.R. Abu Oun*, M.A. Shariff*

تخليق ودراسة مواد تياميدية مختلفة لإستعمالها كمانعة للتآكل

م. خواجة، سالم أبوعون، محمود الشريف

لكثير من المركبات العضوية ذرات تركيبية غنية بالألكترونات، مثال النيتروجين والكبريت، وهي تستعمل بكثرة كمواد مخففة للإحتكاك في الصناعات النفطية وذلك للتقليل من ظاهرة التآكل. ويزيد وجودالذرات الغنية بالألكترونات بجزئيات المركبات تحت الدراسة في رفع قدرتها على تكوين روابط تشاركية متناسقة مع ذرات الفلز ذات العلاقة ببيئة التآكل.

والمركبات المبنية على الأمين الدهني والأمين العطري والإيمادازول والديميدازول والأميد الدهني مواد واسعة الإنتشار كموانع للتآكل في مجال النفط.

وقد تمت في الدراسة تخليق بعض الفينالمسيتياميدات والبنزسيتاميدات. كما وصفت المعلومات الكيميائية والفيزيائية. وقيست معاملات الذوبان والثبات البارد والثبات الساخن وخصائص منع التآكل للمركبات المخلقة تحت ظروف صناعية (10 % خام في ملوحة صناعية عند معامل PH بين 4.5 و74.8، كما تمت مقارنة خصائص مقارنة التآكل ببعض التيميدات المخلقة في تركيزات مختلفة من الملوحة المرتفعة ومياه البحر). وتختلف التميدات المعدة في وزنها الجزئي وذلك لوجود بعض المكونات العضوية المختلفة على مجموعة التيوميدات. وقد بنيت عملية تخليق المركبات المذكورة على تفاعل ولجرودت — كندلر.

وتم التأكد من عملية تخليق المركبات بواسطة العديد من طرق التحليل المعتادة. وقد قورنت القيم التجريبية للتكوين العنصري لهذه المركبات مع القيم المحسوبة ووجدت متناسقة. كما وجد أن قمم منحنيات الإمتصاص المقاس مطيافياً تؤكد وجود مجموعة التيوميد بالمركبات المعدة.

وقد نوقشت في هذه الدراسة ميكانيكية التفاعل المحتملة لتخليق المركبات المذكورة أعلاه، كما تم تفسير ميكانيكية وسبل منع هذه المركبات للتآكل.

ABSTRACT

Many organic compounds having electron rich atoms in their structure, such as nitrogen, and sulphur, are widely in use as lubricating additives in the oil industry to minimise corrosion. The presence of electron rich atoms in the molecules of compounds under discussion, increases the ability of these substances to form co-ordinate covalent bonds with the metal atoms, involved in the corrosion environment.

Compounds based on fatty amine, aromatic amine, imidazoline, di-imidazoline and fatty amide are widely used as corrosion inhibitors. Less attention has been given to study thiocarboxylic acid amides as corrosion inhibitors, in the oil field.

In this work some phenylacetothioamide and benzyl-acetothioamide are synthesised. The chemical and physical data of the prepared compounds are compiled. The solubility, cold stability, heat stability and corrosion inhibition characteristics, of the synthesised compounds have been measured in the artificial environment (10% crude in artificial brine at the pH in between 4.5 to 4.8). Anticorrosive properties for few of the amine based commercially available oilfield corrosion inhibitors and few of the above mentioned synthesised compounds are measured, in the test environment, in order to compare their activity. Prepared thioamides differ in their molecular weights, due to presence of different organic substituents, on the thioamide group. Synthesis of the above mentioned compounds are based on the Willgerodt-Kindler reaction.

*Petroleum Research Centre, P.O. Box 6431, Tripoli, G.S.P.L.A.J.

The synthesised compounds are confirmed by IR, UV/Vis, Elemental Analyzer and other traditional analytical techniques. The experimental values of the elemental composition of these compounds were compared with the calculated values and found to be in agreement. UV/Vis and IR spectras also show the absorption peaks, which confirm the presence of thioamide group in the prepared compounds. The possible reaction mechanism regarding the synthesis of the above mentioned compounds is discussed. Mechanism of corrosion inhibition of these compounds in the corrosive environment is explained.

INTRODUCTION

Chemical antidegradants refer to the chemical species which inhibit corrosion of metals and stabilise or adjust the environment in which it has been applied. Corrosion inhibitors form a protective barrier on the surface of a substrate by physical absorption, chemical absorption or reaction with the substrate. Corrosion problems in the operation of petroleum drilling installation are to be solved by the aid of corrosion inhibitors in the injection water. The crude comes out with plenty of minerals containing water. The pH of this aqueous and oily mixture varies but lies on the acidic side. This acidic pH, mineral contents and dissolved gases are responsible for metallic corrosion.

Variety of organic compounds having electron rich atoms in their molecules such as nitrogen and sulphur, are widely used as corrosion inhibitor, because of their anticorrosive and antioxidation properties [1–3]. A large number of these compounds have been synthesised in the Petroleum Research Centre. They showed different percentage composition of nitrogen and sulphur and varying in unsaturations. It has been proved experimentally that higher the molecular weight of the above mentioned types of compounds, higher is the anticorrosive and antioxidation properties. It may be due to more surface area of the molecules. It is also established that the sulphur containing substances are more effective anticorrosive and antioxidative compared to nitrogen containing compounds, provided the molecular weight and molecuar unsaturations are the same [2–3].

Corrosion and oxidation inhibitors are routinely used in oil fields and in the refineries, in order to minimise the corrosion of the oil transporting pipe lines, pumps, valves and other involved equipments and also the refinery installations.

Commercial corrosion inhibitors are unique mixtures that may contain surfactants, film enhancers, demulsifiers, or an oxygen scavenger in addition to inhibitor moiety.

The purpose of this work was to synthesise some sulphur containing organic compounds which are higher in boiling point, rich in electron density and higher molecular weight (such as compounds of thioamide series). Synthesised thioamides were supposed to be evaluated regarding their anticorrosive properties in the artificial corrosive environment, similar to the formation water, in order to locate the suitable compounds which can compete with the preparations already available in the market for such purpose.

PREPARATION

The synthesis of thioamides are based on the Willgerodt Reaction [4–9]. The reaction is carried out by adding suitable amine in the mixture of sulphur and suitable ketone, in equimolar proportion. Thioamides result in the reaction of enamine with sulphur at 20°C. Enamine is generated at elevated temperature by the reaction of ketone and amine. The following is the general reaction model:

$$\underset{\text{Ketone}}{\mathrm{ArCOCH_2.R}} + \underset{\text{Amine}}{\mathrm{HNR_1R_2}} \xrightleftharpoons{130^\circ C} \underset{\text{Enamine 1}}{\mathrm{ArC(NR_1R_2)=CH.R}}$$

Where R = H or organic group
R_1 = H or organic group
R_2 = H or organic group

Then reaction of elemental sulphur with enamine results the isomerisation and thiolysis. This reaction is very fast and takes place favourably even at 20°C, as shown below:

$$\mathrm{Ar-\underset{\displaystyle NR_1R_2}{\underset{|}{C}}=CH.R} \xrightleftharpoons[S_8/20^\circ C]{\text{Isomerisation}} \mathrm{ArCH_2\underset{\displaystyle NR_1R_2}{\underset{|}{C}}=CH_2} \xrightleftharpoons[20^\circ C]{S_8} \mathrm{[ArCH_2\underset{\displaystyle NR_1R_2}{\underset{|}{C}}=CHSH]}$$

$$\xrightarrow[\text{stabilisation}]{\text{Irreversible}} \mathrm{[ArCH_2-\underset{\displaystyle N^+R_1R_2}{\underset{\backslash}{CH}}-\overset{\displaystyle H}{\overset{|}{C}}-S- \longrightarrow ArCH_2-CH_2-\underset{\displaystyle NR_1R_2}{\underset{|}{C}}=S}$$

EXPERIMENTAL PROCEDURE

A 0.2 Mole of amine was added to a mixture of 0.2 mole of ketone and 0.2 mole of sulphur at ambient temperature (21–24°C) in a heat resistant reaction flask. The flask was immediately connected with reflux condenser. The temperature of the flask was then gradually raised to 95–100°C, by controlled heating. The reaction mass was kept at this temperature with constant stirring for 4–5 hours. After elapsing the reaction time, the flask was allowed to cool. The reaction mass was dissolved in xylene in order to remove any unreacted sulphur. After evaporation of xylene the crystalline products were purified by recrystallisation in ethanol. The liquid products were not purified due to unavailability of very low vacuum facilities for complete removal of benzene. So crystalline products in purified form and liquid products in crude form were used for evaluation of anticorrosive properties of the synthesised compounds to screen out the effective compounds. The melting point of the crystalline products were measured and are mentioned in Table 1. The boiling point of the crude liquid products were not measured as the compounds contain xylene. The purification of these compounds will be done after the availability of the required vacuum facilities. The yield of crystalline products were calculated and given in Table 1. The yield of liquid products were not estimated due to impureness of the compounds.

Table 1. Experimental Yield of Crystalline Products

Compound code	m.p. in °C	Percent yield
iii	122–123	8.1
xii	96–97	47.3
xxi	129–130	59.4
xxii	74–75	85.3
xxiv	77–78	82.9

ANALYTICAL CHARACTERISATION OF THIOAMIDES

Study of I.R. Spectra

I.R. absorption bands of thioamides fall in the "Finger print" region of the spectra and are difficult to trace out normally [1, 10]. Secondly the vibrations of the $-CSN=$ group are not clearly seen due to strong coupling with other vibrations of the molecules. Strong absorption bands were found in the I.R. Spectra of the synthesised compounds. They were in the region of 700–850 cm^{-1}, 700–800 cm^{-1}, and in the region of 850–1000 cm^{-1}, for the primary, secondary and tertiary thioamides respectively. These bands indicate the presence of $=N-C=S$ (double bond) group in the compound under analysis. The above mentioned regions are the absorption regions of $N=C-S$ (single bond) group also.

Strong absorption bands in the region of 1300–1400 cm^{-1} in case of primary, secondary and tertiary thioamide, in I.R. spectras of the synthesised compounds are due to presence of $C-C$ and $C-N$ (single bond), which are also the absorption region of $C=N$ (double bond).

The above mentioned observation supports the concept of resonance stabilised planar $S-C-N$ skeleton of the thioamide molecules.

$$S-C=N \longleftrightarrow S=C-N$$

The absorption bands in the I.R. spectra of the synthesised compounds, in the region 1200–1300 cm^{-1} in case of primary thioamide, in the region 950–1150 cm^{-1} in case of secondary thioamide and in the region 1000–1200 cm^{-1} in case of tertiary thioamides, indicate the presence of $N-C-S$ group.

Strong absorption bands in the I.R. spectra of the synthesised compounds, in the region 1415–1480 cm^{-1} in case of primary thioamide, in the region 1525–1565 cm^{-1} in case of secondary thioamide and in the region 1490 to 1530 cm^{-1} in case of tertiary thioamide are due to the presence of $C-N$ and NR_2 groups.

The above observations confirm the presence of thioamide group in the synthesised compounds under investigation. I.R. spectra were obtained in KBr pellets by using PU-9512 IR spectrophotometer.

Ultraviolet Spectroscopic Evidence

$C=S$ group of thioamide has chromophoric properties. These compounds are bright yellow and yellowish brown in colour. The majority of their parent substances (ketones and amines) are colourless and few are white crystalline in nature. This interesting fact led to the identification of thioamide by UV/Vis Spectrophotometry. The UV/Vis spectra of the synthesised compounds were obtained, by using Milton Roy-1201 UV Spectrometer, in benzene. The results indicate that the synthesised compounds have characteristic long wavelengths, low intensity (R) band and the more intense (K) bands at shorter wavelength. This is in accordance with the behaviour of thioamides in these regions, as mentioned in the literature [1, 10]. According to Kasha's terminology (R) and (K) bands are due to the n-π^* and π to π^* transition respectively [10]. This classification is based on the MO calculations, polarised U.V. absorption spectra, solvent shifts, intensities and behaviour on protonation. The observed facts are given in Table 2.

Table 2, Ultraviolet and Visible Spectrophotometric Data of Synthesised Compounds

Compound code	λ_{max}(nm)	log ε
i	251.6	4.507
ii	253.6	4.509
iii	253.6	4.509
iv	269.8	4.523
v	253.6	4.510
vi	257.6	4.515
vii	259.7	4.517
viii	251.6	4.505
ix	255.7	4.510
x	256.3	4.504
xi	257.7	4.515
xii	255.6	4.521
xiii	253.6	4.508
xiv	254.6	4.501
xv	255.6	4.511
xvi	251.6	4.506
xvii	257.6	4.513
xviii	256.4	4.503
xix	263.7	4.519
xx	253.6	4.510
xxi	255.3	4.521
xxii	254.4	4.509
xxiii	253.6	4.510
xxiv	253.6	4.510
xxv	261.7	4.519
xxvi	259.6	4.521
xxvii	258.9	4.503
xxviii	259.3	4.513
xxix	267.7	4.522
xxx	253.6	4.509

Solvent used is Benzene.

EVALUATION OF ANTICORROSIVE PROPERTIES OF THE SYNTHESISED COMPOUNDS

Anticorrosive properties are measured by applying the procedure mentioned in the ID 182 using persistent film technique, in order to separate the compounds having more than 50% metal protection properties [11]. The Oil (Sirtika crude) and Brine water (composed of 9.62% NaCl, 0.305% $CaCl_2$, 0.186% $MgCl_2.6H_2O$ and 89.89% distilled water) were used in all the experiments. The Oil brine water ratio was chosen 10:90 (Oil-to-Brine water) and chemical (test compound) concentration based on the total volume of mixture of oil and brine was chosen 1%. Xylene was used as solvent for dissolution of test compounds. Prepolished carbon steel coupons were used throughout the experiment as test metal. The used coupons have available surface area equal to 13.2098×10^{-4} m^2 each. The procedure mentioned in the ASTM Designation G1-88 for preparing, cleaning, and evaluating corrosion test specimens was adopted in this work [12]. The anticorrosive test was carried out at ambient temperature for 72 hours and wheel speed was kept at 6 r.p.m. Table 3 shows the experimental results of test compounds in percentage protection and weight loss of the test coupons.

Anticorrosive properties of few of the mentioned compounds and the compounds commercially available as crude oil corrosion inhibitors in the concentration ranges from 10 to 100 ppm are measured in Brine water as well as in Sea water by using standard NACE Wheel Test method. The test conditions for all the above experiments are given in Table 4. Schematic diagram of the gas purging system and gas blanket assembly, used in the test experiments is illustrated in Fig. 1.

As this study was only limited to screen out the effective anticorrosive compounds from the synthesised products, the additives like surfactants, film enhancer etc. were not incorporated with the test compounds during the evaluation.

RESULTS AND DISCUSSION

Corrosion processes both anodic and cathodic are described in detail in the literature [2–3].

The effect of hydrogen sulphide is thought to be responsible for the acceleration of corrosion of iron. But in the presence of inhibitors such as amines, quaternary ammonium cations, thiourea, synergistic enhancement of inhibition is observed due to interaction of adsorbed HS^- ion with the adsorbed inhibitor.

The mechanism of action of organic corrosion inhibitors, depends on many factors, such as concentration; the pH of the corrosive environment; the nature of the anion of acid; the presence of other species in the corrosive medium; the extent of reaction to form secondary inhibitors and the nature of the metal. The activity of corrosion inhibitors, with the same functional group, may additionally vary with factors such as the effect of the molecular structure, electron density of the functional group and the size of the hydrocarbon portion of the molecule, unsaturations of the molecule and presence of electron rich elements [9].

Corroding metal surfaces in acid solution are oxide free, whereas in neutral solutions, the metal surfaces are covered with films of oxides, hydroxides or salts owing to reduced solubility of these species [9]. Inhibition in neutral solution is due to compounds which can form or stabilise protective surface films. The organic compounds containing sulphur inhibit the corrosion of metals in acid solution perhaps by donation of electrons from adsorbed molecules to the metal atoms or ions.

Sulphur containing compounds are considered to be superior in inhibition compared to nitrogen and oxygen containing compounds, as ionisation energy

Table 3. Effect of Synthesised Compounds on the Corrosion Properties of the Carbon Steel Coupons

Compound code	Percentage protection	Loss of wt. in g/m^2
BLANK	00.00	24.522
TH-i*	90.45	2.342
TH-ii	44.09	13.708
TH-iii*	88.78	2.751
TH-iv	40.73	14.535
TH-v*	58.14	10.264
TH-vi	21.05	19.360
TH-vii*	63.20	9.024
TH-viii*	75.84	5.924
TH-ix*	86.73	3.254
TH-x	21.62	19.220
TH-xi*	80.34	4.822
TH-xii*	87.57	3.048
TH-xiii*	64.04	8.817
TH-xiv	48.86	12.540
TH-xv*	55.90	10.815
TH-xvi	48.31	12.675
TH-xvii	44.66	13.570
TH-xviii	15.46	20.730
TH-xix*	83.88	3.953
TH-xx*	81.43	4.554
TH-xxi*	89.59	2.553
TH-xxii*	87.14	3.154
TH-xxiii	39.32	14.879
TH-xxiv*	89.18	2.653
TH-xxv*	84.69	3.754
TH-xxvi	21.06	19.357
TH-xxvii	13.75	21.150
TH-xxviii	86.33	3.352
TH-xxix*	87.14	3.154

*Compounds having percentage protection more than 50%.

Table 4. Test Conditions Used in All Performed Experiments

Test method	Temp. °C	Time (hrs)	CO_2 solubility at R. Temp. g/l	O_2 solubility at R. Temp. g/l	Crude oil (v/v) %	Brine water (v/v) %	Sea water (v/v) %
Wheel test method	25	72	1.5	0.001	10	90	—
Wheel test method	25	72	1.5	0.001	10	—	90

of sulphur is less than oxygen and nitrogen. These compounds attach themselves at the points which suffer anodic attack preferentially and they form a protective film on the metal by making co-ordinate covalent type of linkage with the metal atoms and by london forces. At anodic points, the inhibitor increases the electron atmosphere and render more difficult the detachment of positive metallic ions.

The inhibition of sulphur compounds is made more effective by introducing cyclic or aromatic group into the compounds. This not only increases the surface area of the molecule, but makes the sulphur more nucleophilic. The other groups which increase the nucleophilicity of the molecule of these compounds, when introduced into its molecules, increase the effectiveness of the compounds, regarding its anticorrosive activity. Shielding effect of organic inhibitors depends on the position of side chain [3]. The molecules having side chain at para position are more effective than the molecules having substitution at ortho and meta positions.

The effect of synthesised thioamides on the corrosion properties of steel coupons is given in Table 3. The test conditions for all the corrosion evaluation experiments are given in Table 4. List of synthesised compounds and their percentage composition of sulphur and nitrogen is given in Table 5. The solubility data of the synthesised thioamides in benzene, xylene,

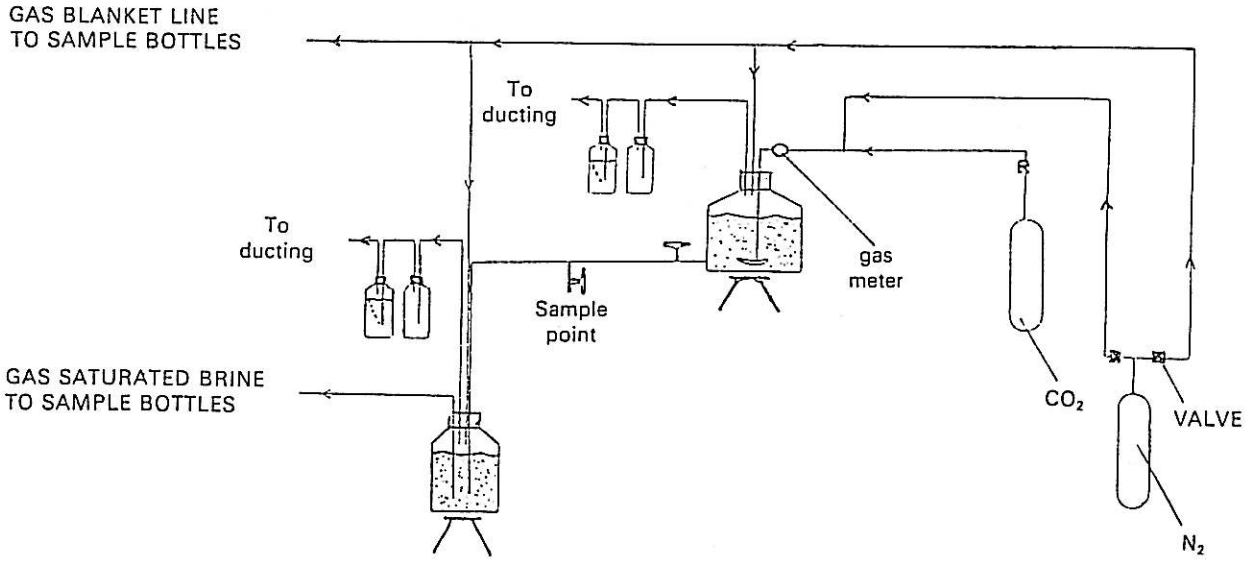


FIG. 1. Schematic diagram of the gas purging system and gas blanketing assembly used in the test experiments.

Table 5. List of the Synthesised Compounds and their Elemental Composition

Compound code	Formula	Percentage composition of S & N w/w			
		Calculated		Found	
		N	S	N	S
TH-i	CaHbNS	2.8	6.4	2.6	6.2
TH-ii	CaHbNS	4.3	9.7	4.1	9.6
TH-iii	CaHbNS	4.3	19.6	4.1	19.4
TH-iv	CaHbNS	4.4	10.1	4.6	10.3
TH-v	CaHbNS	4.4	10.2	4.3	10.1
TH-vi	CaHbNS	4.8	11.0	4.7	10.9
TH-vii	CaHbNS	5.0	11.5	4.9	11.4
TH-viii	CaHbNcS	10.4	11.8	10.5	11.9
TH-ix	CaHbNS	5.3	12.2	5.2	12.1
TH-x	CaHbNS	5.3	12.2	5.2	12.1
TH-xi	CaHbNcS	6.2	10.9	6.1	10.8
TH-xii	CaHbNS	5.5	12.6	5.6	12.7
TH-xiii	CaHbNcSO	7.9	11.1	8.0	11.3
TH-xiv	CaHbNcS	16.7	12.7	16.6	12.6
TH-xv	CaHbNcS	11.2	12.8	11.1	12.6
TH-xvi	CaHbNcSO	11.8	13.4	11.9	13.5
TH-xvii	CaHbNcS	17.7	13.5	17.5	13.4
TH-xviii	CaHbNcS	11.9	13.6	11.7	13.4
TH-xix	CaHbNS	5.9	13.6	5.7	13.4
TH-xx	CaHbNS	6.0	13.7	5.8	13.5
TH-xxi	CaHbNS	6.2	14.1	6.1	14.0
TH-xxii	CaHbNSO	6.3	14.5	6.3	14.4
TH-xxiii	CaHbNS	6.3	14.5	6.2	14.4
TH-xxiv	CaHbNS	6.4	14.6	6.2	14.4
RH-xxv	CaHbNS	6.8	15.4	6.7	15.3
TH-xxvi	CaHbNS	6.8	15.4	6.6	15.2
TH-xxvii	CcHbNS	6.8	15.6	6.7	15.5
TH-xxviii	CaHbNS	7.6	16.9	7.4	16.8
TH-xxix	CaHbNS	7.3	16.8	7.2	16.7

Note: In the above compounds the *a*, *b* and *c* are in the following range:

$a = 11$ to 33
$b = 13$ to 60
$c = 2$ to 3

kerosene, methanol and brine are indicated in Table 6. Heat stability data of these compounds in brine water is given in Table 6.

Schematic diagram of the gas purging system and gas blanketing assembly, used in the test experiments, are illustrated in Fig. 1. Corrosion protection properties versus concentration of inhibitor, of few of the synthesised compounds and some of the commercially available crude oil corrosion inhibitors, in the concentration range 10 to 100 ppm, using NACE Wheel Test method are illustrated in Figs. [2–5] respectively. From the results it appears that synthesised compounds show good inhibition when used in low concentration, but inhibition properties decrease at higher concentration. The increase in corrosion rate at higher concentration, in case of synthesised thioamides, may be due to the presence of effective amount of corrosion supporting organic species along with desired inhibitor molecules, as we have not purified our reaction products. The crude form of synthesised compounds were used in evaluation experiments to screen out the passive compounds. The Comparative studies show that the synthesised compounds are good anticorrosive preparations.

All the evaluation experiments are performed on laboratory scale. The results need reevaluation regarding the behaviour of pure form of synthesised thioamides under high pressure, high temperature, in the presence of CO_2 and H_2S as well as in the above mentioned experimental conditions. This will enable to choose the compounds having linear relationship

Table 6. Solubility and Stability Data of Synthesised Compounds in Common Organic Solvents and in Brine Water

Comp. code	Solubility in					Stability in		
	Benz.	Methanol	Xylene	Keros.	Brine	Cold 20°C	Hot 100°C	Brine
TH-i	+++	+++	+++	+++	− − −	St.	St.	St.
TH-ii	+++	+++	+++	++	− − −	Unst.	Unst.	St.
TH-iii	+++	+++	+++	+++	− − −	St.	St.	St.
TH-iv	+++	+++	+++	+++	− − −	Unst.	Unst.	St.
TH-v	+++	− − −	+++	++	− − −	St.	Unst.	St.
TH-vi	+++	++	+++	+++	− − −	St.	St.	St.
TH-vii	+++	+++	+++	+++	− − −	Unst.	Unst.	St.
TH-viii	+++	++	++	++	− − −	St.	St.	St.
TH-ix	+++	+++	+++	+++	− − −	St.	St.	St.
TH-x	+++	+++	+++	+++	− − −	St.	St.	WPPT
TH-xi	++	+++	++	++	− − −	Unst.	Unst.	St.
TH-xii	+++	+++	+++	+++	− − −	St.	St.	St.
TH-xiii	+++	++	++	− − −	− − −	St.	St.	St.
TH-xiv	++	+++	++	++	− − −	St.	Unst.	PPT
TH-xv	+++	++	++	+++	− − −	St.	Unst.	PPT
TH-xvi	++	++	++	++	− − −	Unst.	Unst.	PPT
TH-xvii	+++	+++	++	++	− − −	St.	St.	St.
TH-xviii	+++	+++	+++	++	− − −	St.	Unst.	St.
TH-xix	+++	+++	+++	+++	− − −	St.	St.	St.
TH-xxi	+++	+++	+	− − −	− − −	St.	St.	St.
TH-xxii	+++	+++	+++	+++	− − −	St.	St.	St.
TH-xxiii	+++	+++	+++	+++	− − −	St.	St.	St.
TH-xxiv	+++	+++	+	++	− − −	St.	St.	PPT
TH-xxv	+++	+++	+++	− − −	− − −	St.	St.	St.
TH-xxvi	++	+++	++	− − −	− − −	St.	St.	St.
Th-xxvii	+++	+++	+++	+++	− − −	Unst.	Unst.	St.
TH-xxviii	+++	+++	+++	+++	− − −	St.	St.	St.
TH-xxix	+++	+++	+++	− − −	− − −	St.	St.	St.
TH-xxx	+++	+++	+++	+++	− − −	St.	St.	St.

Note:

+++ = Completely soluble
++ = Soluble with difficulty, not completely
+ = Partially soluble and partly forming susp.
− − − = Very little soluble.
St. = Stable
Unst. = Unstable
PPT = Decomposition of the compound (Precipitation of sulphur)
WPPT = Decomposition of the compound (White precipitate appeared)

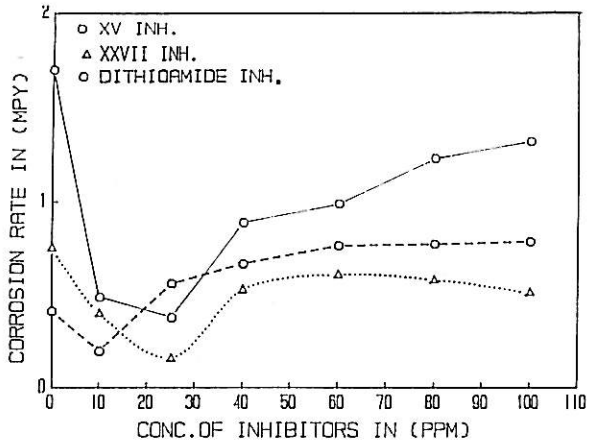


FIG. 2. Comparison of corrosion rate of different synthesized thioamides in brine water, at pH 4.5 to 4.8, in concentration ranges from 10 to 100 ppm, by using NACE standard wheel test method.

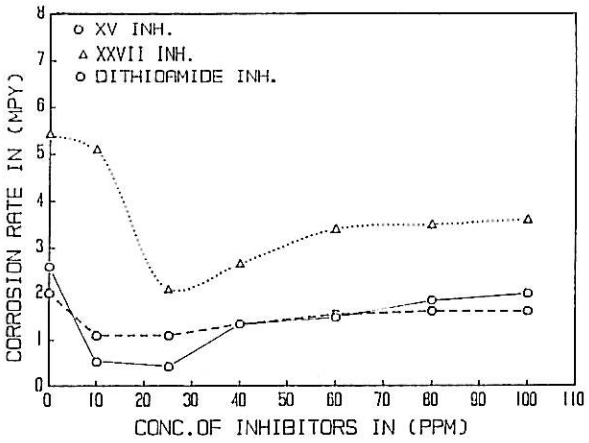


FIG. 3. Comparison of corrosion rate of different synthesized thioamides in sea water, at pH 4.5 to 4.8, in concentration ranges from 10 to 100 ppm, by using NACE standard wheel test method.

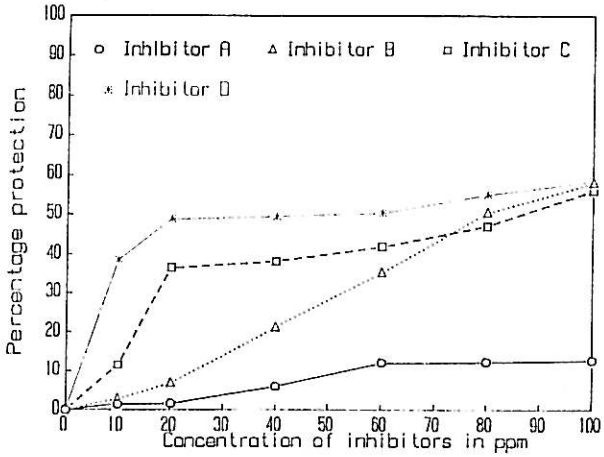


FIG. 4. Comparison of percentage protection of different commercially available amine base crude oil corrosion inhibitors, in brine water, at pH 4.5 to 4.8, in the concentration ranges from 10 to 100 ppm, by using NACE standard wheel test method.

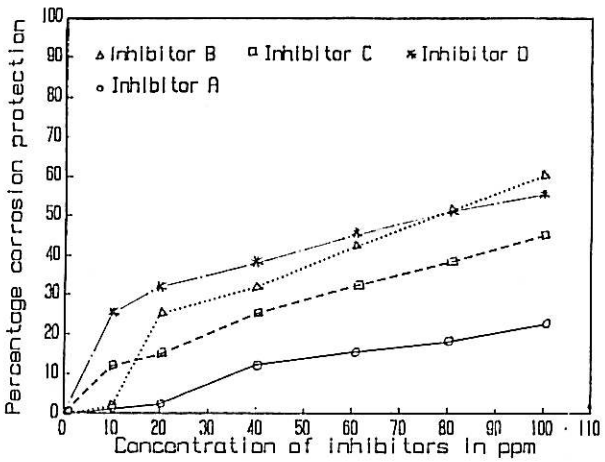


FIG. 5. Comparison of percentage protection of different commercially available amine base crude oil corrosion inhibitors, in sea water, at pH 4.5 to 4.8, in the concentration ranges from 10 to 100 ppm, by using NACE standard wheel test method.

between the corrosion rate and their concentration. Beside the above mentioned parameters it is also necessary to find out the emulsion tendencies and solubility percentage in the aqueous and oily medium in order to locate, in case of success, the suitable oil field application for the synthesised formulations.

CONCLUSION

In this work work series of thioamides different in molecular weight, molecular structure and molecular saturation, have been synthesised successfully. Their chemical characterisation and evaluation of anticorrosive properties, in crude form, are made in the artificial environment, similar to the formation water. Out of the synthesised compounds eighteen compounds were found to have percentage protection above fifty percent in the above specified environment. Comparative studies regarding the corrosion protection properties, of few of the synthesised and commercially available corrosion inhibitors show that the synthesised compounds are also good anticorrosives.

ACKNOWLEDGEMENT

The author would like to thank PRC Administration for providing facilities and necessary approval for executing this study and for their permission to publish the work. Thanks are also extended to the supervisor of the chemistry department for his assistance in providing the required chemical material and other necessities. The author is thankful to Mrs. Ebtisam Al-Tabany for her contribution in this work by reevaluating few of the mentioned compounds, as part of her B.Sc. Project.

REFERENCES

[1] L. Meites, Hand book of Analytical Chemistry. (Analysis of thioamides). Published by McGraw Hill, Inc. (1963): Page 12 to 168.

[2] L.L. Shreir, Corrosion Inhibition (Principles and Practice). Publ. Newnes Butterworth. Vol. 2, (1977): page 18:28 to 18:29.

[3] L.L. Shreir, Corrosion Inhibition (The Mechanism of Corrosion Prevention by Inhibitors). Publ. Newnes Butterworth. Vol. 2, (1977): page 18:34 to 18:35.

[4] J. Zabicky (Editor), The Chemistry of Functional Groups (The Willgerodt Reaction). Interscience Publ., New York, (1970): page 145–147.

[5] M.J. Janssen, Organo Sulphur Chemistry (The Willgerodt and Kindler Reaction). Interscience Publ., New York, (1967): page 229–232.

[6] M.W. Ranney, Corrosion Inhibitors (Manufacture and technology). Chemical Technology Review No. 60, (ndc), (1976): page 1.

[7] R.C. Denney, Named Organic Reactions. Publ. Butterworth, London, (1969): page 234–237.

[8] Marrison and Boyd, Organic Chemistry (Alkylation of Carbonyl Compounds via enamine). Publ. Allyn and Bacon, Inc., (1987): page 1071–1072.

[9] J. March. Advanced Organic Chemistry ("Reaction Mechanisms, and Structure" Willgerodt Reaction). Publ. McGraw-Hill Book Company, (1968): page 9:63 to 9:65.

[10] J. Zabicky (Editor), The chemistry of functional groups (The ultraviolet spectroscopic evidence of thioamides), (1970): page 400–406. Interscience publ., New York.

[11] Wheel Test Method used for Evaluation of Film Persistent Inhibition for Oil Field Applications, NACE Publication No. ID 182, (1982): page 45–47.

[12] Standard Practice for Preparing, Cleaning, and Evaluating Corrosion Test Specimens, Annual Book of ASTM Standards, vol. GO1.05, (1988): page 61–67.

[13] M.A. Sheriff, A. Hassan and A. Abusnena, Evaluation of Oil Field Corrosion Inhibitors by NACE Static Test Method and Wheel Test Method. Petroleum Reseach Journal, vol. 2, (1990): page 67–70.

PRJ, Vol. 5 (January 1993); P. 76–80, 3 FIGS, 2 TABLES.

Short Note

THE EFFECTS OF HYDROGEN ON THE FRACTURE TOUGHNESS OF STAINLESS STEEL

A.T. Hassan*

تأثيرات الهيدروجين على خشونة كسر الحديد غير القابل للتآكل

عبد الفتاح حسن

تمت في هذه الدراسة إجراء التجارب على نوعين من الحديد الغير قابل للتآكل (UB50, 410) باستعمال ثلاثة طرق مختلفة ، وذلك بتطبيق المواصفات الإنجليزية (5447) لقياس خشونة الكسر (K_{IC}). الطريقة الأولى شملت :

— الطريقة الكهروكيميائية للحصول على درجة عالية من التشبع بالهيدروجين.

— طريقة محلول جمعية التآكل الأمريكية من درجة الحرارة العادية.

— طريقة محلول جمعية التآكل الأمريكية من درجة 50 درجة مئوية.

ومن هذه الطرق الثلاثة تبين التالي :

— ارتفاع وانخفاض خشونة الكسر بالنسبة للحديد UB50, 410 على التوالي باستعمال الطريقة الأولى.

— إنخفاض خشونة الكسر لنوعين من الحديد باستعمال الطريقة الثانية.

— إرتفاع وانخفاض خشونة الكسر للحديد UB50, 410 على التوالي باستعمال الطريقة الثالثة.

INTRODUCTION

A duplex stainless steel UB50 and 410 martensitic stainless steel were exposed to hydrogen using three different methods. Cathodic charging with hydrogen in electrochemical cell, H_2S NACE solution which consisted of 5 weight percent (w%), NaCl, 0.5 w% acetic acid, and balance of deionized water at room temperature, and NACE solution at 50°C.

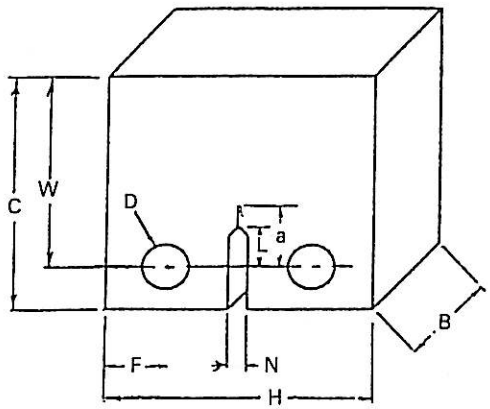
The effect of the methods on the fracture toughness showed that cathodic charging resulted in increasing and decreasing the fracture toughness of UB50 and 410; respectively. The H_2S NACE solution at room temperature resulted in decreasing the fracture toughness of both. Stainless steels and H_2S NACE solution at 50°C resulted in increasing and decreasing the fracture toughness of UB50 and 410; respectively.

EXPERIMENTAL PROCEDURE

Samples of two materials (UB50 and 410 stainless steel) were machined into crack growth specimen of dimensions shown in Fig. 1, [4]. The material chemical compositions of both alloys are given in Table 1. A fatigue precrack of length approximately $\frac{1}{2}$ w was placed in each sample prior to hydrogen cracking. The fatigue parameters used were 37–40 Hz, a maximum tensile load around 9 KN and a R-ratio of 0.1. The maximum load was chosen so that it would not exceed 70% of the expected value of K_{IC}.

The samples were cathodically charged with hydrogen in an electrochemical cell at constant current of 1.6 Amp. in 0.5 M H_2SO_4 with 1 g/l of thiourea added as a hydrogen recombination poison as shown in Fig. 2. Argon was bubbled through the solution both prior to and during the charging to remove any dissolved oxygen which might adversely affect the test. The precracked fracture toughness specimen was used as cathode and a platinum electrode was used as the anode. Direct current power source was connected to both electrodes to provide a constant current during charging operation. Another method of hydrogen charging was used which is exposing samples of both steels (UB50, 410) to a saturated H_2S NACE solution

*Petroleum Research Centre, P.O. Box 6431, Tripoli, G.S.P.L.A.J.



Dimension	Symbol	Measurement (mm)
Net width	W	25.40
Total width	C	31.75
Height	H	30.48
Hole diameter	D	6.35
Hole distance	F	5.08
Notch width	N	1.65
Effective notch length	*l*	6.75
Effective crack length	a	Measured after pre-crack

FIG. 1. Dimensions of test specimen (CTS).

was used as the cell and the charging time was thirty days. However, at the end of 30 days, the pH of the solution was nearly 0.30. This indicated high concentration of H^+ ions to generate H_2 gas throughout the entire test.

All samples were tested to determine the K_{IC} values within 15 minutes from the time they were removed from the electrochemical cell. A load vs strain curve was generated for all tests. The load was measured by the testing machine and the strain was measured from the clip gauge attached to the sample. The clip gauge allowed the actual strain of the sample to be measured instead of measuring the cross head position which would have included the strain of the test pins and attachments. The K_{IC} value was determined according to British standard 5447. A line was drawn through the origin of the load vs displacement plot with a slope 5% less than the slope of the elastic region. The load where this line intercepts the plot is called P_Q. K_Q is determined from P_Q and the geometry of the specimen. If the test data conform with all requirements outlined in the standard; the K_Q becomes the K_{IC} which is the fracture toughness. If the requirements are not met then only a K_Q value can be reported. All the results obtained in this study are K_Q values except one result, because in most instances, the value of P_{max}/P_Q was greater than 1.10 making the test invalid for K_{IC} determination.

Table 1. Compositions of Alloys

Elements	C	Si	Mn	S	P	Cr	Ni	Fe	Mo	Cu	Co
UB50	0.029	0.47	1.56	0.006	0.016	20.74	6.6	bal	2.4	1.4	—
AISI 410	0.13	0.33	0.4	0.006	0.002	13.2	0.38	bal	0.03	0.06	0.02

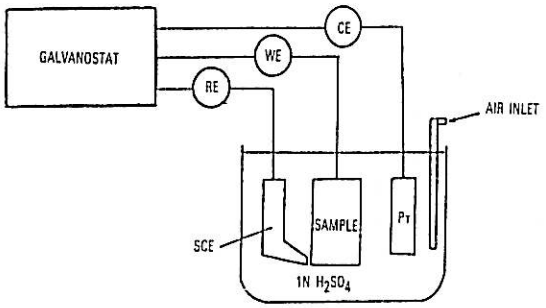


FIG. 2. Schematic diagram of hydrogen charging in electrochemical cell.

at 50°C and room temperature. For comparison the NACE solution was saturated by bubbling H_2S gas through the solution until the solubility limit has been reached.

Attempts were made to keep the pH of the solution low enough to maintain a high concentration of H^+ ions near the cathode producing a high partial pressure of H_2 gas near the sample. In the first test a four liter jug

RESULTS

The results obtained using L.E.F.M. method and the stated conditions as well as P_{max}/P_Q values, precracking length (a), specimen width (w) values, K_Q and K_{IC} values are listed in Table 2.

The values are plotted against curves generated from previous work done using H_2S environments (Fig. 3).

DISCUSSION

In order to reveal the embrittling effect of hydrogen uptake on the change of materials properties and the possible different response of the different stainless steels to hydrogen entry, the effects of precharging on the fracture toughness of both steels (UB50 and 410) was determined. All the specimens were machined with the notch and crack parallel to the longitudinal (rolling) direction.

Table 2. Fracture Toughness Results and Testing Conditions

Sample No.	Test Conditions	P_{max}/P_O	a/w	K_{IC} and K_O ($MPa/m^{1/2}$)
1B UB 50	4 litre cell cathodic charged for 11 days in H_2SO_4+1 gr l^{-1} thiourea solution	1.05	0.48	50
R UB 50	4 litre cell cathodic charged for 30 days in H_2SO_4+1 gr l^{-1} thiourea solution	1.06	0.49	55
3B UB 50	4 litre jar, specimen immersed in saturated H_2S NACE solution for 6 days at room temperature	1.2	0.57	46
3A UB 50	4 litre jar, specimen immersed in saturated H_2S NACE solution for 6 days at 50°C using water bath	1.16	0.50	51 (K_{IC})
1A UB 50	4 litre jar, specimen immersed in saturated H_2S NACE solution for 6 days at 50°C using water bath	1.16	0.50	54
410 (4)	4 litre cell cathodic charged for 6 days in H_2SO_4+1 gr l^{-1} thiourea solution	1.06	0.51	63
F 410 (2)	4 litre jar, specimen immersed in saturated N_2S NACE solution for 6 days at room temperture	1.02	0.51	60
410 (3)	4 litre jar, specimen immersed in saturated H_2S NACE solution for 6 days at 50°C using water bath	1.02	0.55	72
UB 50	4 litre cell cathodic charged for 13 days in H_2SO_4+1 gr/l thiourea solution	—	—	—

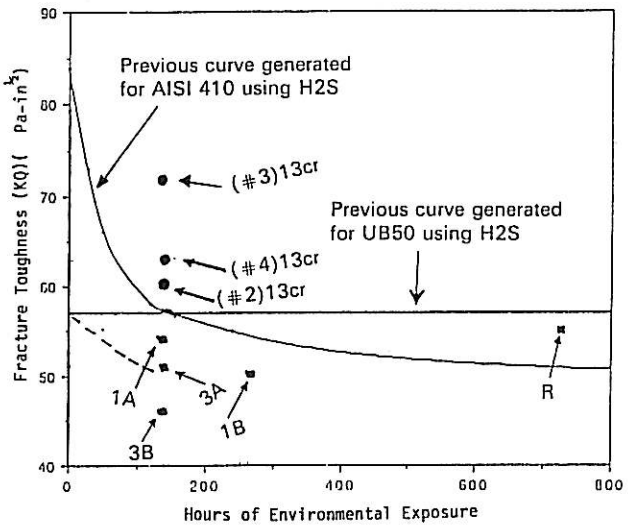


FIG. 3. Comparison of data from this study with results obtained. Descriptions of samples are given in Table 2.

Table 2 lists all values of K_Q of both stainless steel. These values are plotted against curves from previous study or work done using H_2S environment (Fig. 3).

The 410 martensitic stainless steel was actually very tough in air ($K_Q = 87$ Mpa/m$^{1/2}$), but its toughness dropped sharply in six days after immersion in H_2S NACE solution. Further pre-charging for up to 30 days results in entirely brittle fracture behaviour of the AISI 410 giving its K_{IC} of around 50 Mpa/m$^{1/2}$ [1]. All the results obtained concerning 410 are K_Q values because in most instances the requirements of BS 5447 are not satisfied making the test invalid for K_{IC} determination.

The results performed on 410 samples in two different conditions (H_2S NACE solution at room temperature and 50°C) using CT specimen correlate very well with the previous results conducted with H_2S environment Fig. 3.

Electrochemically charging with hydrogen (410 #4) has the same effect as using a reaction with H_2S at room temperature (410 #2) to embrittle the alloy. Increasing the temperature while using H_2S to charge the sample had a little effect on the fracture toughness: on the sample (410 #3) exposed to H_2S NACE solution at 50°C for six days the fracture toughness value (72 Mpa/m$^{1/2}$) is below the line constructed from that taken using an H_2S environment at room temperature, Fig. 3.

The method of hydrogen charging has relatively little effect on the fracture toughness of 410 while the bulk precharging of H_2S had a significant precharging effect on the 410. The temperature also has an effect on the fracture toughness of 410 in a H_2S environment.

The electrochemical charging of specimens (IB UB50 and R UB50) shows a small decrease and no change in the fracture toughness respectively. The base-line fracture toughness value of UB50 before any environment exposure was close to the 52 Mpa/m$^{1/2}$ obtained in the previous study [1] Fig. 3. This gives good indication that the electrochemical hydrogen charging has a little if any effect on the fracture toughness of UB50 (specimens R UB50, IB UB50). The fracture toughnes however, is reduced after charging with H_2S NACE solution at room temperature (46 Mpa/m$^{1/2}$).

The H_2S content of a saturated H_2S NACE solution at 20°C is approximately 2700 ppm and at 50°C this value dropped to 1300 ppm.

The decrease in H_2S content of the solution at higher temperature as mentioned above causes the samples exposed to H_2S NACE solution at 50°C to have a higher fracture toughness for UB50 as shown in Table 2.

Another explanation for this phenomenon is that increased diffusion at higher temperature [2, 3] had a greater effect than the lower H_2S concentration.

In case of AISI 410 stainless steel, Table 2, the same effect of temperature was observed as for UB50, i.e. when the temperature increased the fracture toughness increased.

CONCLUSION

Due to time constraints only a limited number of the tests were performed during this study.

1. Electrochemical hydrogen charging lowers the fracture toughness of both 410 and UB50 stainless steels. The effect of the electrochemical on AISI 410 was slightly lower than the effect observed in a previous study, but higher for UB50 than observed in a previous study.
2. The effect of the electrochemical hydrogen charging appears to be slightly higher than the effect of the H_2S NACE solution, for both steels (UB50 and 410).
3. The drop in fracture toughness of UB50 was relatively small compared to the decrease observed with the AISI 410 stainless steel.
4. The effect of H_2S NACE solution at 50°C has a significant effect on the fracture toughness of both stainless steel (410 and UB50). Increasing the temperature, from room temperature to 50°C, increased the fracture toughness of both steels.

ACKNOWLEDGEMENT

I wish to thank the management of the Petroleum Research Centre for giving me the opportunity to carrying out this type of work.

Also the assistance and guidance of Dr. R. Brook and Prof. J. Yu from the University of Sheffield are greatly appreciated.

REFERENCES

[1] S. Yu and R. Brook, "Sulphide Stress Corrosion Cracking of Stainless Steels", Special Report University of Sheffield 1992.
[2] J.C. Scully, Corrosion Science 15, 1975, 205.
[3] J.C. Scully Ibid, TMS, AIME, New York, 1976, 129.
[4] "Plain Strain Fracture toughness (K_{IC} of metallic materials" British Standard 5447, 1977.